

TRANSFER

Výzkum a vývoj pro letecký průmysl

č 16 / 2011



AIIV
CZECH REPUBLIC

SPACE'2011 International Seminar
"ADVANCED DEVICES, MATERIALS AND RESEARCH METHODS FOR SPACE APPLICATION"
5-6 October 2011 Prague, Czech Republic

CZECH TECHNOLOGICAL PLATFORM FOR THE AVIATION AND SPACE

OPERAČNÍ PROGRAM PODNIKÁNÍ A INOVACE

EUROPEAN UNION EUROPEAN REGIONAL DEVELOPMENT FUND INVESTMENT IN YOUR FUTURE

Logos included in the grid: AeroSpace, Aeromedie, AET, ATG, as, AZ, AeroSpace, Evertor, Evertor, Honeywell, i, Jihlava, Jihlava, COMPOSITE, MESIT, Mikrotechnika, LOM PRAGUE, Prague Cast, MESIT, Mikrotechnika, RayService, SAAB, Schenck-Hirth, SKYLEADER, SPEEL PRAHA, SVOM, TCZ, UNIS.

Toto číslo elektronického sborníku obsahuje příspěvky přednesené na mezinárodním semináři - Pokročilé technologie, materiály a zařízení pro kosmické aplikace.

"Advanced technologies, materials and devices for space application"

ISSN 1801 - 9315

Výzkumný a zkušební letecký ústav, a. s.
ZA PODPORY ASOCIACE LETECKÝCH VÝROBCŮ ČR A ČESKÉ TECHNOLOGICKÉ
PLATFORMY PRO LETECTVÍ A KOSMONAUTIKU
spolufinancované fondem EU



EUROPEAN UNION
EUROPEAN REGIONAL DEVELOPMENT FUND
INVESTMENT IN YOUR FUTURE



SPACE'2011
International Seminar
“ADVANCED DEVICES, MATERIALS AND RESEARCH METHODS
FOR SPACE APPLICATION”
5-6 October 2011
Prague, Czech Republic

TRANSFER

Výzkum a vývoj pro letecký průmysl
Elektronický sborník VZLÚ, a.s.
číslo 16, říjen 2011, 6. ročník

Adresa redakce:

Výzkumný a zkušební letecký ústav, a.s.
Beranových 130, 199 05 Praha 9, Letňany
Tel.: 225 115 223, fax: 286 920 518

Šéfredaktor:

Martina Monteforte Hrabětová (e-mail: monteforte@vzlu.cz)

Vydavatel:

Výzkumný a zkušební letecký ústav, a.s.
© 2010 VZLÚ, a.s.

Space'2011 international seminar “Advanced devices, materials and research methods For space application”

Organized by

Aeronautical Research and Test Institute (VZLU), Prague, Czech Republic
and
Semenov Institute of Chemical Physics Russian Academy of Sciences (ICP RAS), Moscow,
Russian Federation
and
Saint-Petersburg State University of Aerospace Instrumentation (SUAI), Saint – Petersburg,
Russian Federation

The book consists of the abstracts of oral contributions to the Czech-Russian Workshop on **ADVANCED DEVICES, MATERIALS AND RESEARCH METHODS FOR SPACE APPLICATION “SPACE 2011”** (October 5 - 6, 2011, Prague, Czech Republic).

The following questions are covered:

Sensors and instruments for space applications

- Development of sensors and instruments for space applications
- Advanced detecting and measurement systems in optics, electronics, magnetism and astrophysics
- Laser technologies and optical data transmission systems
- Measurement of residual microaccelerations on board of a spacecraft
- Ground testing of space sensors
- Innovative technology for detection and measurement of the third millennium
- International co-operation and prospective projects

Advanced materials for space applications

- Typical composite material applications in space platforms and vehicles
- New types of stiff high-temperature resistant ceramic materials
- Amorphous metal, metal foams and their application in space
- New types of adhesives or matrices filled by nanoparticles
- New types of light metal alloys for space application
- Friction welding technology for aerospace production
- Thermoplastic composites and their application in space
- Materials for thermal and shock protection
- Ground testing of materials
- Out of autoclave composite processing technologies (RTM, Vacuum Bagging) - new design

Original author's style including interpretation, formulas and names of chemical/physical processes, schemes, pictures and explanations, is preserved in the abstracts published in this book.

**THE CONFERENCE WAS HELD UNDER FINANCIAL SUPPORT OF THE EUROPEAN
REGIONAL DEVELOPMENT FUND INVESTMENT IN YOUR FUTURE (EUROPEAN UNION)**

Table of contents

- 6 GNSS observations and products for precise Earth monitoring**
Ing. Jan Douša, Ph.D. (jan.dousa@pecny.cz), Geodetic Observatory Pecný, Research Institute of Geodesy, Topography and Cartography
- 10 Software Package for Simulation and Design of Complex Flexible Space Vehicles**
Alexander V. Nebylov, professor, Director of International Institute for Advanced Aerospace Technologies of Saint Petersburg State University of Aerospace Instrumentation
Alexander I. Panferov, docent of Saint Petersburg State University of Aerospace Instrumentation, Faculty of aerospace instruments and systems
Sergey A. Brodsky, senior staff scientist, International Institute for Advanced Aerospace Technologies of Saint Petersburg State University of Aerospace Instrumentation
- 14 Loop Heat Pipes – High-Efficient Heat-Transfer Devices for Spacecrafts Thermal Control Systems**
Dr. Yury F. Maydanik, Institute of Thermal Physics, Ural Branch of the Russian Academy of Sciences
- 18 Single photon laser altimeter and lidar in space missions**
Ivan Procházka¹, Josef Blažej¹, Vojtěch Michálek^{1,2}, Michael Vacek^{1,2}, Marek Peca²
¹Czech Technical University in Prague, Břehová 7, 115 19 Praha 1, Czech Republic
²Aeronautical Research and Test Institute, Beranových 130, 199 05 Prague, Czech Republic
- 21 Time-to-Digit Converter Based on Radiation-Tolerant FPGA**
Marek Peca^{1,2}, Michael Vacek^{1,2}, Vojtech Michalek^{1,2}
¹ Vyzkumny a zkusebni letecky ustav, a. s.
² Ceske vysoke uceni technicke v Praze, Fakulta jaderna a fyzikalne inzenyrska, Katedra fyzikalni elektroniky
- 26 The time-optimal control of a motion for a spacecraft with inertial executive devices**
Mikhail Levskii, Research Institute of Space systems
- 29 Worst Case Analysis of an Accelerometer Measuring Loop**
Jozef Zakucia
- 32 Space Solar Patrol data and the global changes**
*S.V. Avakyan¹, L.A. Baranova², E.V. Kuvaldin¹, N.B. Leonov¹,
A.V. Savuyshkin¹, N.A. Voronin¹, V.V. Kovalenok³, V.P. Savinykh⁴,*
¹All-Russian Science Center "S.I. Vavilov State Optical Institute", Birgeyaya linia, 12, Saint-Petersburg,
²A.F.Ioffe Physico-Technical Institute of RAS, Saint-Petersburg, Russian Federation
³Federation of Cosmonautics of Russia
⁴Moscow State University of Geodesy and Cartography
- 35 Solution of the problem of recognition celestial sky in astronavigation.**
A. P. Grigoryev , V. Y. Mamaev State University of Aerospace Instrumentation, Saint-Petersburg, Russia

- 38 Intelligent training system for advanced spacecraft pilot**
A. P. Lastochkin, V. Y. Mamaev State University of Aerospace Instrumentation, Saint-Petersburg, Russia
- 40 Analysis of the Concept and Prospects for Developing a Network of Micro- and Nano-Satellites for Research and Commercial Applications**
Alexander V. Nebylov, Professor, Director of International Institute for Advanced Aerospace Technologies of Saint Petersburg State University of Aerospace Instrumentation
- 44 Calculation of Temperature Fields of Vibrating Composite Part**
Ing. Vilém Pompe, Ph.D
- 47 Properties of ejecta generated at high-velocity perforation of thin bumpers made from different constructional materials**
*N.N. Myagkov^{a)}, T.A. Shumikhin^{a)}, L.N. Bezrukov^{b)},
^{a)} Institute of Applied Mechanics of RAS, Leninsky prospect 32A, Moscow 119991, Russia
^{b)} State Research Institute of Aviation Systems (GosNIIAS), Victorenko street 7, Moscow 125319, Russia*
- 50 Combustion Characteristics of Droplets of Paraffin Propellants**
*S.G. Orlovskaya¹, V.V. Kalinchak¹, V.Ya.Chernyak², F.F. Karimova¹, M.S. Shkoropado¹, E. Yu. Aktan²
¹ Odessa National I.I. Mechnikov's University, Dvoryanskaya str.2, Odessa, 65082, Ukraine
² Kiev National T.G. Shevchenko University, Acad. Glushko 2/5, Kiev, 03022, Ukraine*
- 52 The fatigue test effectiveness improvement using NDT methods combination**
Ing. V. Makarov, Ing. V. Horak, VZLÚ a.s., Prague, Czech Republic
- 55 LF Technology – Smart method for composite parts production**
Mgr. Eva Straňáková, Ing. Richard Pavlica, Ph.D.
- 59 Friction Stir Welding of Aerospace Structures**
Ing. Petr Bělský / VZLÚ, a.s., Prague

GNSS observations and products for precise Earth monitoring

Ing. Jan Douša, Ph.D. (jan.dousa@pecny.cz), Geodetic Observatory Pecný, Research Institute of Geodesy, Topography and Cartography, Ústecká 98, Zdíby, 250 66, Czech Republic

Global Navigation Satellite Systems (GNSS) were primarily designed for the navigation, but today the GNSS observations provide possibility to monitor the changing Earth precisely. We present examples based on the GNSS data analyses provided by the Geodetic Observatory Pecný, RIGTC, namely for precise monitoring of the Earth's rotation, lithosphere and atmosphere. Additionally, we discuss the estimation of precise orbits as a prerequisite in such type of applications, in particular for (near) real-time applications.

INTRODUCTION

In this paper we describe the example exploitations of the Global Navigation Satellite System observations (GNSS, currently represented by American GPS NAVSTAR and Russian GLONASS) in highly accurate applications like the scientific monitoring of the changes in the Earth's rotation, lithosphere and atmosphere.

Any effort starts with the data collection - the GNSS observations are typically collected using various observation scenarios – real-time streams, hourly and daily files, high-rate data, extra signals and systems, etc). However, additional precise products and models are required in order to estimate the principle parameters of the standard GNSS observation model – the receiver position and troposphere path delays – with the highest achievable accuracy. The precise products and models are available (usually free of charge) thanks to a close cooperation within the geodetic scientific community.

The most important products are precise satellite orbits and clocks, available for both post-processing and (near) real-time applications such as the estimation of receiver positions (e.g. in support of geodynamics studies, a natural hazard monitoring, early warning systems), precise estimates of atmospheric parameters (e.g. in support of numerical weather prediction, climate study) etc. The precise orbit and clock products are provided independently by several analytical centres worldwide, but these individual contributions are finally combined into a robust solution at the International GNSS Service (IGS, www.igs.org). The examples of data GNSS analyses for the monitoring of changing Earth are based on results provided by the Geodetic Observatory Pecný (GOP, www.pecny.cz) of the Research Institute of Geodesy, Topography and Cartography (RIGTC, www.vugtk.cz).

GNSS OBSERVATIONS AND THEIR DISSEMINATION

Linear model of the GNSS code P_{Af}^i and phase L_{Af}^i observations for the receiver A , satellite i and frequency f is written as follows:

$$P_{Af}^i = \rho_A^i + c \cdot \delta_A - c \cdot \delta^i + I_{Af}^i + T_A^i + c \cdot B_{Af} - c \cdot B_f^i$$

$$L_{Af}^i = \rho_A^i + c \cdot \delta_A - c \cdot \delta^i - I_A^i + T_A^i + c \cdot b_{Af} - c \cdot b_f^i + \lambda_f \cdot N_{Af}^i$$

where ρ_A^i is a geometrical distance between receiver and satellite, δ^i , δ_A are satellite and receiver clock corrections, I_A^i is the effect of the ionosphere, T_A^i is the effect of the troposphere, B_f^i , B_{Af} are code hardware biases, b_f^i , b_{Af} are phase hardware biases and λ_f is wavelength of the frequency f , N_{Af}^i is initial ambiguity (unknown number of full wavelengths between transmitting from a satellite and receiving at a receiver).

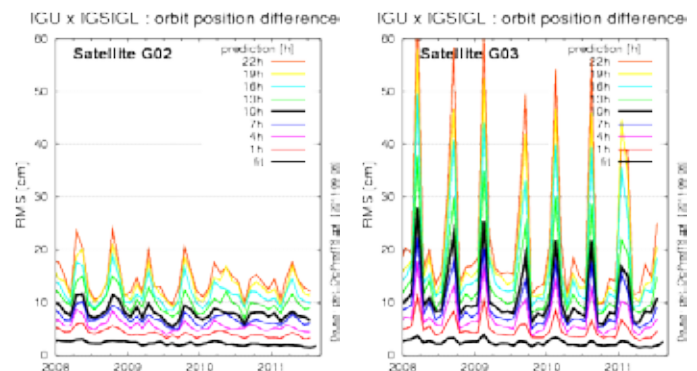


Fig. 1: Accuracy of the fitted (0h) and predicted (1h,4h,7h,10h,13h,16h,19h,22h) orbits of GPS Block IIR (left) and GPS Block IA (right). The fluctuation is caused by regular eclipsing periods (by Earth).

The Geodetic Observatory Pecný initiated the observing of GPS NAVSTAR in 1992. The operational data collecting started in 1995, the GLONASS capability was added in 2000 and the tracking Galileo signals will start with the upcoming In Orbit Validation Galileo (IOV) phase in 2011. Additionally, GOP supports the operation of other 8 stations constituting altogether the Scientific Experimental Network for GNSS Observations (VESOG, oko.asu.cas.cz/VESOG). One station is part of the IGS network, 6 stations of the EUREF Permanent Network (EPN) and, finally, 4 stations are part of the Czech Positioning System

(CZEPOS, czezos.cuzk.cz). GOP supports also the GNSS data and products exchange by the operating the GNSS data centre (ftp://ftp.pecny.cz/LDC) and by the disseminating the real-time data and streams via NTRIP caster (http://ntrip.pecny.cz:2101).

PRECISE SATELLITE ORBITS AND EARTH ROTATION

Although the GNSS navigation message contains necessary information about the satellite positions, most of the scientific GNSS applications require more precise products for example such provided by IGS. For near real-time applications (see troposphere estimation). GOP developed a highly efficient ultra-rapid solution for the precise GPS orbit determination already in 2000. Since 2004 it has contributed to the IGS ultra-rapid orbit solution, which is combined from up to 7 individual products and which is widely used in both scientific and commercial applications.

The 24 hour fitted and 24 predicted orbits are routinely updated every 6 hours in order to support both near real-time and real-time applications. The GOP orbit accuracy (expressed with position 1D RMS) is about 5cm and 12cm in 24-hour fitted and 12-hour predicted satellite position, respectively. The accuracy of the IGS ultra-rapid orbits is slightly better, but the main benefit of the combined product remains in its high robustness, stability and completeness. Additionally, the combination process provides a highly relevant orbit accuracy assessment, which is useful for a proper weighting of satellite observations in end-user applications.

However, the events exist such as the satellite eclipse and manoeuvres, which significantly affects the quality of orbits. The plots in Figure 1 show examples of the fluctuation of the orbit accuracy due to the regular eclipsing periods affecting satellites in a different ways (left figure shows the newer GPS Block IIR satellite, right figure shows the older GPS Block IIA satellite). The effect needs to be considered at a user side for handling such satellites in real-time applications, since the predictions degrade much faster for the old-fashioned satellites.

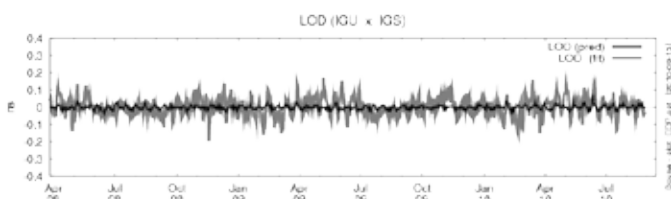


Fig. 2 Time-series of estimated and predicted LOD parameters

Finally, in order to link the inertial system used for the orbit determination and the terrestrial system used for the receiver position on the ground, the Earth's rotation parameters need to be estimated and provided together with the orbits. However, from the GNSS observations, we can estimate only X, Y pole coordinates with their changes in time and the length of a day (LOD). The pole coordinates represent the position of the rotation axis with respect to the Earth crust and the LOD represents the excess of the astronomically measured day duration from expected 86400 SI seconds. Other Earth's orientation parameters cannot be estimated using GNSS. Figure 2 shows the example of fitted and predicted LODs time-series based on GNSS. The overall accuracy of all estimated parameters is summarized in Table 1.

fitted / predicted	orbits [cm]	X, Y pole coord. [mas]	X, Y pole rates [mas/day]	length of a day [ns]
GOU	6 / 12	0.1 / 0.3	0.2 / 0.4	0.03 / 0.07
IGU	<5 / 10	0.1 / 0.3	0.3 / 0.5	0.03 / 0.06

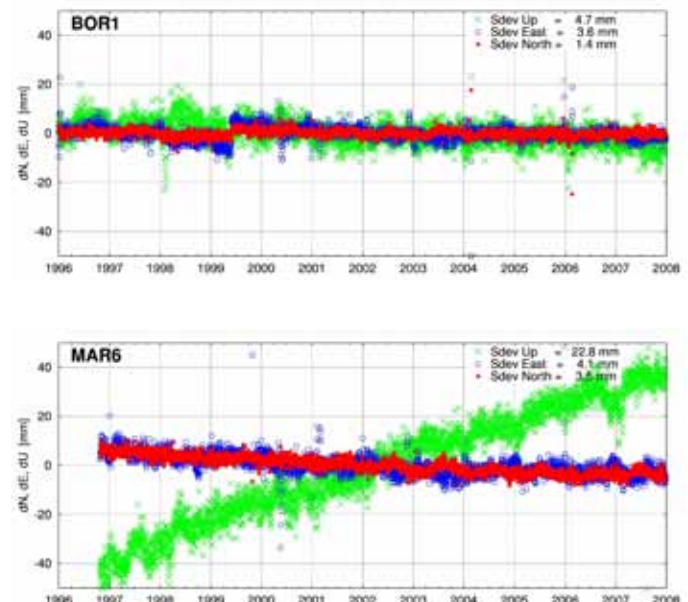
Tab. 1 RMSs of fitted and predicted orbit and earth rotation parameters from GOP (GOU) and IGS (IGU)

RECIEVER COORDINATES AND VELOCITIES

Although there are various applications based on the precise receiver positioning, we focus only on those related to the phenomena due to geodynamic processes. The first is related to the defining, realizing and maintaining terrestrial reference systems required by most of the applications. Today, the global, regional and national reference systems are realized using arrays of permanent GNSS stations. For example, the European permanent network (epncb.oma.be) consisting of about 250 GNSS stations today is organized by the International Association of Geodesy's sub-commission for the European Reference Frames (EUR-REF) as a co-operated effort of a data collection, dissemination and processing.

The GOP analysis centre has contributed via analysing a specific EUR-REF sub-network since 1997 and, recently, via a re-processing effort in order to achieve a complete and homogeneous solution based on up-to-date products and models. The primary goal is to estimate precise coordinates and derive residuals time-series (North, East, Up), the example is given in Figure 3. Since the processing aims for the highest accuracy, daily batches are analysed using the final IGS products and most-accurate models.

The raw time-series generated from such independent daily or weekly solutions include many different effects such as the instrumentation changes (BOR1), post-glacial uplift (MAR6), post-seismic movements (TUBI), seasonal effects due to snow and ice covering antenna (HFLK) and also changes in processing models, strategies and reference frame. However, the last ones are not relevant for the plots of figure since these are based on a homogeneous re-processing solution.



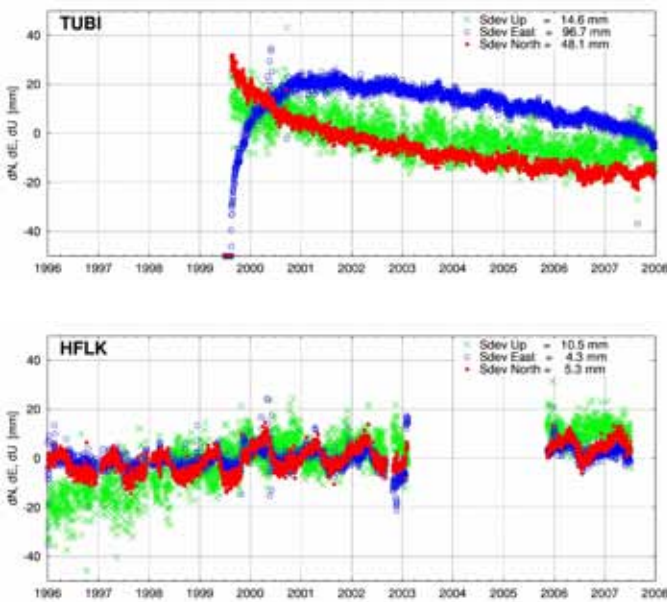


Fig. 3 North, East, Up coordinate residuals time-series - examples for 4 European stations showing different effects. Plots are based on homogeneous re-processing solutions during 1996-2008

To estimate a precise set of the coordinates for individual stations we apply the stacking of daily/weekly normal equations to provide a unique combined solution. However, to eliminate the effects visible in Figure 3 we have to setup a simple velocity model (with some exceptions, e.g. TUBI, the linear approximation is sufficient for Europe). Additionally, we identify epochs of discontinuities in time-series to setup a new set of coordinates if necessary (e.g. because of the antenna change). In such solution we get a simple coordinate and velocity model for realizing a long-term reference frame. Figure 4 shows the N, E, U coordinate repeatability for all stations based on the raw (left) and combined (right) coordinate residuals. The repeatability from the combined solution has been significantly reduced - 2mm and 6mm in horizontal and vertical component, respectively - due to the applying discontinuity and velocity models in combination. The velocity models and coordinate residuals (because of insufficiency of the velocity model) based on the combined solution are important input for studying crust movements, crust elastic responses for various loading effects, co-seismic and post-seismic movements, land-slides, and many other phenomena.

The GOP analysis centre also provides a system of routine performance and stability monitoring of all stations of the Czech Positioning System (CZEPOS, czepos.cuzk.cz) and some other private networks. Through the estimation of the latest coordinates (usually with a delay of one day) we monitor the official coordinates providing an access to the official reference frame and, additionally, we estimate seasonal or other effects on the station coordinates in a long-term.

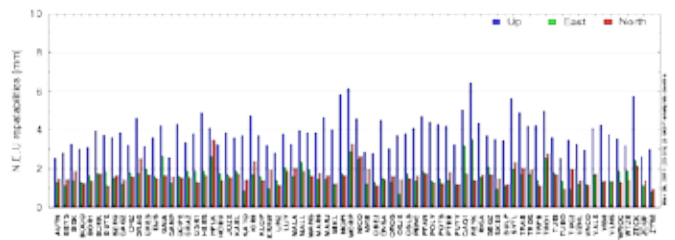
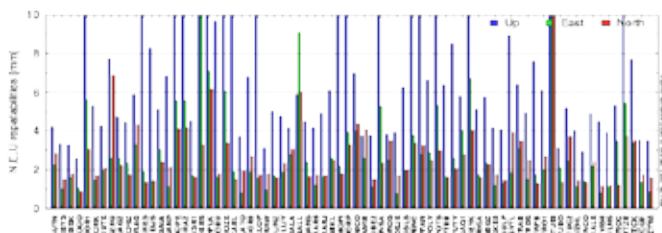


Fig. 4 Coordinates repeatability from the raw (left) and combined (right) solutions from GOP re-processing

ATMOSPHERE MONITORING

The GNSS signal paths are delayed due to the ionosphere and the troposphere. While the first can be eliminated using dual-frequency measurements, the latter is usually not a priori known with a sufficient accuracy. That's why the troposphere path delays are regularly estimated along the receiver coordinates. On other hand, ionosphere is eliminated using ionosphere-free linear (L_3) combination from L_1 and L_2 phase observations on f_1 and f_2 frequencies

$$L_3 = \frac{1}{f_1^2 - f_2^2} (f_1^2 L_1 - f_2^2 L_2)$$

The troposphere path delay can be split into two components – a hydrostatic delay and a wet delay. While the first one can be precisely modelled based on atmospheric pressure at the receiver location, the latter cannot be modelled due to a highly temporal and spatial variability of the water vapour causing this effect. To estimate troposphere path delays in a GNSS analysis, we setup a simplified model mapping the direct path delay T (for a satellite and receiver pair) to the zenith total delay (ZTD) using the zenith distance (z) dependent mapping function $m_f(z)$. The different mapping functions are defined for the zenith hydrostatic delay (ZHD) and the zenith wet delay (ZWD) while ZHD is used as a priori value and ZWD is estimated from the data. To account for the azimuth (A) asymmetry of the mapping function, two horizontal tropospheric gradients can be estimated (in direction to North and East) by a simple tilting of the mapping function. The complete model can be thus written as follows

$$T = m_{fH}(z) \cdot ZHD + m_{fW}(z) \cdot ZWD + GRD_N \frac{\partial m_f}{\partial z} \cos A + GRD_E \frac{\partial m_f}{\partial z} \sin A$$

Typically, the ZTD (ZHD + ZWD) is estimated for a receiver applying a piece-wise constant or linear model (e.g. for 1h) or, alternatively, as a stochastic white-noise process. Since ZWD contains information about the integrated water vapour (IWV) in the atmosphere it is highly usable in meteorological applications.

For climate research, the ZWD need to be estimated as much as precisely and using a homogeneous analysis because long-term trends in ZWDs are of main interest. The post-processing strategy and the final IGS products are required as well as the re-processing activity whenever applied models have been updated. GOP contributes to the EUREF re-processing project and provided 15-year ZTD time-series for 80 stations in Europe. The trends, however, are not yet estimated with a sufficient accuracy and it is not expected earlier than at the end of a decade.

When the GNSS troposphere solution is upgraded in near real-time mode (usually every hour), estimated ZTD (or ZWD) are of a high interest for the assimilation into numerical weather models (NWM) for im-

proving the weather forecasting. Rapid developments in now-casting systems for very short-term predictions on one side and the current capability of GNSS observations disseminated and analysed in real-time on the other side, a high potential is foreseen for improving the monitoring and warnings during situations with strong rainfalls, thunderstorms or floods.

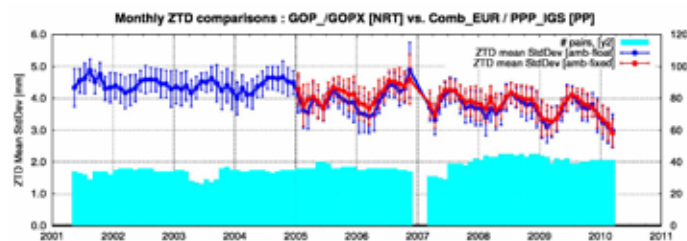


Fig. 5 Mean bias and standard deviation of ZTD from all stations estimated in near real-time in GOP

The GOP has been one of the first analysis centres processing data from national and European GNSS permanent stations in support of a numerical weather forecasting. During 10 years, GOP collaborated with the meteorology community in different EU projects (COST-716, TOUGH FP5 EU, E-GVAP). Within these, so called GPS-meteorology has evolved from near real-time ZTD estimation system developments, which has extended to 11 analysis centres contributing with ZTDs from about 1600 unique stations, and turning up to the operational service during the EUMETNET GNSS Water Vapour Programme II. Figure 5 displays the time-series of a mean ZTD bias and standard deviation over all processed stations estimated routinely every hour at GOP. ZTDs are compared to the final EUREF troposphere product. Today, standard deviation and bias of ZTD achieves 3–4mm and 1mm, respectively, and the products are delivered to the UK Met Office database within 1h 45min. Currently, GOP is fully supporting a multi-GNSS ZTD solution after the successful evaluation of stand-alone GPS and GLONASS ZTD solutions (Figure 6).



Fig. 6 ZTD time-series based on multi-GNSS and stand-alone GPS and GLONASS solutions by GOP

CONCLUSION

By regularly processed GNSS data from the national, regional and global permanent stations, GOP analysis centre estimates various parameters of interest – receiver and satellite positions, troposphere and ionosphere path delays, earth rotation parameters and some others. While some of them are estimated in order to provide the most accurate products for geodetic or non-geodetic applications, the others are able to serve for a high accurate monitoring of the Earth changes – the water vapour content in the lower atmosphere, the total electron content in the upper atmosphere, crustal motion, rotation and orientation of the Earth axis and others. Via providing many of them GOP contributes to various international services and projects. Future perspectives are foreseen in mainly in the field of real-time analyses and the exploitation of all available GNSS observations (global GPS, GLONASS, Galileo and COMPASS and other geostationary systems).

Software Package for Simulation and Design of Complex Flexible Space Vehicles

Alexander V. Nebylov, professor, Director of International Institute for Advanced Aerospace Technologies of Saint Petersburg State University of Aerospace Instrumentation

Alexander I. Panferov, docent of Saint Petersburg State University of Aerospace Instrumentation, Faculty of aerospace instruments and systems

Sergey A. Brodsky, senior staff scientist, International Institute for Advanced Aerospace Technologies of Saint Petersburg State University of Aerospace Instrumentation

Keywords: *mathematical model, flexible vehicle, simulation, sloshing, local angle of attack, oscillations damping*

New results in the field of automaton of aerospace flight control system design are presented in the paper. The concept of a universal program for research of dynamic properties, calculation of comprehensive mathematical models, simulation of the flight motion and synthesis of smart control laws for different types of the flexible aerospace constructions (mainly launchers and missiles) is considered. The special attention to creation of mathematical models of different physical phenomenon of aerospace vehicles is given. The basis of the program is the structure, which allows carrying out of the analysis of dynamic characteristics, simulation, and visual information representation. The software package is supplied with the library of program modules. These modules are designed on the base of mathematical models of separate vehicle elements and different physical effects, such as flexibility, sloshing, sluggishness of engines, local angle of attack values, etc. Selection of different sets of the mathematical models and program modules allows investigating different constructions for known and prospective vehicles. The interface of the program enables changing parameters of the vehicle in a wide range, to simulate flight at any trajectory and to output results of the analysis in a digital or graphical form. For synthesis of control laws, provides the usage of the smart control approach.

1. INTRODUCTION

The mass and aerodynamic characteristics of flying vehicles can be considerably varied during their motion. From the point of view of control theory the aerospace craft represents a typical non-linear and non-steady controlled plant. Designers of vehicles aim to create maximum light designs. This process results in deformation of vehicle during the flight and development of the vehicles' elastic properties. Elastic longitudinal and lateral oscillations of the composite shape arise. Frequencies of these oscillations are variable during the flight. Elastic vibrations are usually described by partial derivative equations or ordinary differential equations of high order. Deformations of a body result in development of local attack and slide angles. The aroused local forces and moments of forces are synchronized with variations of local an-

gles. These mechanisms cause the additional oscillations of a body or damping of elastic vibrations. Oscillations of fuel and oxidizing agent in tanks cause the development of forces and moments concerning all three axes of a vehicle [1]. Sophisticated construction of modern vehicles results in necessity to separate the process of vehicles design into several stages.

The program allows inputting constructive parameters of the vehicle, including the linear dimensions of a body, parameters of the engine, the sizes and arrangement of tanks with fuel and oxidant, aerodynamic coefficients, distribution functions of pressure and mass along the vehicle centerline. On the initial stage of vehicle motion analysis the simplest models are used and the vehicle is supposed as an absolutely rigid body. Since most vehicles are unstable, direct modeling does not

allow obtaining full data about dynamical properties of vehicles. For this reason the suggested software provides the possibility to calculate the indirect characteristics of controllability and stability at each instant of flight. The program enables calculation of transfer functions for each instant of flight. It is possible to lower the order of transfer functions by excluding such factors as sloshing, flexibility and other submodels. The program is able to evaluate the roots of characteristic equations, and to plot the responses in time and frequency domains.

A discrete model of flexible vehicle, represented as a beam with linearly varying cross sectional properties, is used. The mass, stiffness and damping matrices calculated by a discretization technique correspond to the hypothetical vehicle with given distribution of linear parameters. It is possible to justify the choice of sampling interval. Local load is evaluated with the account of distributed aerodynamics forces, which depend on a local angle of attack, local airspeed and linear aerodynamics coefficients. Stochastic wind distortions are taken into account. Mathematical model for sloshing of a free surface of liquids in tanks is presented.

The program allows estimating the flexible motion for all points along the vehicle for each flight instant. This flexible motion is determined by three functions of time t and coordinate x along the vehicle: displacement of the elastic line from the longitudinal neutral axis, and the first and second order x -derivatives of this displacement. Outcomes of modeling are presented as three-dimensional animations of vehicle motion and charts of functions of t and x .

At the first design stage the vehicle is investigated as a variable mass solid body [2]. The problem of rational aerodynamic vehicle mounting and needed efficiency of control system actuators is solved at the first stage. It is treated a problem of motion stabilization of vehicle as a rigid body. Methods of aerodynamics, flight dynamics, automatic control, and also specialized and universal programs, such as MATLAB are usually used.

Elasticity of a vehicle and oscillation of liquid in tanks are taken into account at a following design stage. Local forces and the moments of forces such as functions of time and coordinates along a centerline of a vehicle are calculated. Analytical and semi-graphical methods of calculation at this stage give only approximated outcomes [4]. Special programs, for example, ANSYS, NASTRAN, Coventor, Structural Dynamics Toolbox for use with MATLAB, etc are designed to research the elastic systems. However, these programs do not address many issues that appear in flight vehicle design. The purpose of this paper is to present the specialized software package for designing different types of vehicles.

2. DESCRIPTION OF THE PROGRAM

The block diagram of control system of a flexible vehicle is shown in Fig. 1. Initial window is shown in Fig.2. The program is a universal tool for simulation of flight for wide class of vehicles. Vehicle can have arbitrary configuration, mass, length and other parameters. Speed, height, attitude, angle of attack, angle of slide may vary within a wide range.

All these parameters are input into the program in numerical or graphical form. „Simple“ nonlinear model of rigid vehicle is calculated at the first design stage. Usually vehicles are unstable. For this reason it is ne-

cessary to design simple control system without filters for suppression of aeroelastic oscillations. Simple model of vehicle and simple control system is used only for primary simulation. Prescribed program trajectory may be arbitrary and complex. Results of this simulation are saved in memory and used as nominal trajectory for linearization. Aeroelastic, sloshing and other affects are proposed to give small increments for vehicle motion on vehicle designing stage. For this reason it is possible to use linear models of mentioned effects. If the increments will be large, the vehicle will likely break up and construction or control system must be changed. Results of design and simulation can be saved in database and/or output in graphical 3-D or 2-D postprocessor.

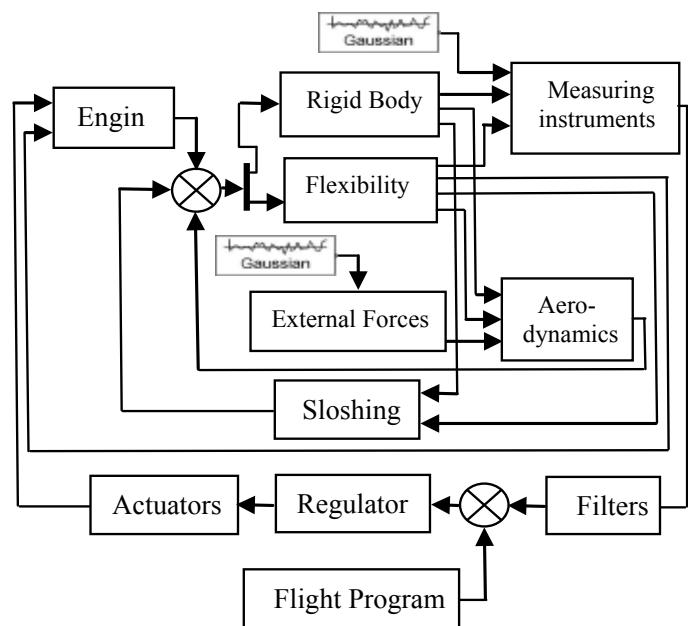


Fig.1. The simplified block diagram of control system for flexible vehicle

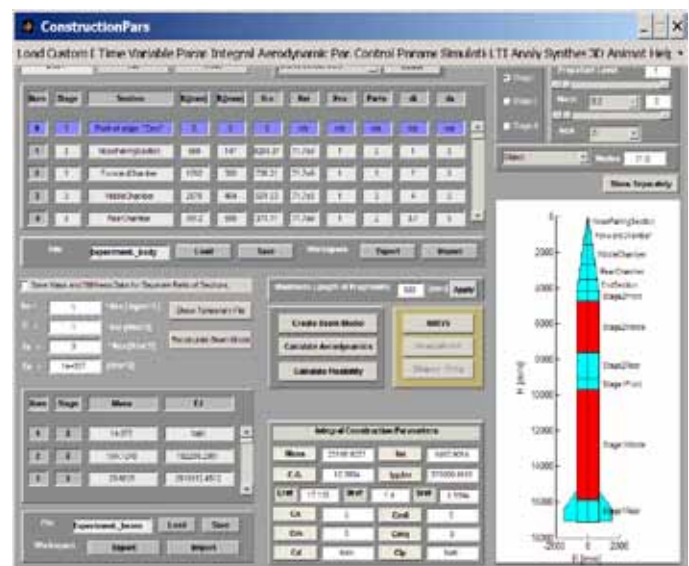


Fig.2. Initial window of the program package

3. AERODYNAMICS

Distributed and integral aerodynamics forces are calculated in this program block. First of all, the pressure in all points of vehicle surface and for all Mach numbers and angles of attack is calculated.

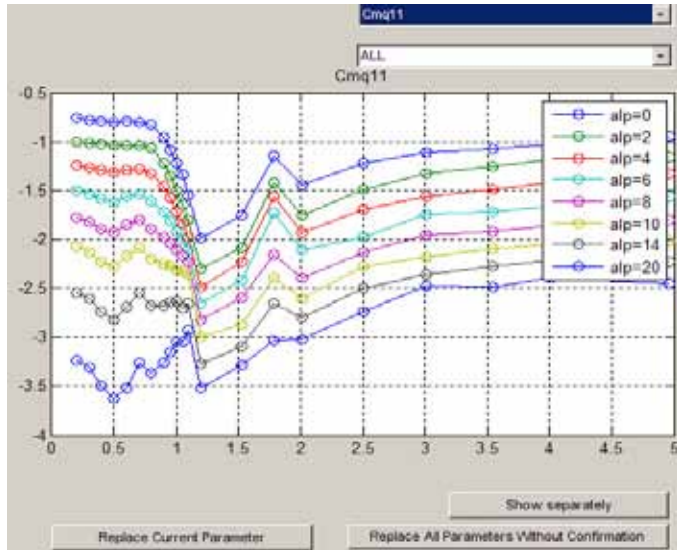


Fig. 5. Normalized integral aerodynamic coefficient C_{mq} for different Mach numbers and angles of attack

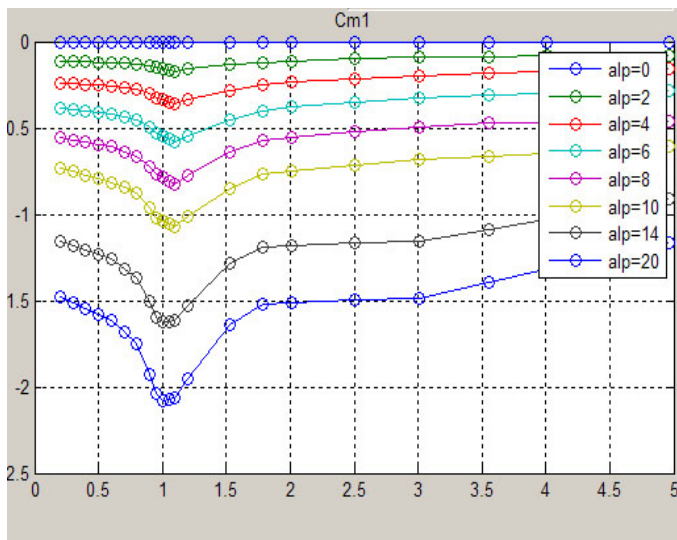


Fig. 6. Normalized integral aerodynamic coefficient C_m for different Mach numbers and angles of attack

Then the pressure is integrated for ring cross-sections along the length of the vehicle. Allocation of the pressure in the aircraft surface is illustrated in Fig. 6 by the conventional colours. Description of this procedure is described in [5].

4. SLOSHING

It is well known that the dynamic effect of liquid sloshing can be roughly approximated by replacing the liquid mass with a rigid mass plus

harmonic oscillator. The oscillator parameters are the function of tank diameters, liquid level, etc. Sloshing liquid generates forces and moments. So the varying vehicle moment of inertia results in oscillations of vehicle c.g. position [8].

5. MODELS OF LOCAL EXTERNAL FORCES AND MOMENTS

All distributed and local loads are stochastic processes in wide band of frequencies. The in-depth physical description of these processes is very complex. Process of formation, development and vortex break-down depends rather complex also on the shape of object, its angular orientation, elastic deformations of a body, a velocity and an altitude of flight. The main influence on elastic oscillations is made by low-frequency external forces in frequency band from zero up to frequencies of second and third harmonics. The main synchronizing factor of a vortex break-down and appearance of external forces is atmosphere turbulence.

Even at a constant value of an object velocity in the atmosphere the vortices are formed. These vortices generate complex and time-varying pattern of local loads distribution on a surface of object. At high speed of flight in separate parts of vehicle there are local peaks of pressure. For their modeling it is important to define the zones of applying the large local loads and their varying in time. Usually these zones are arranged close to the transitions from conical surface to cylindrical one or in places of joints of surfaces of different more complex forms. Designers of vehicles usually aim to avoid such roughness, but it is not possible to remove them completely. Models for the description of the most typical factors, leading to local loads, are described here. Such factors are: a constant lateral wind with taking into account vortex generation, vortex generation in the field of joining of the nose cone and the cylinder, vortex generation in places of joints of separable stages, effect of vortices in the area of stabilizing fin. Description of external forces and moments was given in [5].

6. FLEXIBILITY

The equation of elastic line flexible displacements from the longitudinal neutral axis looks like

$$\Delta \mathbf{M} \ddot{\mathbf{q}} + \Delta \mathbf{\Xi} \dot{\mathbf{q}} + \mathbf{q} = \Delta \mathbf{f} \tag{8}$$

where $\mathbf{q}(t)$ is the deflection of elastic line from the longitudinal axis; Δ is the symmetrical inverse of stiffness matrix; \mathbf{M} is the diagonal the mass matrix; $\mathbf{\Xi}$ is the symmetrical structural damping matrix; \mathbf{f} is distributed load.

Equations which are used for simulation of flexible motion are given in [7].

This approach for description of flexible oscillations allows regulating the dimension of the vehicle mathematical model. The permissible degree of simplification is easily controlled by comparison of modeling outcomes with different number of the elastic vibrations modes.

Such approach allows to reduce considerably the time necessary for the analysis and synthesis of control system, and to simulate the flight at any trajectories without loss of accuracy.

7. CONTROL SYSTEM DESIGN

Mathematical models of all mentioned modules form unique nonlinear model which describe the flight of the aerospace vehicle in atmosphere. It is possible to calculate linear approximations for each instant of the flight. The program allows to perform linearization automatically for arbitrary instants of flight and to convert linear model from one form to another. In Fig. 9 Bode diagram for different instants of time after start for flexible launcher is shown. The complexity of the flexible launcher model determines the necessity to use special smart methods of the control design.

Dependence of vehicle dynamic characteristics from time and stage of flight hampers to the control system design. One of the possible approaches to the synthesis of such algorithm was described in [7].

8. CONCLUSION

- Universal software program to research dynamic properties and simulate flight for different types of flexible vehicles may be used on the initial stages of various types missiles design.
- Designed mathematical models make the basis of program modules for the analysis of dynamic properties and modeling of flexible vehicle.
- Program modules allow investigating the influence of different physical effects, such as flexibility, sloshing, sluggishness of engines, local angle of attack and local angle of slide on dynamic properties of vehicle.
- Outcomes of testing have shown efficiency of the program at simulation of aerospace craft in view of aerodynamic local loads.

References:

- [1] Kolesnikov K.S. Missiles dynamics. Moscow, Mashinostroenie, 350 p. 1980 (in Russian).
- [2] Blakelock, J.H. Automatic Control of Aircraft and Missiles. John Wiley & Sons, Inc., 285 p. 1967
- [3] Mishin, V.P. Rocket Dynamics. Mashinostroenie, Moscow 1990 (in Russian).
- [4] Kohsetsu, Y. Simplified Method of Analysis of Structural Vibrations of Asymmetric Rockets. Trans. Jpn. Soc. Mech. Eng., Vol. 63, No. 612, p.2627-2634 1997 (in Japanese).
- [5] Panferov A.I., Nebylov A.V., Brodsky S.A. Theory and Software Package for Simulation and Smart Control Design for Complex Aerospace Vehicles/ 18th IFAC World Congress, Milano (Italy) August 28 - September 2, 2011 p. 3003-3008
- [6] Sestieri, A. and S. Ibrahim. Analysis of errors and approximations in the use of modal coordinates. Journal of sound and vibration, Vol. 177, No.2, pp. 145-157.1994
- [7] Panferov A.I., Nebylov A.V., Brodsky S.A. Mathematical Models and Control System Designing for Flexible Missile 4th International Conference on Recent Advances in Space Technologies RAST 2009, 11-13 June 2009, Istanbul, TURKEY, 2009
- [8] Nebylov A.V., Panferov A.I., Brodsky S.A. Mathematical Models, Designing, Analysis and Synthesis of Control Systems of the Complex Flexible Objects. International Conference „Physics and Control“, Saint-Petersburg, 2005
- [9] Eli Livne. Future of Airplane Aeroelasticity. JOURNAL OF AIRCRAFT, Vol. 40, No. 6, November-December 2003, pp. 1066-1088.

Loop Heat Pipes – High-Efficient Heat-Transfer Devices for Spacecrafts Thermal Control Systems

Dr. Yury F. Maydanik, Institute of Thermal Physics, Ural Branch of the Russian Academy of Sciences

Loop heat pipes (LHPs) are passive heat-transfer devices, operating on a closed evaporation-condensation cycle with the use of capillary pressure for pumping a working fluid. LHPs have a high heat-transfer capacity, they are able to operate at any orientation in the field of mass forces and zero gravity, easy to configure, and they provide a great scope for various design embodiments. Heat transfer distance in LHPs can reach tens of meters, and capacity - several kilowatts. The first flight experiments with loop heat pipes have been carried out in 1989 aboard the Soviet spacecrafts "Gorizont" and "Granat". The experiments have shown operability and efficiency of these devices in extreme conditions of the outer space and cleared the way to their practical application in space technology.

The paper presents the basic conditions of LHP operability, various design variants and thermal characteristics of these devices and also some examples of successful application in space technology.

INTRODUCTION

The history of development of LHPs originates from 1972^{1,2}. The appearance of LHPs was a response to the challenge connected with the acute demand of aerospace technology for high-efficient heat-transfer devices with all the main advantages of conventional heat pipes³, but at the same time less sensitive to the change of orientation in the gravity field and http://multitrans.ru/c/m.exe?a=110&t=2289692_2_1&sc=28a acceleration actions.

The LHP conception includes the following main principles:

- the use of fine-pored wicks, which can produce a high capillary head;
- maximum decrease in the distance of the liquid motion in the wick;
- organization of effective heat exchange in the condensation and evaporation zones of the working fluid;
- maximum decrease in pressure losses in the transportation section of the working fluid motion.

The schemes of conventional and loop heat pipes are presented in Fig. 1. For realization of this conception special capillary-porous materials were created on the base of sintered nickel and titanium powders with an effective pore radius of 1-10 μm and a porosity of 55-75%.

Such materials possess a sufficient strength, which allows complex mechanical processing at wicks production, are capable of producing a high capillary pressure and chemically compatible with a wide range

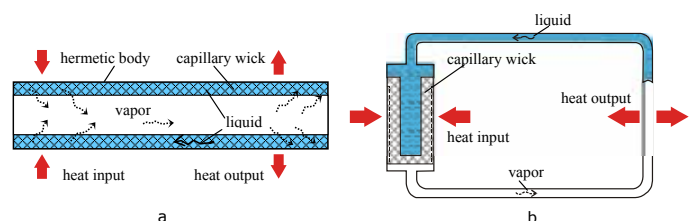


Fig. 1 Schemes of conventional heat pipe (a) and loop heat pipe (b)

of working fluids. Minimization of the distance for the liquid motion in the wick is limited, as a rule, by several millimeters is achieved at the expense of the wick design. A decrease in pressure losses in the transportation section of the LHP is ensured by the fact that for the motion of a working fluid here separate smooth-wall lines are used, which exclude both the thermal and the viscous interaction between counter flows of vapor and liquid. At the present time a wide range of different modifications of these devices, operating efficiently both in ground and space conditions, has been produced on the base of the LHP conception⁴.

¹ Heat Pipe, USSR Inventor's Certificate № 449213, 1974

² Gerasimov Yu.F., Maydanik Yu.F., Shchegolev G.T. et al.: Low-temperature heat pipes with separate channels for vapor and liquid; Journal of Engineering Physics, 28 (6), 1975, pp. 957-960 (in Russian)

³ Dunn P.D., Reay D.A.: Heat Pipes; Pergamon Press, Oxford, 1976

BASIC CONDITIONS OF LHP OPERATION

Theoretical analysis of different aspects of LHPs operation is particularly presented in the publications⁵⁻⁸.

The operation of these devices is based on the same physical processes as those used in conventional heat pipes. These are processes of evaporation and condensation in heat load supply and removal zones, heat transfer in a vapor phase of the working fluid and return of a condensed liquid in the heating zone by means of capillary forces produced in the capillary-porous wick.

According to this, the first condition of LHP operation is determined in the same way as for conventional heat pipes:

$$\Delta P_c \geq \Delta P_v + \Delta P_l + \Delta P_g, \quad (1)$$

where ΔP_c - the capillary pressure produced in the wick; ΔP_v , ΔP_l - pressure losses during the motion of the working fluid in the vapor and liquid phases; ΔP_g - pressure losses caused by the hydrostatical resistance of a liquid column. In weightless state $\Delta P_g = 0$.

The values of ΔP_v and ΔP_l are determined here in accordance with the well-known equations³ for the motion of vapor and liquid in different LHP sections, including the wick. The value of ΔP_g may be determined by the formula:

$$\Delta P_g = (\rho_l - \rho_v) g l \sin \varphi, \quad (2)$$

where ρ_l , ρ_v - the liquid and vapor densities; g - the free fall acceleration; l - the LHP length; φ - the LHP slope angle with a horizontal plane. The value of the capillary pressure is defined by the Laplace formula:

$$\Delta P_c = \frac{2\sigma}{r_c} \cos \theta, \quad (3)$$

where σ - the surface tension coefficient, r_c - the effective radius of wick capillaries, θ - the curve angle of liquid wetting of wick capillary walls.

The second condition of operability, characteristic only of LHPs, is the necessity of producing a sufficient temperature and pressure drop between the evaporating and absorbing surfaces of the wick, which are divided by a relatively thin layer of the capillary structure. This condition may be written as follows:

$$\left. \frac{\partial P}{\partial T} \right|_{T_v} \Delta T_w = \Delta P_{ex}, \quad (4)$$

where $\partial P/\partial T$ - the derivative determined by the slope of the tangent to the saturation line of the working fluid at the point with temperature T_v , average between the temperature of the evaporating and absorbing surfaces of the wick, ΔT_w - the temperature drop between the mentioned temperatures, ΔP_{ex} - the sum of pressure losses on the external areas of the working fluid circulation relative to the wick. This condition is necessary for displacing the working fluid from the vapor line

MATERIALS AND WORKING FLUIDS

The main material for production of LHPs designed for application in space technology is stainless steel. Aluminum alloys are also used.

Sintered nickel and titanium fine-dispersed powders are widely used as materials for wicks. Such wicks are chemically compatible with many low-temperature working fluids, which can be used in http://multitrans.ru/c/m.exe?a=110&t=1625187_2_1&sc=197 space environment^{9,10}.

The choice of working fluids for LHPs is based on the same criteria as for conventional heat pipes, including the following:

- chemical compatibility with the body and the wick
- appropriate temperature range, which should be sufficiently far from triple and critical points
- crystallization temperature

The most suitable working fluids for space environment are ammonia and propylene. The choice criteria of working fluids for LHPs are presented in details in the paper¹¹.

DESIGNS AND LHP THERMAL CHARACTERISTICS

The LHP additional advantage is that allows a wide variety for different design embodiments and achievement of high heat-transfer capacity⁴. They allow producing flexible, ramified, controllable and reversible heat-transfer devices well-adapted to various conditions of arrangement and service.

Fig. 2 shows the experimental examples of miniature LHPs with cylindrical evaporators of diameter 5-6 mm and lines for vapor and liquid 2 mm in diameter. The length of such devices is 200-300 mm and a maximum capacity can reach 200 W.

Fig. 3 presents the external view of a flexible LHP 1.8 m in length, the maximum capacity of which is 100 W. The cylindrical evaporator 10 mm in diameter was equipped with an aluminum interface with dimensions of 60x60 mm for the placing of a source of heat load.



Fig. 2 Miniature LHPs with cylindrical evaporators



Fig. 3 Flexible LHP

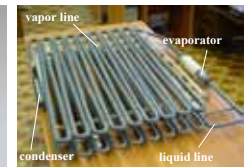


Fig. 4 Ammonia LHP 21 m in length

³ Dunn P.D., Reay D.A.: Heat Pipes; Pergamon Press, Oxford, 1976 and the condenser during the LHP start-up and operation.

⁴ Maydanik Yu.F.: Loop heat pipes; Applied Thermal Engineering, 25, 2005, pp. 635-657

⁵ Maydanik Yu.F., Fershtater Yu.G.: Theoretical basis and classification of loop heat pipes and capillary pumped loops; Keynote lecture X-7, Proc. of 10th International Heat Pipe Conference, 1997, Stuttgart, Germany

⁶ Ku J.: Operating characteristics of loop heat pipes; SAE Paper 2007, 1999

⁷ Kaya T., Hoang T.T.: Mathematical Modeling of LHPs and Experimental Validation; Journal of Thermophysics and Heat Transfer, v.13, №3, 1999, pp. 2557-2569

⁸ Mishkinis D., Ochterbeck J.M., Sottke C. et al.: Non-dimensional analysis and scaling issues in loop heat pipes; AIAA Paper 2002-0341, 2003

⁹ Kuskov G.V., Maidanik Yu.F.: Investigation of the structural and hydraulic properties of capillary porous materials for heat pipes; Journal of Engineering Physics, 50 (4), 1986, pp. 411-416

¹⁰ Maidanik Yu.F., Kuskov G.V.: Titanium porous materials for the capillary structures of heat pipes; Soviet Powder Metallurgy and Metal Ceramics, 22 (1), 1983, pp. 33-35

¹¹ Fershtater Yu.G., Maydanik Yu.F.: Criteria for selection a working fluid for an "anti-gravity" heat pipe; Heat transfer Soviet research, 19 (6), pp. 114-118

FLIGHT EXPERIMENTS OF LHP

The first flight experiment with LHPs was conducted in 1989 aboard the Russian spacecrafts "Gorizont" (NPO Applied Mechanics) and "Granat" (NPO Lavochkin Association)^{12,13}. The scheme and the external view of the experimental module "Gorizont" are shown in Fig. 5.

The experiment aboard the spacecraft "Gorizont" was performed with an LHP with three parallel evaporators 24 mm in diameter combined with an aluminum plate, on which a heat load simulator of capacity varying from 40 to 120 W was located. The condenser was made in the form of parallel pipes 6 mm in diameter, joined to the panel of a radiator. Freon-11 was used as a working fluid.

The experiment aboard the spacecraft "Granat" was carried out with an LHP 4 m in length with an evaporator 12 mm in diameter. The source of heat load was solar energy, which was concentrated with the help of a special panel, connected with the evaporator. Propylene was used as a working fluid. The scheme of the experimental module "Granat" and the external view of the LHP are presented in Fig. 6.

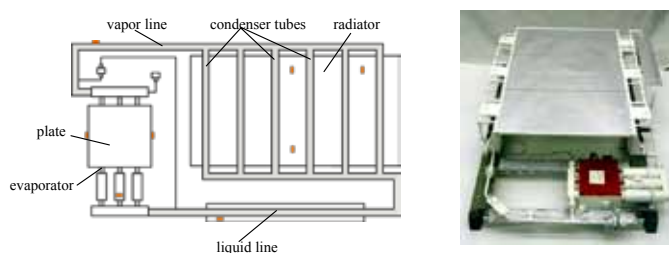


Fig. 5 Scheme and external view of "Gorizont"

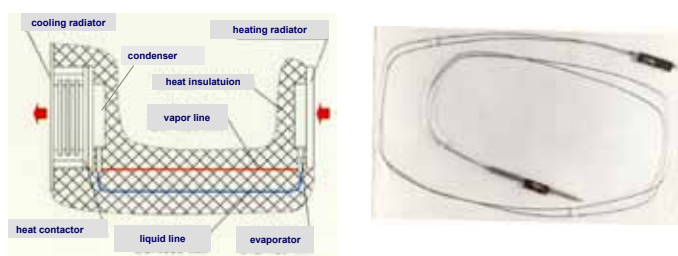


Fig. 6 Scheme of experimental module "Granat" and external view of LHP

Flight experiments have shown the LHP working capacity in weightlessness conditions and opened the flood-gates for real application of these devices in thermal control systems of spacecrafts.

APPLICATION OF LHPs IN SPACECRAFTS THERMAL CONTROL SYSTEMS

A unique thermal control system including six LHPs was installed aboard the Russian spacecraft "Mars-8", launched in 1996 according to the "Mars-96" Program¹⁴.

In 2003 the spacecraft "Yamal – 200" was put into orbit, on board which the TCS with 14 LHPs has been successfully operating already in the course of 8 years. Thermal control systems with loop heat pipes have also been operating on board the Russian spacecrafts "MIM-1", "Fobos-Grunt", "Spectr", "Electro", and "Yubileiny".

In the USA the first actual application of LHPs took place in January, 2003. Two propylene LHPs were used in the thermal control system "Geoscience Laser Altimetry System (GLAS)" on board the spacecraft "ICESat"¹⁵.

LHPs have also found an application in European space programs. There are thermal control systems of the martian probe aboard the spacecraft "Netlander", the magnetic alpha spectrometer on board the International Space Station and also the TCS aboard the European space platforms Eurostar 3000. These two platforms were launched in 2005 and each of them have two LHPs 6 m in length with capacity of 400 W operating in the temperature range from -30 °C to +80 °C¹⁶.

A high heat-transfer capacity of LHPs, a low thermal resistance, mechanical flexibility and excellent adaptability to different conditions of location and service were in full used in creating all these and other thermal control systems.

CONCLUSION

Loop heat pipes are high-efficient heat-transfer devices which have demonstrated their efficiency in thermal control systems on board Russian, American and European spacecrafts where they have been successfully used for long years. In perspective these devices will be used along with conventional heat pipes in an increasing number as a quite usual component of the thermal control system of spacecrafts for different purposes.

¹² Maidanik Yu., Fershtater Yu., Pastukhov V., Goncharov K., Zagar O., Golovanov Yu.: Thermoregulation of Loops with Capillary Pumping for Space Use; SAE Paper 921169, 1992

¹³ Maidanik Yu.F., Fershtater Yu.G., Goncharov K.A.: Capillary-pumped Loop for the Systems of Thermal Regulation of Spacecraft; Proc. of 4th European Symposium on Space Environmental and Control Systems, Italy, 1991, pp. 87-92

¹⁴ Kozmin D. et al.: Loop Heat Pipes for Space Mission "Mars 96", 26th International Conference on Environmental Systems; USA, 1996, Paper № 961602

¹⁵ Baker C.L. et al.: Geoscience laser altimetry system (GLAS) on-orbit flight report on the propylene loop heat pipes; Proc. of International Two-Phase Thermal Control Technology Workshop, the Netherlands, 2003

¹⁶ Mena F.: In Orbit Heritage of Loop Heat Pipes on Eurostar 3000 Spacecraft; Proc. of International Two-Phase Thermal Control Technology Workshop, the Netherlands, 2008

References:

- [1] Heat Pipe, USSR Inventor's Certificate № 449213, 1974
- [2] Gerasimov Yu.F., Maidanik Yu.F., Shchegolev G.T. et al.: Low-temperature heat pipes with separate channels for vapor and liquid; *Journal of Engineering Physics*, 28 (6), 1975, pp. 957-960 (in Russian)
- [3] Dunn P.D., Reay D.A.: *Heat Pipes*; Pergamon Press, Oxford, 1976
- [4] Maidanik Yu.F.: Loop heat pipes; *Applied Thermal Engineering*, 25, 2005, pp. 635-657
- [5] Maidanik Yu.F., Fershtater Yu.G.: Theoretical basis and classification of loop heat pipes and capillary pumped loops; Keynote lecture X-7, Proc. of 10th International Heat Pipe Conference, 1997, Stuttgart, Germany
- [6] Ku J.: Operating characteristics of loop heat pipes; SAE Paper 2007, 1999
- [7] Kaya T., Hoang T.T.: Mathematical Modeling of LHPs and Experimental Validation; *Journal of Thermophysics and Heat Transfer*, v.13, №3, 1999, pp. 2557-2569
- [8] Mishkinis D., Ochterbeck J.M., Sodtke C. et al.: Non-dimensional analysis and scaling issues in loop heat pipes; AIAA Paper 2002-0341, 2003
- [9] Kuskov G.V., Maidanik Yu.F.: Investigation of the structural and hydraulic properties of capillary porous materials for heat pipes; *Journal of Engineering Physics*, 50 (4), 1986, pp. 411-416
- [10] Maidanik Yu.F., Kuskov G.V.: Titanium porous materials for the capillary structures of heat pipes; *Soviet Powder Metallurgy and Metal Ceramics*, 22 (1), 1983, pp. 33-35
- [11] Fershtater Yu.G., Maidanik Yu.F.: Criteria for selection a working fluid for an "antigravity" heat pipe; *Heat transfer Soviet research* 19 (6), pp. 114-118
- [12] Maidanik Yu., Fershtater Yu., Pastukhov V., Goncharov K., Zagar O., Golovanov Yu.: Thermoregulation of Loops with Capillary Pumping for Space Use; SAE Paper 921169, 1992
- [13] Maidanik Yu.F., Fershtater Yu.G., Goncharov K.A.: Capillary-pumped Loop for the Systems of Thermal Regulation of Spacecraft; Proc. of 4th European Symposium on Space Environmental and Control Systems, Italy, 1991, pp. 87-92
- [14] Kozmin D. et al.: Loop Heat Pipes for Space Mission "Mars 96", 26th International Conference on Environmental Systems; USA, 1996, Paper № 961602
- [15] Baker C.L. et al.: Geoscience laser altimetry system (GLAS) on-orbit flight report on the propylene loop heat pipes; Proc. of International Two-Phase Thermal Control Technology Workshop, the Netherlands, 2003
- [16] Mena F.: In Orbit Heritage of Loop Heat Pipes on Eurostar 3000 Spacecraft; Proc. of International Two-Phase Thermal Control Technology Workshop, the Netherlands, 2008

Single photon laser altimeter and lidar in space missions

Ivan Procházka¹, Josef Blažej¹, Vojtěch Michálek^{1,2}, Michael Vacek^{1,2}, Marek Peca²

¹*Czech Technical University in Prague, Břehová 7, 115 19 Praha 1, Czech Republic*

²*Aeronautical Research and Test Institute, Beranových 130, 199 05 Prague, Czech Republic*

We are reporting on research, development, indoor tests, and operational results of the single photon laser altimeter and lidar that are being developed in our lab for several planetary missions. The Czech Technical University in Prague has been involved in research and development of the lidar for the space applications in the missions to the planet Mars since 1989. Following our contribution to the Soviet mission PHOBOS, our group has been invited to participate in Mars projects, as well. The ultimate goals of the projects were to establish an altimeter for the aerostat probe on Mars, to monitor the atmospheric dust and clouds, nadir looking, and to monitor the atmosphere dust and clouds from the landing apparatus, zenith looking. Requirements are achievable using single photon counting approach and detector based on silicon avalanche photodiode operated in a special mode with single photon detection capability in optical wavelength region. This experience has been also used in the NASA mission Mars Polar Lander 98. The single frequency lidar based on solid state photon counting technology was one of the sensors onboard the Lander. The capabilities of our laboratory for time-resolved single photon detection applicable for laser altimeters and lidar research and development will be presented.

SOLID STATE PHOTON COUNTING

Solid state photon counting is a fast emerging experimental technique, which is opening new possibilities in optical measurements and diagnostics. The most elaborated photon counting method based on a semiconductor technology is using the avalanche multiplication of carriers. This technique is based on the avalanche photodiode, which is pulse biased above its breakdown voltage [1]. The recent achievements in the solid state photon counting technology enable to construct detectors capable to response to both single and multiple photons signals [2] with extremely high timing resolution in the wavelength range spanning from x-ray up to a near infrared. The concept of the detector enables to avoid any analog signal processing: amplification and discrimination, which are usually both temperature dependent and power consuming. All the signal processing is based on logic circuits, only.

PHOTON COUNTING CAPABILITIES

The availability of the solid state photon counter is opening a full spectrum of new possibilities in optical measurements. Obviously, the photon counting enables to register the ultimately weak optical signals, but this is just one of many possible applications. The photon counting

principle permits to measure light intensities with high precision and stability. The quantum nature of the light on one hand and the capability to count the number of the light quanta on the other hand enable to measure the analog value – light intensity by a purely digital way. The analog to digital conversion is carried out by the quantum nature of the light and the detection principle. The absence of analog signal processing: amplification, discrimination and conversion results in extreme (even absolute) measurement stability, linearity, reproducibility etc. Additionally, the detector is quite versatile: the same detector may be employed for the precise timing of weak optical pulses in altimetry or lidar (Light Detection And Ranging) and as an optical sensor for photometry with extreme stability, dynamical range and linearity. These features are of special interest for space borne sensors.

Our University had developed and tested the solid state photon counter based on silicon avalanche photodiode and an active quenching and gating circuits within the last two decades. Numerous applications of this detector have been found in picosecond time resolved spectroscopy, fiber optics diagnostics and sensors, millimeter precision satellite laser ranging, lidar, industrial air pollution sensors, quantum key distribution, and several space borne projects. For every application, the detection avalanche structure and the active quenching and gating circuit have been optimized. Our solid state photon counting detector based on silicon avalanche photodiode has been selected for space applications for its unique properties: low operating voltage, low power

consumption, and high radiation damage threshold. The detector is capable to operate in both gated and not gated operational modes. To keep the appropriate biasing of the detection diode in the extreme temperature range of -80 to $+50$ degree Celsius, the detector biasing circuit has been designed and manufactured. No temperature stabilization is required within the entire temperature range.

PLANETARY ALTIMETRY AND LIDAR

Planetary altimetry was the first space borne application of our solid state photon counting detector. Our experience acquired in satellite laser ranging projects permitted to design and construct a compact laser altimeter for the deep space mission Mars'92 (96) prepared in the Soviet Union late nineties [3]. The altimeter used a laser diode delivering nanoJoules of energy in the near infrared in pulses 90 ns long. The echo signal has been detected by the solid state photon counter. The transmitting and receiving optics has been 50 and 20 mm in diameter respectively.

The total mass of the device was 900 g, 400 g for the optical head, 400 g the electronics and 100 g for cabling. The average power consumption of the device was 30 mW with a peak power consumption of 4 W used to heat up the laser diode in the initial phase. The system was capable to range solid objects within the range of 0 to 5 km. Late nineties, the identical device has been installed on board the NASA Mars Polar Lander (MPL) with the objective to operate as an atmospheric lidar and to investigate the Mars atmosphere [4]. The flight unit of the altimeter is in Figure 1.

In a lidar mode it was capable to detect clouds and dust within the range up to 1 km. In the passive mode, the Sun light scattered in the high atmosphere has been recorded as a time series, what enabled to determine the concentration of light scattering particles in the atmosphere in the height up to 100 km. These two applications demonstrate the photon counting concept versatility – the same device can be used for altimetry, lidar and precise photometry.



Fig. 1: The flight unit of lidar on MPL'98. Optical part (silver block with apertures) with two lasers and receiver; and electrical part (black cylinder).

Our experience acquired in previous planetary missions together with the numerical models [5] show, that the altimetry can be performed from the orbit height exceeding 1000 km using the moderate size, radiation and heat resistant optical telescope. The photon counting altimeter / lidar is a powerful tool for the planetary atmosphere studies, as well. The photon counting lidar is capable to analyze the planetary atmosphere, dust and aerosol distribution.

LONG RANGE RANGING

The planetary laser transponder has been proposed to provide range measurements on the inter-planetary scale with decimeter accuracy [6]. It should provide, among others, high accuracy deep space navigation. To detect the optical pulses at the remote side of the transponder link, the photon counting detector with nanosecond timing resolution is required. The solid state photon counter based on our silicon avalanche detector has been optimized for the transponder application. It is capable to operate within extreme temperature range, employing low voltage biases only, consuming milliWatts of power. The timing resolution is below 100 ps, the quantum efficiency in the spectral range of 500 – 900 nm exceeds 10 %.

The Time Transfer using Laser Link (T2L2) experiment is based on detection of optical pulses with energies in the range of single to thousands of photons [7]. It will provide synchronization of time scales with the precision of 10 ps on an intercontinental scale. This time scales synchronization will permit to carry out the precise navigation on an inter-planetary scale by means of one way ranging. The silicon based photon counting avalanche photodiodes developed by our group have been selected for both the ground and space segments.

The application of solid state photon counters in the experiment “Astrodynamical Space Test of Relativity using Optical Devices” (ASTROD) program [8] or EJSM/Laplace mission [9] program are under consideration. The several applications in time transfer missions for time scales synchronization with picosecond precision and accuracy over planetary distances have been reported in previous proceedings of this workshop [10].

TECHNOLOGY DEMONSTRATOR

The European Space Agency (ESA) has nominated the photon counting altimeter as one of the attractive devices for planetary research for the next decade. The first mission in view is Mercury with scheduled launch in 2010. The requirements on the device are rather strict: total mass below 5 kg, power consumption below 10 W. Additionally, the harsh radiation environment near Mercury requires, among others, small optical aperture of the device. Recently, the technology demonstrator of the altimeter and atmospheric lidar is under development at our group. The altimeter technology demonstrator is based on the diode pumped frequency doubled Nd: YAG microlaser delivering 1 μ J at 532 nm in 1 ns long pulses with the repetition rate of 10 kHz. The electronics is based on a modular kit consisting of the programmable gate arrays and a control processor and software. The optical part of the altimeter is scaled down to simulate the real background count rate scenario and to reduce the energy budget link by a factor of 104 at the same time. The demonstrator [11] should be capable to range objects at distances 0 – 5 km in both night and day time. It will be used to develop data processing and filtering algorithms and to verify energy budget under various conditions.

CONCLUSION

The solid state photon counting has demonstrated its capabilities for laser altimetry, lidar for atmospheric studies, precise photometry and precise timing for space navigation. The technology is available, it is

compatible with space applications foreseen: low mass, low power, rugged, radiation resistant. European labs are playing leading role in solid state photon counting technology development and applications.

ACKNOWLEDGEMENTS

This research has been supported by numerous grants provided by the Grant Agency of the Czech Republic, Ministry of Education of the Czech Republic, and the national and international grant agencies, as well. The recent publication has been supported by the research framework MSM6840770015.

References:

- [1] Procházka I., Sopko B., Hamal K., Mácha I.: Novel Contribution in Branch of Ultra Fast Condensed Matter Spectroscopic Photon Counting Systems; *Microelectronics Engineering* 19, pp. 643-648, 1992.
- [2] Blažej J.: Photon number resolving in Geiger mode avalanche photodiode photon counters, *Journal of Modern Optics* 51 (9), pp. 1491-1497, 2004.
- [3] Pershin S. M., Linkin S., Makarov V., Prochazka I., Hamal K.: Space-born altimeter based on a semiconductor laser transmitter and a single photon diode receiver; *Technical Digest Series of CLEO '91*, vol. 10, p. 520, 1991.
- [4] Linkin V. M., et al.: Lidar for Mars Polar Lander, [online] [cit. August 6 1999] <<http://mars3.jpl.nasa.gov/msp98/lidar/iki.html>> and in Russian compact lidar for NASA "Mars surveyor program 1998", NASA no. 19980227632, 19th Int. Laser Radar Conference, 1998.
- [5] Blažej J., Prochazka I.: The simulator of the photon counting planetary altimeter; *Proc. SPIE* 6677, p. L6771, 2007.
- [6] Degnan J. J.: A detailed analysis of an Earth-Mars laser transponder link; in *Proceedings of 12th International workshop on laser ranging*, Matera, Italy, [online] [cit. September 28 2011] <http://cddis.gsfc.nasa.gov/lw12/docs/Degnan_trasponder.pdf>, 2000.
- [7] Samain É., et al.: Time transfer by laser link – the T2L2 experiment on Jason-2 and further experiments; *International Journal of Modern Physics D* 17 (7), pp. 1043-1054, 2008.
- [8] Tian-Yi Huang, et al., Space Test of Relativity and Gravitational-Wave Astronomy, *Int. Journal of Modern Physics D* 11 (7), pp. 947-1158, 2002.
- [9] Prochazka I., et al.: Optical receiver for one-way ranging to the EJSM/Laplace mission to Jupiter, in *Proc. of EJSM Instrument Workshop*, Laurel, Maryland, p. 42, 2009
- [10] Prochazka I., Blažej J.: Photon Counting Detectors for Laser Ranging and Laser Time Transfer Missions; *Transfer* 2010 (13), pp. 28-32, 2010.
- [11] Blažej J., Prochazka I., et al.: Photon counting laser altimeter for planetary exploration - the technology demonstrator, *J. Of optics A – Pure and applied optics* 9 (6), pp. S98-S101, 2007.

Time-to-Digit Converter Based on Radiation-Tolerant FPGA

Marek Peca^{1,2}, Michael Vacek^{1,2}, Vojtech Michalek^{1,2}

¹ Vyzkumny a zkusebni letecky ustav, a. s.

² Ceske vysoke uceni technicke v Praze, Fakulta jaderna a fyzikalne inzenyrska, Katedra fyzikalni elektroniky

Architecture of a time-to-digit converter (TDC) is presented. TDC is an electronic device which measures time of arrival of discrete electronic pulses, with respect to reference time base. Our work on TDC is motivated by its applications in field of long-range laser distance measurement and time synchronization. Unlike earlier time interpolation methods, we have chosen all-digital approach based on pulse propagation through tapped delay line. We do not expect it could outperform recent invention of time interpolation using narrow-band filter excitation [1,2]. However, our approach relies on a standard digital circuitry only. With space applications in mind, we are implementing the TDC into a space qualified, radiation tolerant field-programmable gate array (FPGA).

On top of related works on all-digital, delay line TDCs, we try to gather more complete information about the sampled pulse. It is done by sampling whole bit vector, corresponding to all of the delay line taps. A calibration method based on random pulse source is discussed, including preliminary results. Currently, the TDC prototype is in agreement with laboratory time interval counter up to 80 ps of systematic error plus 49 ps RMS of jitter. RMS deviation between actually measured jitter distribution and normal distribution function is 3 ps RMS, giving an insight of absolute accuracy limit of our approach within the given FPGA platform.

1. INTRODUCTION

Mankind has measured time since time immemorial. High precision time measurements are used in huge amount of applications around us today. Our key motivation was to develop suitable Time-to-Digit Converter (TDC) for space applications, especially, lidar applications based on photon counting approach (planetary altimetry, time synchronization, etc.). Such a TDC have to be radiation tolerant and compact with low power consumption. For this reason, an implementation of TDC in single FPGA chip was chosen as appropriate solution. Despite our original motivation, we try to develop as general TDC as possible with the constraints due to single FPGA approach.

2. MEASUREMENT APPROACH

2.1. What is TDC?

General principle of time-to-digit conversion is as follows. Ticks of a high stable and low noise reference clock is counted by a digital coun-

ter. In this manner, time can be measured in chunks of reference clock period, which is, however, insufficient if precision higher than is required. For this reason, time interpolation is employed while measuring times with resolution higher than clock period.

Analog interpolation and digital delay line approaches belong to usual time interpolation methods. Analog time interpolation is based usually on charging a capacitor with constant current between reference clock ticks. Elapsed time is then proportional to charge accumulated at the capacitor. Currently the best interpolator known to us is based on narrow-band (e.g. SAW) filter excitation by incoming pulse and sampling of impulse response by analog-to-digital converter [1,2].

The digital approach employs tapped delay line on which the incoming pulse propagates. Each part of the line is sampled regularly by reference clock and the pulse position determine time elapsed since previous clock tick. The delay line can be either active or passive.

Active line is formed by chain of active elements with defined delay such as buffers, latches, multiplexers, or gates [4]. The performance of

-router timing "best effort" algorithms cause that the line is routed towards snapshotting flip-flops in the way it has the shortest possible delay. Nevertheless, this is an undesired behavior since it deteriorates line linearity and shortens the total propagation delay of the line. A posteriori analysis of placer-and-router tool designs showed that a flip-flop branch topology gives acceptable and promising routing results (see Sec 4.2, $M=2400$ design). Evenly and vertically spaced flip-flops deliver sufficient precision and compensate the increased inter-block delay simultaneously.

The total delay of the line is apparently proportional to the line length. It is highly intended to implement as long line as possible with an appropriate number of snapshotting flip-flops. Essentially, the line should be substantially longer than reference clock period (Sec. 3.2), and higher number of taps increases time-domain sampling resolution.

Owing to the impossibility of arbitrary routing, the maximum delay of the line is restricted by the dimensions of FPGA. It is about 5 ns for a given FPGA. Additional elements with a defined position may be inserted in the passive line to work around this issue; however, it brings certain trade-offs. Multiplexer elements are typically used. By these means, an arbitrary long delay line may be designed, the number of available flip-flops being the only restriction.

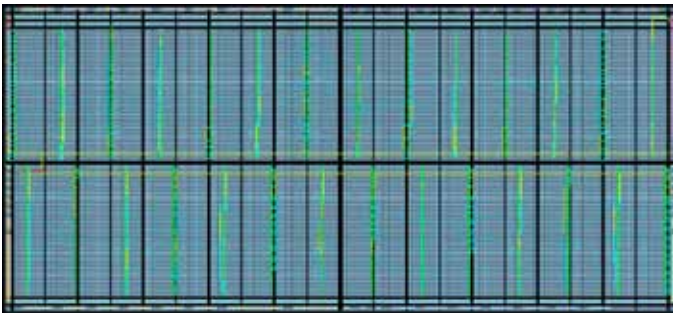


Fig. 2: Internal FPGA structure (tile grid); yellow, green, red, and blue lines denote the different net class of the passive delay line

3. CALIBRATION AND TESTING

A calibration is necessary to use passive delay line TDC implemented within FPGA. Since there is little control over FPGA net routing, there is no prior knowledge of actual tap delays. Even more, the exact time order of taps (flip-flops) along the line is not known until calibration.

3.1. Calibration methods

Given a TDC with reference clock and one event pulse input, following calibration tools are possible:

- accurate time interval source;
- accurate reference TDC instrument;
- random pulse source.

The accurate time interval source may consist of a pulse generator, providing pulses with defined delay with respect to reference clock edge. It may be also calibrated transmission line, cable of fixed length or variable line stretcher [5], whose are also capable to provide defined pulse delay. Another solution is to measure time intervals from some source with another, calibrated TDC.

Both of the methods mentioned above require somewhat accurate or at least complex equipment. Completely different approach is to use a random pulse source as a base for calibration. Provided the reference clock is accurate, a huge amount of pulses arriving at random times is able to provide sufficient data for calibration by histogram.

3.2. Calibration by histogram

The calibration by histogram is based on following assumptions:

- the frequency of reference clock is defined and stable;
- incoming pulses have known probability distribution in time, modulo clock period;
- the sample set of pulses is sufficiently large and representative.

The most likely and simplest assumption is that pulse event time within one clock period follows uniform probability distribution: $t \sim U(0, T_0)$, where T_0 is reference clock period and t is pulse arrival time modulo T_0 . Almost any signal source, which is not coherent with reference clock, will satisfy the assumption over long term measurement.

After collecting the huge amount of data, a histogram is created. Each pulse yields a bit vector of length M , corresponding to M taps of delay line. The sum of all bit vectors yield histogram of M bins.

Under assumption of negligible flip-flop jitter ($\sigma_j \ll \Delta t$, where σ_j stands for timing uncertainty and Δt is a representative inter-tap delay) and $T_{max} \leq T_0$, the histogram tells us two important things [3]:

- absolute order of taps along the line;
- ratio of tap delays.

The height of histogram in n -th bin is proportional to probability that $t < t_n$, where t_n is respective input to tap delay. Of course, the proportionality holds only when law of large numbers (LLN) apply. After sorting bins according to their height, first difference of sorted histogram is then proportional to Δt between neighbour taps. Keep in mind, that neighbour is meant no longer in location sense, but in time domain.

The task remaining for useful calibration is, how to determine absolute time quantities of the observed tap delays. Here the prior knowledge of T_0 enters the game. In case $T_{max} < T_0$, some of the random pulse edges are not visible within the bit vector at all, it reads all zeros or all ones, since the event occurred in $T_{max} < t < T_0$. Therefore, T_{max}/T_0 should be proportional to ratio of observed vs. missed pulses (under LLN).

When $T_{max} > T_0$, the number of missed pulses should go to zero and it is more difficult to determine T_{max} from T_0 . If $T_{max} > T_0$, the pulse will occasionally appear twice in the following bit vectors. If $T_{max} > 2T_0$, the pulse should always occur twice. Then, the T_{max} may be inferred from histogram and the fact that the two occurrences are displaced by T_0 .

It should be noted, that TDC with property of $T_{max} < T_0$ is not much useful in practice, due to the missed pulses. On the other hand, it is easy to analyze and explain, and this is why we describe mostly such a design in following text.

The last note should be said about the jitter mentioned. It is clear, that presence of jitter tends to smooth histogram by occurrences of "leap"

bit vectors, such as ...00010111..., ...000100111... etc. They cause systematic error in histogram and are not being canceled out by LLN. We still have not developed sound technique for jitter estimation and compensation during calibration, so we will continue with the plain method described above.

4. MEASUREMENT

4.1. Experimental setup

In Fig. 3, there are configurations used for calibration and testing of the TDC. First of them is a practical realization of the random pulse source by an oscillator with large phase-noise, unrelated in frequency and not coupled by any means to the reference clock oscillator. In our case, the reference oscillator has been a crystal oscillator, while the random pulse source has been an RC astable generator formed around famous NE555 chip. The care was taken to isolate NE555 from the FPGA and crystal oscillator. Independent power supplies have been used. NE555's output has been buffered by a pulse/delay generator DG535, which served merely as a pulse shaper in this first configuration.

Second configuration employs DG535 as a delay generator which is triggered by pulse derived from reference clock. By means of DG535, various delays with respect to sampling clock can be set and each point of the delay line can be tested appropriately.

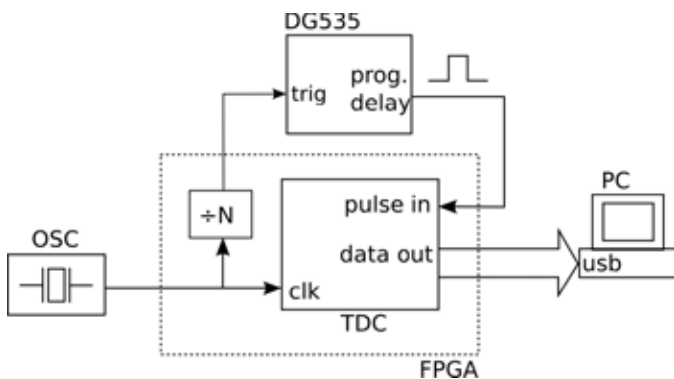


Fig. 3: Experimental setup; (a) calibration (b) measurement

As confirmed by experiments, a particular care should be taken for the calibration procedure. First, it is necessary to feed the TDC with pulses of the same shape (logic standard, slope). Also, to obtain good statistical results even for rare phenomena, really huge amount of calibration data is required (several gigabytes of raw data has been taken during night).

4.2. Results

Let us first examine first difference of sorted histograms, generated overnight by NE555. Fig. 4 shows histograms for two different TDC FPGA designs. The first is $M=320$, one straight flip-flop string along the chip. The second is $M=2400$ (non-effective length cropped out), zig-zag lines around the chip.

The most noticeable (and unpleasant) feature of the first design is presence of peaks, meaning long inter-tap delays and thus locally very low resolution: $< \pm 88$ ps, i.e. $\Delta t < 176$ ps. The nine peaks correspond very faithfully to the chip topography, where there are transversal ribs

between ten spaced blocks of cells. The other disadvantage of this design is $T_{max} \approx 3.5$ ns, what is significantly lower than $T_0 = 10$ ns, resulting in 65% event loss. However, such a large tap delay deviations have been considered a good challenge to judge calibration process, so this design will be further examined.

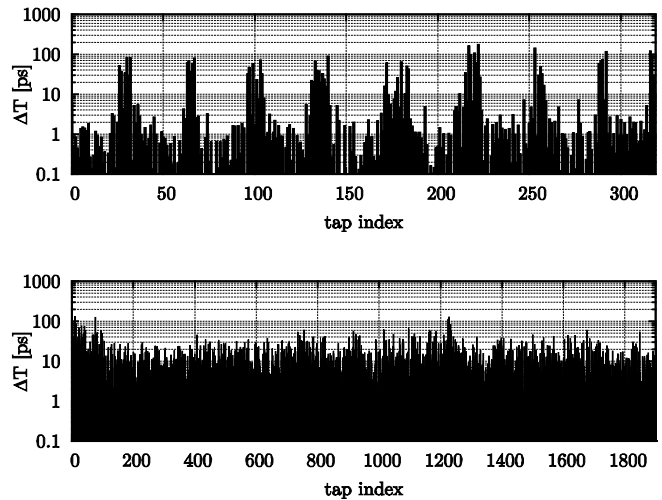


Fig. 4: Inter-tap delay histograms for two different TDC designs

The second design shows much smoother delay distribution. The worst-case of resolution is ± 63 ps. However, overall error of this design is 28 ps RMS. It should be noted, that RMS (root-mean-square) quantity is conclusive only under assumption, that pulse arrival is not correlated with reference clock (otherwise, the longest delay division may apply more frequently in worst case).

After calibration, the experiment with pulse generator has been performed. For each nominal pulse delay, preset on the pulse generator, a set of impulses has been recorded and again, a histogram calculated (called "preset histogram" in following text). Since bin numbers are already calibrated with respective t_n times, it is now possible to plot each preset histogram with respect to absolute time axis. Since the pulse edge delays have been chosen to $0 < t < T_{max}$, each preset histogram has been normalized to maximum height of 1. See Fig. 5.

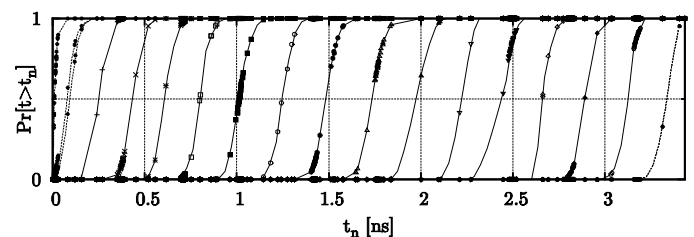


Fig. 5: Preset histograms approaching pulse delay CDF

Now, each preset histogram is an approximation of cumulative distribution function (CDF) of pulse arrival time, as measured by calibrated TDC. In ideal case of zero jitter over whole signal chain, the CDFs would be straight vertical $0 \rightarrow 1$ steps centered around measured time delay. The S-shaped slope of measured CDFs is caused by jitter

of frequency divider, pulse generator, I/O buffers and TDC flip-flops, including impact of all analogue noise sources.

The uneven spacing of "sampling points", i.e. histogram bins, is of no surprise, since it consists of peaks and valleys from Fig. 4.

To judge, whether obtained measurement is consistent with expectations, the mean time delay and variance should be determined for each preset histogram and compared with expected accuracy of signal chain. Whereas there is no prior estimate of other signal chain components, the DG535 pulse generator is specified to have mean variation up to 50 ps and jitter of 50 ps RMS.

Mean observed time delay should lie in center of the CDF curve. Variation then corresponds to its slope. Due to sparsity of data points, we have assumed normal model of probability distribution and fitted each CDF with an error-function. After rejection of five data sets suffering from delay line boundary conditions, the agreement in fitted standard deviation σ among all preset histograms was better than 10%. Therefore, following stochastic model has been adopted:

- all of the presets exhibit the same probability distribution, only displaced in time;
- the distribution is normal, with standard deviation σ .

For model to perform best in the time domain, we have fitted unknown means $t_{TDC\ 1} \cdot t_{TDC\ n}$ and standard deviation σ according to following criterion:

$$J = \sum_i \sum_j \left[\left(\sigma \sqrt{2} \operatorname{erf}^{-1}(2h_{i,j} - 1) + t_{TDC\ i} \right) - t_k \right]^2$$

with i, j spanning over calibrated, normalized histogram points (t_i, h_{ij}) (omitted where $|t_i - t_{TDC\ i}| > 2\sigma$). I.e. the CDFs were fitted minimizing squared distances between points and model curve in time. First, we have examined mean times τ_k against nominal preset times of signal generator t_{PG} . The result is plotted in left side of Fig. 6. Neglecting additive term, which is given by undefined clock to signal path delays, there is a strong linear trend visible in the plot. The trend slope is still large, compared to expected pulse generator accuracy and TDC's crystal oscillator frequency offset. Therefore, further investigation of this phenomenon is needed.

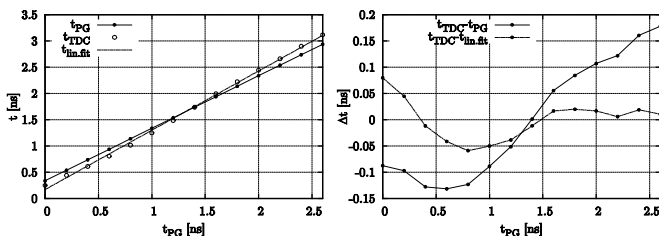


Fig. 6: Mean delay time variation TDC vs. pulse generator

The right part of Fig. 6 shows difference between nominal and fitted time; solid line is up to the constant term, dash-dotted line is with linear trend subtracted. After subtraction of linear term, the worst disagreement in mean pulse time is 80 ps.

Finally, the CDFs have been compared to the normal CDF model after subtraction of the mean values, see Fig. 7. Solid line represents ideal normal CDF with points of all preset histograms superimposed. Standard deviation of the model is $\sigma = 49$ ps RMS, what is within pulse

generator specification. The greatest difference between fitted model and preset histogram data point in time direction is 14 ps, overall agreement is 3 ps RMS.

Such a result supports our hope, that the normal jitter model is just, and that our TDC does not add significant amount of jitter compared to signal generator.

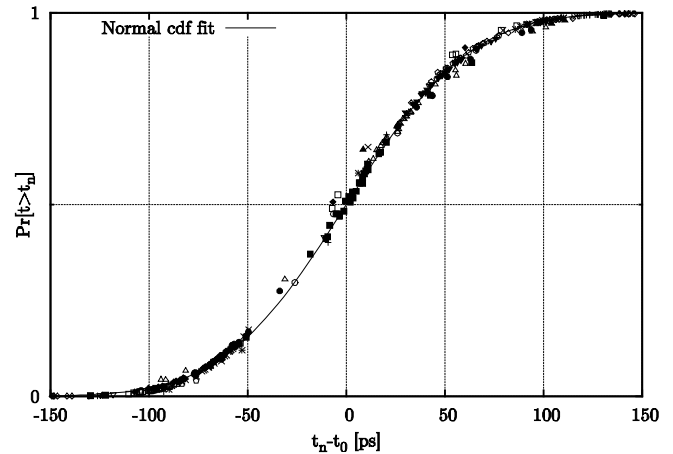


Fig. 7: Measured data fitted to normal distribution function

5. CONCLUSION AND OUTLOOK

Comparison between our random source calibrated TDC and laboratory pulse generator has shown agreement in mean up to 80 ps, up to a linear trend, whose source is to be investigated. The overall jitter observed is characterized to follow normal distribution with standard deviation of 49 ps, the probability model is fitted with accuracy of 3 ps RMS. The overall precision of one of our designs estimated from measured histogram is 28 ps RMS (for signals uncorrelated with reference clock) and 63 ps worst case.

Our future work should concentrate on following topics:

- finalize TDC to become usable measurement instrument ($T_{max} > T_0$);
- try to achieve faster clock (> 100 MHz) by FPGA design optimization;
- characterize flip-flop jitter and its impact on calibration;
- characterize temperature, radiation and aging stability;
- investigate possible impact of metastability phenomenon on flip-flop sampling.

References:

- [1] P. Panek, I. Prochazka. Time interval measurement device based on surface acoustic wave filter excitation, providing 1 ps precision and stability. IEEE Review of Scientific Instruments, Vol. 78 Issue 9, 2004
- [2] P. Panek. Time-Interval Measurement Based on SAW Filter Excitation. IEEE Transactions on Instrumentation and Measurement, 2008
- [3] Becker, Wolfgang. Advanced Time-Correlated Single Photon Counting Techniques : Springer-Verlag, 2005, ISBN 3-540-26047-1
- [4] Y. Zhang, P. Huang, R. Zhu. Upgrading of integration of time to digit converter on a single FPGA. Proc. 15th Int. Laser Ranging Workshop, Canberra Australia Oct. 2006
- [5] R. Salomon, R. Joost. BOUNCE: A New High-Resolution Time-Interval Measurement Architecture. IEEE Embedded Systems Letters, Vol. 1 Issue 2, Aug. 2009

The time-optimal control of a motion for a spacecraft with inertial executive devices

Mikhail Levskii, Research Institute of Space systems

The aspects of time-optimal control of spacecraft motion are discussed. Concrete problem of spacecraft's terminal reorientation is solved. The case when a change of spacecraft's angular position is done with use of inertial actuators (for example, control moment gyroscopes) is considered in this research. Therefore magnitude of spacecraft angular momentum is limited by some value which cannot be exceeded. The conditions of optimality is written, and the properties of optimal spatial turn are studied. Key relations and equations for optimal motion which specify the variation of rotation parameters are given. Results of mathematical simulation of spacecraft motion dynamics under the designed control method are presented.

1. INTRODUCTION

The problem of a transferring a spacecraft from an initial oriented position to a position with an assigned orientation in the optimal manner is solved. The designing of optimal control algorithms for onboard system of spacecraft attitude also remains very important now. For example, spacecrafts for Earth's remote sounding, monitoring, and also astrophysical and other scientific satellites demand periodic change of orientation for direction of scientific devices and the target equipment onto interesting sites of a terrestrial surface or area of heavenly sphere. Minimization of turn's duration will increase time of observation and will improve conditions of their execution. Optimization of a reorientation mode (in sense of maximum speed or minimum of spent resources) raises efficiency of spacecraft's use, and in some cases, it increases resource of spacecraft's functioning on the work orbit. In numerous cases, orientation control is carried out by inertial executive devices (in particular, moment gyroscopes or gyrodynes). This paper is devoted to finding the optimal program for the three-dimensional reorientation of a spacecraft in the minimum time taking into account the constraint imposed on the angular momentum. The solved problem is fairly important for a practice.

2. EQUATIONS OF MOTION AND STATEMENT OF THE PROBLEM

The equations of spacecraft's angular motion as a solid body look like:

$$J_1 \dot{\omega}_1 + (J_3 - J_2) \omega_2 \omega_3 = M_1, J_2 \dot{\omega}_2 + (J_1 - J_3) \omega_1 \omega_3 = M_2, J_3 \dot{\omega}_3 + (J_2 - J_1) \omega_1 \omega_2 = M_3$$

where J_j are the principal central moments of inertia of a spacecraft ($j=1, 2, 3$), M_j are the projections of the moment of external forces onto the principal central body axis, are the projections the absolute angular velocity vector ω onto the axes of the body-fixed basis \mathbf{E} formed by principal axes of spacecraft's ellipsoid of inertia.

For the description of spatial motion of a spacecraft around its center

of mass, the mathematical apparatus of quaternions is used [1]. We specify the motion of a body-fixed basis \mathbf{E} with respect to a reference basis \mathbf{I} by quaternion Λ . To be specific, we will assume that the basis \mathbf{I} is inertial. In this case, the kinematics of spacecraft motion is described by the following kinematic equations:

$$\begin{aligned} 2\dot{\lambda}_0 &= -\lambda_1 \omega_1 - \lambda_2 \omega_2 - \lambda_3 \omega_3, & 2\dot{\lambda}_1 &= \lambda_0 \omega_1 + \lambda_2 \omega_3 - \lambda_3 \omega_2 \\ 2\dot{\lambda}_2 &= \lambda_0 \omega_2 + \lambda_3 \omega_1 - \lambda_1 \omega_3, & 2\dot{\lambda}_3 &= \lambda_0 \omega_3 + \lambda_1 \omega_2 - \lambda_2 \omega_1 \end{aligned} \quad (1)$$

where λ_j are the components of quaternion Λ which is normalized $\|\Lambda\| = 1$ ($j = \overline{0,3}$). Angular position of initial and final orientations of the spacecraft concerning basic basis \mathbf{I} is defined by quaternions Λ_{st} and Λ_f accordingly (the quaternions Λ_{st} and Λ_f are normalized quaternions). Boundary conditions of spacecraft position and its angular velocity we shall set as:

$$\Lambda(0) = \Lambda_{st} \quad (2)$$

$$\Lambda(T) = \Lambda_f \quad (3)$$

and $\omega(0) = \omega_0$, $\omega(T) = \omega_T$, where T is time of a turn. The problems when boundary values $\omega_0 = \omega_T = 0$, and Λ_{st} , Λ_f have any arbitrary values is practically important.

In general case, the problem of reorientation consists in a moving the body-fixed coordinate system OXYZ from initial angular position $\Lambda_{st} = \Lambda(0)$ into required final position $\Lambda_f = \Lambda(T)$ at the time T in accordance with the differential equations (1). This problem earlier was researched [2]. For the spacecraft with inertial control facilities of orientation, the problem of spacecraft turn during minimal time is most important. In the latter case, the index of an optimality becomes:

$$G = \int_0^T dt \quad (4)$$

At control of spacecraft orientation using inertial actuators (for example, the control moment gyroscopes), the vector of the angular momentum should be in the given limited domain, the exit for which results in loss of spacecraft's controllability. We shall assume that the module of the

vector of a spacecraft's angular momentum cannot exceed some value H_0 , i.e. the condition should satisfy:

$$J_1^2 \omega_1^2 + J_2^2 \omega_2^2 + J_3^2 \omega_3^2 \leq H_0^2 \quad (5)$$

where $H_0 > 0$ is a specified positive value, must hold. The problem of optimal control we shall formulate as follows: it is necessary to transfer of a spacecraft from the state (2) into the state (3) according to the equations (1) at presence of restriction (5) and with minimal value of functional (4). The formulated problem is original.

When a constraint of the form (5) is imposed on spacecraft motion, the control problem stated is fairly important. The outcomes of its solution are useful for spacecraft equipped with gyroscopic mechanisms, i.e., gyrodynes. In this case, control of a spacecraft turn is achieved by re-distributing the angular momentum between the system of gyroscopes and spacecraft body [3]; the total angular momentum of the spacecraft as a rigid body with rotating masses is equal to or close to zero. The control of gyrodynes system in order to produce the programmed motion of a spacecraft by creating the necessary moments M_x, M_y, M_z is a separate, independent problem (this problem are not considered here). We merely note for an assigned turning regime to be realized without having to use other actuators (beside the gyrodynes), for example, jet engines, the total angular momentum of the gyro system must lie within the closed region S (it depends on the design characteristics), which determines the control possibilities of the gyro system, over the entire control interval $[0, T]$.

For algorithms of an attitude control of a spacecraft with control moment gyroscopes, it is assumed that the region S of admissible angular momentum values of the system of control moment gyroscopes is confined to a sphere. This assumption has been used by many researchers; it is valid for a large number (if not the majority) of spacecraft (such as the Mir orbital station, the Gamma astrophysical laboratory, the Alpha international space station and others). Since the use of control moment gyroscopes in a turning regime presumes that the total angular momentum of the gyro system would not exceed the admissible value, a constraint, which is formalized for the angular velocity vector, is imposed on the motion of the spacecraft. If the condition $\mathbf{L} + \mathbf{H} \approx 0$, where \mathbf{L} is the angular momentum of the spacecraft body, and \mathbf{H} is the angular momentum of the system of control moment gyroscopes, is taken into account, satisfaction of constraint (5) means that the evolution of the vector \mathbf{H} of the gyro system during the spacecraft motion will satisfy the condition that it lies within a region confined by a sphere; therefore, the turn occurs using only the control moment gyroscopes (the vector \mathbf{H} does not extend beyond this sphere region S without additional input to the action of the control thrusters). The general case of a spatial turn represents interest.

3. SOLUTION OF THE PROBLEM OF SPATIAL REORIENTATION

The formulated problem and synthesis of the optimal program of control must be solved using Pontryagin's principle of maximum [4]. For this purpose, we will enter the conjugate variables ψ_j ($j = \overline{0,3}$), corresponding to quaternion components λ_j . For criterion of an optimality (4), Pontryagin's function of the problem (Hamiltonian) Γ has the form: $\Gamma = -1 + \Gamma_k + \Gamma_d$, where Γ_k is the kinematical part, Γ_d does not depend from kinematic parameters λ_j .

$$\Gamma_k = -0.5\psi_0(\lambda_1\omega_1 + \lambda_2\omega_2 + \lambda_3\omega_3) + 0.5\psi_1(\lambda_0\omega_1 + \lambda_2\omega_3 - \lambda_3\omega_2) + 0.5\psi_2(\lambda_0\omega_2 + \lambda_3\omega_1 - \lambda_1\omega_3) + 0.5\psi_3(\lambda_0\omega_3 + \lambda_1\omega_2 - \lambda_2\omega_1)$$

The equations for conjugate functions ω_j look like: $\dot{\psi}_i = \partial \tilde{A} / \partial \lambda_j$, or (6)

$$\dot{\psi}_0 = -0.5(\psi_1\omega_1 + \psi_2\omega_2 + \psi_3\omega_3) \quad \dot{\psi}_1 = 0.5(\psi_0\omega_1 + \psi_2\omega_3 - \psi_3\omega_2) \\ \dot{\psi}_2 = 0.5(\psi_0\omega_2 + \psi_3\omega_1 - \psi_1\omega_3) \quad \dot{\psi}_3 = 0.5(\psi_0\omega_3 + \psi_1\omega_2 - \psi_2\omega_1)$$

After simple transformations of function Γ_k we will receive $\Gamma_k = 0.5(\omega_1(p_1 + \omega_2 p_2 + \omega_3 p_3))$, $p_1 = \lambda_0\psi_1 + \lambda_3\psi_2 - \lambda_1\psi_0 - \lambda_2\psi_3$; $p_2 = \lambda_0\psi_2 + \lambda_1\psi_3 - \lambda_2\psi_0 - \lambda_3\psi_1$; $p_3 = \lambda_0\psi_3 + \lambda_2\psi_1 - \lambda_3\psi_0 - \lambda_1\psi_2$

From the equations (6) follows that set of variables $\psi_0, \psi_1, \psi_2, \psi_3$ can be accepted as components of a certain quaternion Ψ for which the expression is fair: $2\Psi = \Psi \circ \boldsymbol{\omega}$. Then $\mathbf{p} = \text{vect}(\tilde{\Lambda} \circ \Psi)$, where p_i are the projections of vector \mathbf{p} onto the axis of the body-fixed basis \mathbf{E} ; and the kinematical part of function Γ becomes: $\Gamma_k = 0.5 \boldsymbol{\omega} \cdot \mathbf{p}$. Differentiating expressions for p_i ($i = \overline{1,3}$) and inserting in them the equations for λ_j and ψ_j ($j = \overline{0,3}$) we shall receive the necessary differential equations for the vector \mathbf{p} .

(7)

$$\dot{p}_1 = \omega_3 p_2 - \omega_2 p_3, \quad \dot{p}_2 = \omega_1 p_3 - \omega_3 p_1, \quad \dot{p}_3 = \omega_2 p_1 - \omega_1 p_2$$

By virtue of that $|\mathbf{p}| = \text{const}$, we assume further the vector \mathbf{p} is normalized: $|\mathbf{p}| = 1$. Equality takes place: $\mathbf{p} = \tilde{\Lambda} \circ \mathbf{c}_E = \circ \Lambda$, where $\mathbf{c}_E = \Lambda_{st} \circ \mathbf{p}(0) \circ \tilde{\Lambda}_{st} = \text{const}$ [1]. Boundary conditions Λ_{st}, Λ_t and conditions of a maximum of function Γ specify the required decision $\boldsymbol{\omega}(t)$. Controlled variables (controls) we shall count projections of angular velocity ω_j . Obviously, Γ_k is maximum under condition (5) when $p_j = kJ_j^2 \omega_j$ ($j = \overline{1,3}$). Optimal motion is completely determined by system of the differential equations:

$$\mathbf{p} = -\boldsymbol{\omega} \times \mathbf{p} \quad \text{and} \quad \omega_i = \frac{H_0 p_i}{J_i^2 \sqrt{p_1^2 / J_1^2 + p_2^2 / J_2^2 + p_3^2 / J_3^2}} \quad (8)$$

under support the boundary conditions (2), (3) for decision $\Lambda(t)$ of the system (1). The problem of constructing optimal control consists in a finding of such value of a vector $\mathbf{p}(0)$ that as a result of rotation according to the equations (1), (7), (8) the equality $\Lambda(T) = \Lambda_t$ was executed. Presence of restrictions on control moment \mathbf{M} does impossibly instant change of angular velocity $\boldsymbol{\omega}$ up to required value (the setting of calculated size in the beginning of a turn and damping of actual rate up to zero at the moment of arrival into the final position), that conducts to some increase of maneuver time T because of occurrence of acceleration stage and of braking stage. Maneuver of a turn will consist of spacecraft acceleration till the necessary angular momentum, rotation with a constant of angular momentum size H_0 and damping of angular rate. Required decision $\boldsymbol{\omega}(t)$ at the phase of nominal motion (between acceleration and a braking) possesses the properties:

$$J_1^2 \omega_1^2 + J_2^2 \omega_2^2 + J_3^2 \omega_3^2 = R = \text{const}, \quad \text{and} \quad J_1^4 \omega_1^2 + J_2^4 \omega_2^2 + J_3^4 \omega_3^2 = D = \text{const}.$$

The calculated value of control moment \mathbf{M} is determined as:

$$\mathbf{M} = \boldsymbol{\omega} \times (J \cdot \boldsymbol{\omega}) - J^{-1} \cdot (\boldsymbol{\omega} \times (J^2 \cdot \boldsymbol{\omega}))$$

where $J = \text{diag}(J_1, J_2, J_3)$ is the tensor of inertia.

Required program of spacecraft turn from initial Λ_{st} into the setting angular position Λ_t at time T is provided at the expense of maintenance of programmed angular velocity of spacecraft rotation with high accuracy using a principle of control on acceleration [5]. This systems possess increasing dynamic properties, and also accuracy, adaptability and robust property which are especially necessary at working off of calculated kinematics of rotation.

For spacecraft with axial symmetry ($J_2 = J_3$) a solution was found in an analytical form. Optimal motion is in a class of its simultaneous rotation as solid body around of longitudinal axis and around of some direction η , motionless in inertial space and making with longitudinal axis of a spacecraft the certain angle ϑ . For special case when $J_1 = J_2 = J_3$, the solution of the problem (1)–(5) corresponds to a turn of a spacecraft around the Euler axis.

4. RESULTS OF MATHEMATICAL SIMULATION

As an example, we give the numerical solution of problem of optimal control of spacecraft's programmed turn for minimal time T. Results of mathematical modeling of process of a turn under optimal control are submitted graphically.

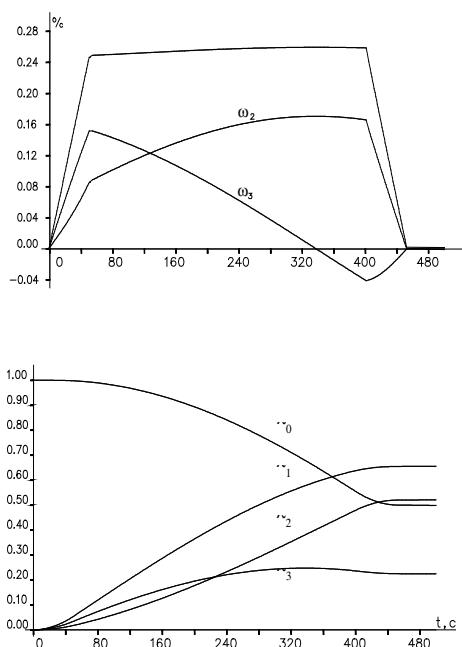


Fig. 1: Variation of the parameters of an attitude during optimal turn

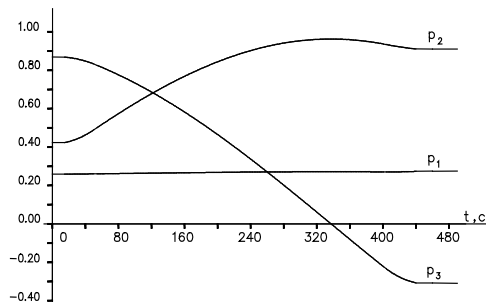


Fig. 2: The components of vector p as time functions

The variations of angular velocities in body-fixed coordinate system $\omega_i(t)$ presented in Fig.1. On him visible separation of full turn into three characteristic stages is distinctly seen: they are acceleration, rotation with as much as possible allowable angular momentum and braking. The variation of the components $\lambda_j(t)$ of quaternion $\Lambda(t)$ during executed maneuver, are displayed also. And, finally, Fig.3 illustrates the

dynamics of variation of the coordinates $p_i(t)$. A characteristic feature here is the insignificant variation of the projection p_1 (the component ω_1 also has almost constant value at the phase between acceleration and braking). This fact testifies that OX is the longitudinal axis of a spacecraft. The variables p_i and λ_j are smooth functions of time unlike the variables ω_i .

5. CONCLUSION

Here the problem of spacecraft's move from initial angular position to given angular position is solved [6]. The turn time is minimized. Interesting case, when a size (module) of spacecraft angular momentum is limited, is considered. Properties of optimal motion during a spatial turn are investigated. Often, the actuators of a spacecraft orientation system are control moment gyroscopes (CMGs). Their use in a turning regime requires that the total angular momentum H of the gyro system does not exceed the admissible value. In most cases, the region S of possible values of the total angular momentum of a system of CMGs, intended for attitude control of a spacecraft, is confined to a sphere of radius $H_{ad} > 0$. In order that a spacecraft turn should occur without the need for "unloading" the CMGs, satisfaction of the condition $|L| \leq H_0$ is required, where H_0 is an assigned constant, $0 < H_0 < H_{ad}$. The difference $H_{ad} - H_0$ guarantees an absence of the angular momentum of the CMG system outside the region S of possible values. Hence, a presence of constraint (5) and the applied sense of solution are understandable. Necessary conditions of optimality for a spacecraft reorientation regime have been written in analytical form. It is shown that the optimal solution belongs to a class of regular motions that are close to the precession of a rigid body around a certain axis fixed in inertial space. In the general case (a turn from a state of rest to a state of rest), a spacecraft reorientation manoeuvre is divided into three characteristic phases: acceleration to the maximum admissible angular momentum, rotation with the maximum magnitude of the angular momentum, and reduction of the angular velocity to zero. The offered algorithm of spacecraft's reorientation control under the limited size of the angular momentum allows considerably (from 20–30 % and more) to reduce a time of a turn. The synthesized algorithm for controlling spacecraft orientation enables us to apply this method in practice.

References:

- [1] Branets, V.N., and Shmygalevskii, I.P. Use of quaternions in problems of orientation of solid body. Moscow: Nauka, 1973.
- [2] Levskii, M.V. Optimal spacecraft terminal attitude control synthesis by the quaternion method. Mechanics of Solids, 2009, Volume 44, No. 2.
- [3] Raushenbakh, B.V., Tokar', E.N. Control of Spacecraft Attitude. Moscow: Nauka, 1974.
- [4] Boltjansky, V.G. Mathematical methods of optimal control. Moscow: Nauka, 1969.
- [5] Krut'ko, P.D. Inverse problems of the dynamics of control systems. Nonlinear models. Moscow: Nauka, 1988.
- [6] Levskii, M.V. A method of controlling the turn of a spacecraft. Russian Federation Patent No. 2093433. Bulletin "Inventions. Applications for Inventions and Patents", 1997, No. 29. Published 20 October, 1997.

Worst Case Analysis of an Accelerometer Measuring Loop

Jozef Zakucia

Worst case analysis belongs to the most important in the analysis section that is performed to document space product quality assurance. The WCA methods provide assurance that analysed system complies with requirements during its mission. The aim of the presented article is brief description and implementation of the most used worst case analysis methods such as Extreme Value Analysis, Root-Sum-Square Analysis and Monte Carlo Analysis. Presented methods are implemented in accelerometer measuring loop.

1. INTRODUCTION

The purpose of the WCA analysis in general is to serve as a tool for design centering, i.e. modifying of nominal system design to receive optimum system parameters [1]. Particular WCA target is providing an assurance by analysis that system design complies with requirements. The article describes WCA implementation for assessment of accelerometer measuring loop design. General principles of acceleration measuring with an electrostatic accelerometer system were described by Fontana in [4]. Basic information to the problems of tolerance analysis presents Géher in Chapter 4 of his monograph [2].

Three different methods of the tolerance effects analysis are generally named as:

- Extreme Value Analysis (EVA);
- Root-Sum-Square (RSS) Analysis;
- Monte Carlo Analysis (MCA).

The worst case analysis works with the circuit structure, tolerances of component characteristics, their temperature changes and time and radiation consequence changes. Grouping of tolerances from individual sources and detail tabular comparison of the three different WCA methods is presented in [5]. It is suitable for WCA to use a specialised methodology with computer program support. It combines processes of tolerance and sensitivity analyses to complete the task. The methods published by Robert R. Boyd in [3] are very useful for completing the task.

Acronyms and abbreviations

AKTRAD	One of the three identical electronic boards of accelerometer with sensor moving part position control as the main function
ECSS	European Cooperation for Space Standardization
EVA	Extreme Value Analysis
FMECA	Failure Modes Effects and Criticality Analysis
GNRHKS	Electronic board of accelerometer with precision amplitude sinusoidal generator and polarization voltage source (besides other functions)
MC	Monte Carlo (method)
MCA	Monte Carlo Analysis

POSDET	One of the three identical electronic boards of accelerometer with sensor moving part position detection as the main function
RSS	Root Sum Squared, (Root Sum of the Squares)
WCA	Worst Case Analysis

2. WCA METHODOLOGY

2.1 EVA procedure

Extreme Value Analysis is most common, easiest and conservative procedure to compute output tolerances of the analysed system. EVA involves the analysis of a given circuit/system under the worst case realizable limits for individual parts. Whether the maximum or minimum foreseeable value of a part parameter is used is dependent on the directional sensitivity of that parameter on overall circuit performance [17].

2.2 Root-Sum-Square (RSS) Analysis

For variations with random component, every variation consists from two parts. One of them presents bias with predictable direction, the other is the random component contribution [16]. Biased portions are summarized to resultant bias. Random components are processed in an RSS procedure and the result is added to resultant bias to receive the resultant output value variation. For detail description of such procedure see [5].

RSS definition: Variance (root sum squared, dispersion) of any function is described by the relation (see [3], Appendix: Derivation of the RSS Equation):

$$\text{Var}(Vo) = \sum_{i=1}^N \left(\frac{\partial Vo}{\partial X_i} \right)^2 \cdot \text{Var}(X_i) \quad (1)$$

or

$$\sigma^2(Vo) = \sum_{i=1}^N \left(\frac{\partial Vo}{\partial X_i} \right)^2 \cdot \sigma^2(X_i)$$

where:

X_i ... characteristic parameter of the i -th component,
 $\sigma^2 = \text{Var}(X_i)$... variance,
 σ ... standard deviation.

2.3 WCA – Monte Carlo Method

One of the most realistic estimation of the worst case performance is Monte Carlo analysis. Inputs for MCA are probabilistic distributions of the part values variability. And output of the MCA is probability distribution of circuit output values. The result of the MCA is commonly presented in the form of a histogram.

The commonly used probability distribution of the circuit components parameters are:

- Uniform distribution function (the most conservative for parameter variations).
- Gaussian distribution function (the most realistic for parameter variations).

3 EXAMPLE SOLUTION

Accelerometer measuring loop analysis:

MCA, RSS and EVA analysis were performed on measuring loop of the accelerometer. Simplified block scheme of the accelerometer feedback loop, created for the WCA purposes, is shown in Figure 1.

Input for the feedback system presented in the Figure 1 is acceleration Γ and output is voltage U_T . General formula for acceleration was derived in the form (meanings of the symbols are described below):

$$\Gamma = \frac{C_0 D}{m} \left[\frac{U_4^2}{(D+x)^2} - \frac{U_3^2}{(D-x)^2} \right] \quad (2)$$

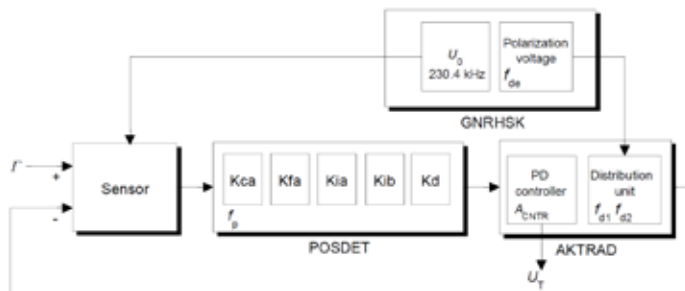


Fig. 1: Block scheme of accelerometer measuring loop

Γ	translation component of on board non-gravitational acceleration	[ms ⁻²]
x	equilibrium translation of cube position from the central position caused by constant non-gravitational acceleration	[m]
D	gap between electrodes when the sensor cube is placed in the central position; ($2 \cdot 10^{-4}$)	[m]
U_3	sensor electrode No. 3 control composite voltage $U_3 = f_{d1}(U_T, P_V, U_T, R)$	[V]
U_4	sensor electrode No. 4 control composite voltage $U_4 = f_{d2}(U_T, P_V, U_T, R)$	[V]
U_T	translation component of regulation voltage between the sensor electrodes $U_T(x) = x \cdot A_{CNTR} \cdot L_{PS}$	[V]
P_V	polarization voltage between the sensor electrodes; $(+11) P_V = f_{de}(U_{10})$	[V]
U_0	amplitude of sensing sinusoidal voltage with 230.4 kHz frequency; (1.0)	[V]
C_0	capacitance of an control electrode-cube electrode pair with cube placed in the central position; ($13.1 \cdot 10^{-12}$)	[F]

A_{CNTR}	AKTRAD amplifier's gain; (8)	[-]
L_{PS}	POSDET transfer from displacement to output voltage; $(10^5) L_{PS} = f_o(Kca, Kfa, \dots)$	[Vm ⁻¹]

Functions $f_{d1}, f_{d2}, f_{de}, f_p$ present simplified notations of the functional relations of their arguments. Detail insight into the system functions and equations is not introduced (it is comprised into computations) because of the limited length of this presentation. Above mentioned description of the system suffices for our considerations in this paper.

3.1 EVA

The procedure works with the simplified formula for acceleration value. Both sensor mass m and gap distance D are supposed to be constant, translation x , and consequently U_T voltage are taken as parameters and the EVA computation is performed for one of the parameter possible values ($x = 3.1 \cdot 10^{-6}$ m, $U_T = 2.48$ V). Individual independent variables are functions of circuit elements, mainly of pertinent POSDET and AKTRAD circuit boards elements. We will proceed EVA computations and receive in the end the following relative tolerances for the acceleration:

$$\left(\frac{\Delta \Gamma}{\Gamma} \right)_{EVA} = \begin{bmatrix} -5.16\% \\ +5.30\% \end{bmatrix} \quad (3)$$

3.2 RSS

For the next acceleration RSS tolerances evaluation:

We will use the results of particular RSS symmetric tolerances evaluations. The root of sum of quadratic terms is extracted from the data according to an RSS procedure:

$$\sum_{i=1}^n (Sen_i \cdot T_i)^2 = 3.14 \cdot 10^{-2} [\%]^2 + 3.72 \cdot 10^{-2} [\%]^2 + 8.57 \cdot 10^{-2} [\%]^2 + 2.37 [\%]^2 + 9.76 [\%]^2 = 12.444 [\%]^2 = 12.4 [\%]^2 \quad (4)$$

The result for relative tolerance value of Γ is:

$$\left(\frac{\Delta \Gamma}{\Gamma} \right)_{RSS} = \pm \left(\sqrt{\sum_i (Sen_i \cdot T_i)^2} \right) = \pm 3.53\% \quad (5)$$

3.3 MCA

MCA was performed on measuring loop of the accelerometer. Simplified block scheme of the accelerometer feedback loop, created for the WCA purposes, is shown in Figure 1. MCA considers the tolerances of substantial resistors in the signal measuring path and particular POSDET units.

Input for this feedback system, presented in the Figure 1 is acceleration Γ and output is voltage U_T . The aim of this analysis is to compute tolerances of the acceleration Γ . Mentioned system is described by the function

$$\Gamma = f(U_T(x)) \quad (6)$$

where

$$U_T(x) = x \cdot A_{CNTR} \cdot L_{PS} \quad (7)$$

corresponding with (2) where x (parameter) is the position of the sensor cube (see Table 1 for other details). The computation was realized by running MATLAB script. Inputs for the script were array of the accelerometer part tolerances and function of the system stated in clause 3.

The result of this computation (for parameter x set to e.g. $3.1 \mu\text{m}$) is histogram of the acceleration Γ shown in Figure 2. The 2σ value of the final acceleration distribution stands for 4.24% tolerance of the acceleration value.

$$2\sigma_{MCA} = 4.24\% \quad (8)$$

A histogram of the acceleration Γ was created (Figure 3) and computed for each value x from a set of the parameter (in its working range).

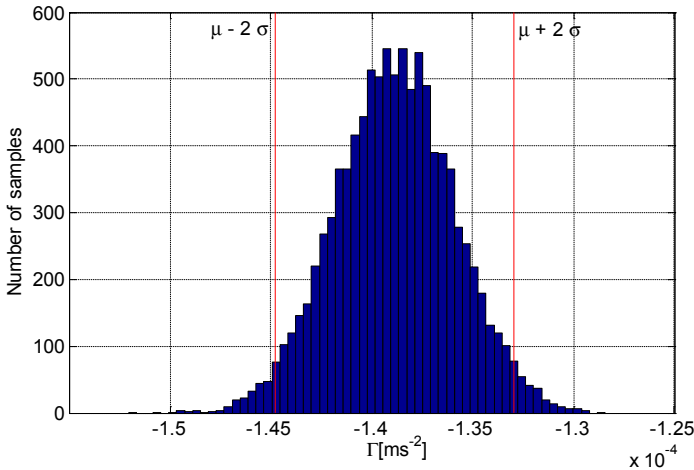


Fig. 2: Histogram of acceleration PDF in 2D

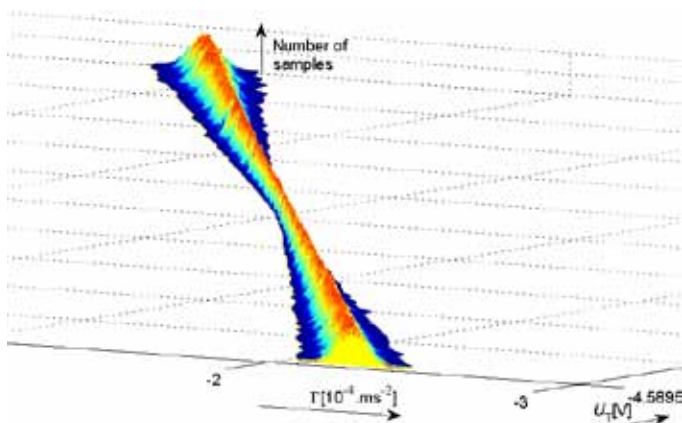


Fig. 3: Three-dimensional view of acceleration PDF histograms for variable U_T value

4. CONCLUSIONS

Comparison of used WCA methods illustrates, that EVA/RSS methods present data with great effort even in the case of using dedicated software. MCA method encodes graphical outputs as a bonus for better presentation of the results.

For presented example of accelerometer measuring feedback loop the resulting tolerance values for the three used methods are:

EVA {-5.16 %, +5.30 %}; RSS {-3.53 %, +3.53 %}; MCA {-4.24 %, +4.24 %}.

Regardless of the results differences, all the methods give well corresponding results and their parallel using supports assurance of the results correctness.

References:

- [1] Novák, M.: Theory of Network Tolerances. Academia Praha 1987, (published in Czech: Teorie Tolerance soustav) 340 pp.
- [2] Géher, K., Theory of Network Tolerances. Akadémiai Kiadó, Budapest 1971, 184 pp.
- [3] Boyd, R.R.: Tolerance analysis of electronic circuits using MATLAB. CRC Press, 1999, 147 pp.
- [4] Fontana, G.: High Performance Electrostatic Sensors and Actuators for LISA Proof Mass Control. University of Trento, 2002, 57 pp., <http://arxiv4.library.cornell.edu/ftp/physics/papers/0111/0111006.pdf>
- [5] Worst Case Circuit Analysis (WCCA). System Reliability Center, <http://src.alionscience.com/pdf/WorstCaseCircuitAnalysis.pdf>, 2004 Alion Science and Technology.
- [6] MIL-STD-785 Reliability program for systems and equipment development and production
- [7] ECSS-Q-30-01A, First issue, Worst case circuit performance analysis. 31. March 2005, Discontinued Requirements transferred to ECSS-Q-ST-30C, remaining material to ECSS-Q-HB-30-01A
- [8] ECSS-Q-ST-30C Space product assurance – Dependability. 6 March 2009, 54 pp.
- [9] ECSS-Q-HB-30-01A (working draft)
- [10] ECSS-Q-TM-30-12C (working draft)
- [11] ECSS-E-ST-10-04C Space Engineering – Space Environment. 15 November 2008, 198 pp.
- [12] ECSS-E-ST-10-12C (15 November 2008) Space Engineering – Methods for the calculation of radiation received and its effects, and a policy for design margins
- [13] ECSS-Q-60-11A (7 September 2004) Space product assurance – Derating and end-of-life parameter drifts – EEE components
- [14] ECSS-Q-ST-30-11C Space product assurance – Derating – EEE components. 31 July 2008, 59 pp.
- [15] MIL-HDBK-1547A (06 July 1998): DoD Handbook – Electronic Parts, Materials, and Processes for Space and Launch Vehicles; 253 pp.
- [16] JPL D-5703, Reliability Analyses Handbook. NASA JPL, Jul 1990, 169 pp.
- [17] Worst Case Circuit Analysis Application Guidelines, Reliability Analysis Center, 1993; 98 pp.

Space Solar Patrol data and the global changes

S.V. Avakyan¹, L.A. Baranova², E.V. Kuvaldin¹, N.B. Leonov¹,

A.V. Savuyshkin¹, N.A. Voronin¹, V.V. Kovalenok³, V.P. Savinykh⁴,

¹All-Russian Science Center "S.I. Vavilov State Optical Institute", Birgevaya linia, 12,

²A.F. Ioffe Physico-Technical Institute of RAS, Saint-Petersburg, Russian Federation

³Federation of Cosmonautics of Russia

⁴Moscow State University of Geodesy and Cartography

The results obtained during the execution of several ISTC projects are presented. The general aim of these ISTC projects has been the study of global changes, connected with solar activity. Brief description is given of the optical apparatus of the Space Solar Patrol (SSP) developed and built in the framework of the ISTC projects # 385, 385.2, 1523 and 2500. The Space Solar Patrol has been intended for permanent monitoring of spectra and absolute fluxes of soft X-ray and extreme ultraviolet (X-ray/EUV) radiation from full disc of Sun which ionize the upper atmosphere of Earth. The permanent solar monitoring at the main part of the ionizing radiation spectra 0.8-115 (119) nm does not exist. An important point is the degree of solar blindness of the ionizing-radiation detectors. It is highest in the SSP apparatus (up to 10–10 of the working section of the spectrum even at 270 nm). The study of the physical causes of the influence of the main factors of space on the state of the ionosphere and then to the weather and climate characteristics, including global warming is presented. The basis of this research - proposed by the authors Rydberg excitation-by the fast ionospheric electrons experimentally observed microwave radiation the Earth's ionosphere, which is almost free to penetrate into the lower atmosphere, providing channels of influence of solar variability on terrestrial phenomena.

1. INTRODUCTION

In recent years there has been a sharp increase in the interest in and need for monitoring of the solar activity and its effects in phenomena on Earth. But one of the gaps of the modern solar-terrestrial physics is an absence of the permanent space monitoring of the soft X-ray and extreme ultraviolet radiation from the full disk of Sun. The solar activity determines the degree of geomagnetic activity. The strongest manifestations of solar activity are solar flares [1] and they are often responsible for the most important manifestations of the solar activity on the Earth, i.e. geomagnetic storms. Therefore the first cause of numerous phenomena in the solar-terrestrial relations is a solar flare and the flare events on the Sun.

The monitoring of the most important solar irradiance in the spectral range of 0,8 - 119 nm does not exist at present. Presently at the satellite TIMED the Solar EUV Experiment (SEE) observations are limited to about 4 min per orbit, with an orbital period being about 97 min. As can be seen from its low duty cycle for the solar observations, "SEE was not designed to study flares" [2]. The current measurements (see Table 1) carried out only several times per day or/and only at the limited spectral ranges. It should be emphasized that, to present day, there is no monitoring of variations of absolute magnitude of the fluxes of solar ionizing radiation and their

spectral composition. There are no experimental data on the spectra and increments of the fluxes in the periods of flares on the sun of various levels and classes. Table 1 shows the results of our analysis of the completed and planned space experiments on monitoring the solar short-wavelength activity in the period from 1996 to 2012. It can be seen that the only experiment that solves the tasks of total monitoring of solar short-wavelength activity (including measurements over the whole spectral interval with the required for solar-terrestrial physics spectral resolution of about 1 nm, and in constant duty with continuous spectrum scanning each 72 s, which is close to both the subflare duration and the pulse phase of high-power flares) is the Permanent Space Solar Patrol proposed by us.

The results of this spectral monitoring may be a source of development of studies in several sciences such as: solar physics (the state of all regions of the solar atmosphere), meteorology and physics of the atmosphere (impact of shortwave solar activity on the global changes, weather and climate including the effects of atmospheric electricity), aeronomy, cosmonautics (influence of solar activity on the density of the upper atmosphere and the drag of space vehicles, on the parameters of their atmosphere and satellite anomalies), radiophysics (determination and prediction of the planetary ionospheres and conditions of radio wave propagation), heliobiology (the possible role of the solar variability in biology and medicine), technosphere (including pipeline), possibly seismology and probably sociology.

Spacecraft, country	Apparatus, spectral region ($\Delta\lambda$) and resolution ($\delta\lambda$)	Comments
SOHO (Solar and Heliospheric Observatory), international	SEM (Solar EUV Monitor), $\Delta\lambda = 26\text{-}34$ nm and $\Delta\lambda = 0.1\text{+}50$ nm, $\delta\lambda$ - only 2 specified spectral channels. SUMER (Solar Ultraviolet Measurements of Emitted Radiation), $\Delta\lambda = 46.5\text{-}80$ nm, $66\text{+}161$ nm, $\delta\lambda = 0.004$ nm in both channels.	Measurements every 15 s with limitation on resolution and without overlapping the entire range. The solar disk is entirely scanned only during several hours, but these measurements, as a rule, are not carried out.
SNOE (Student Nitric Oxide Explorer), USA	SXP (Solar XUV Photometer), $\Delta\lambda = 3\text{+}20$ nm, $\delta\lambda$ - three spectral intervals in total.	Measurements four times a day with limitations on the resolution and range.
GOES (Geostationary Operational Environmental Satellites), USA	XRS (Solar X-ray Sensor), $\Delta\lambda = 0.05\text{+}0.8$ nm, $\delta\lambda$ - two spectral intervals in total.	Continuous measurements in a narrow region of the solar spectrum.
KORONAS-I and -F (Comprehensive orbital near-earth observations of the activity of the Sun), Russia, Poland	SUVR (Solar UV Radiometer) and VUSS (UV solar spectrometer), $\Delta\lambda < 130$ nm, ~ 120 nm, < 12 nm, $\delta\lambda$ - three intervals in total.	One measurement in 7 minutes without resolution required for geophysical tasks.
TIMED (Thermosphere-Ionosphere – Mesosphere-Energetics-Dynamics), USA	SEE (Solar EUV Experiment): XPS (XUV Photometer System), $\Delta\lambda = 0.1\text{+}27$ nm, $\delta\lambda$ - twelve spectral intervals in total; EGS (EUV Grazing Spectrograph), $\Delta\lambda = 26\text{+}195$ nm, $\delta\lambda = 0.4$ nm in this spectral interval.	Measurements are carried out in less than 4 minutes per turn (97 minutes) with a complete range covering.
SORCE (Solar Radiation and Climatic Experiment), USA	XPS (XUV Photometer System), $\Delta\lambda = 1\text{+}34$ nm, $\delta\lambda$ - ten spectral intervals in total; $\lambda = 121.6$ nm, $\Delta\lambda = 115\text{+}195$ nm, $\delta\lambda = 1$ nm in this spectral interval.	Measurements take up to 60% of the time in the turn, but without covering the main part of the range.
MKS (International Space Station), Germany	SOL-ACES (Solar Auto Calibrating EUV/UV Spectrometers), $\Delta\lambda = 17\text{+}220$ nm, $\delta\lambda = 0.5\text{+}2$ nm in this spectral interval.	Measurements take up to 15 min on the turn, 600 hours/year.
GOES, USA	Five broad spectral bands in the extreme UV range (EUV-Sensor).	2009
Solar-B, Japan, USA, Great Britain	XRT (X-Ray Telescope) (an improved counterpart of the SXT (Soft X-Ray Telescope) on Solar-A (Yohkoh)), $\Delta\lambda = 0.2\text{+}6.0$ nm, the spectrum for a time less than 10 s.	2008, there is not the EUV data!
GOES-O (Geostationary Operational Environmental Satellites), USA	EUV-Sensor $\Delta\lambda = 5\text{-}15$ nm, $\Delta\lambda = 25\text{-}34$ nm, $\delta\lambda = 118\text{-}127$ nm	There are not spectral resolution, 2009
KORONAS-Foton, Russia and Germany	"EUV-Foka", $\Delta\lambda = 10\text{+}130$ nm, $\delta\lambda$ - six spectral intervals in total.	2009, but already there not measurements
Proba-2, ESA, Belgium, Switzerland, Germany	"Lyra", $\Delta\lambda 115\text{-}125$ nm, $\Delta\lambda 200\text{+}220$ nm, $\Delta\lambda = 17\text{+}31$ nm, $\Delta\lambda = 1\text{+}20$ nm (four indicated spectral channels in total).	The first data are given in 2011, one measurements 50 millisecond

SDO (Solar Dynamics Observatory), USA	"EUV Variability Experiment" MEGS: $\Delta\lambda = 5\text{+}37$ nm, $\Delta\lambda = 35\text{+}105$ nm, $\Delta\lambda = 0.1\text{+}7$ nm, $\lambda = 121.6$ nm, $\delta\lambda = 0.1$ nm; EPS: $\Delta\lambda = 34\text{-}38.1$ nm, $\Delta\lambda = 23.1\text{-}27.6$ nm, $\Delta\lambda = 17.2\text{-}20.6$ nm, $\Delta\lambda = 28.0\text{-}31.6$ nm	Temporal resolution is 0.25 sec and 10 sec, 2010
Spaceship will be defined in accordance with the Federal Space Program of the Russian Federation	Permanent Space Solar Patrol: Radiometer $\Delta\lambda = 0.14\text{+}157$ nm, $\delta\lambda$ - twenty spectral intervals, XUV (X-ray-EUV)- spectrometer, $\Delta\lambda = 1.8\text{+}198$ nm, $\delta\lambda$ is about 1 nm. EUV-spectrometer, $\Delta\lambda = 17\text{+}155$ nm, $\delta\lambda$ is about 0.2 nm	Permanent continuous-mode absolute measurements of full spectra every 72 s.

Tab. 1. Space experiments on monitoring short-wavelength solar activity.

The results of this spectral monitoring may be a source of development of studies in several sciences such as: solar physics (the state of all regions of the solar atmosphere), meteorology and physics of the atmosphere (impact of shortwave solar activity on the global changes, weather and climate including the effects of atmospheric electricity), aeronomy, cosmonautics (influence of solar activity on the density of the upper atmosphere and the drag of space vehicles, on the parameters of their atmosphere and satellite anomalies), radiophysics (determination and prediction of the planetary ionospheres and conditions of radio wave propagation), heliobiology (the possible role of the solar variability in biology and medicine), technosphere (including pipeline), possibly seismology and probably sociology.

2. SPACE SOLAR PATROL METHODOLOGY AND

The technique of the Space Solar Patrol absolute measurements involve the simultaneous use of two spectrometers and a radiometer, and a special algorithm is used for separating signals from radiation and charged particles precipitating from the earth radiation belts. In this case, the spectrometers measure a detailed source function and its variations, whereas the filter sensors give reference information for selecting signals of the solar radiation and for obtaining its absolute intensity allowing for the stray light in the spectrometer (with due account of the source function and the presence of 20 wave bands isolated by foil, thin-film, and crystal filters). The signals of the radiation and charged particles are isolated by comparing the readings from a solar sensor with those of another one mounted at a close pitch angle, which detects the charged particles. Finally all spectrometers and radiometer use the same open secondary electron multipliers (elaborated by the State Optical Institute) with BeO photocathode, which is "solar-blind" and characterized by high sensitivity in the EUV and soft X-ray region. This effect allows to use the submicron film filters of carbon, boron, Lexan, which characterized by the high value of transmittance in visual region. The multiplier has a large dynamic scope up to 10^7 . The latter characteristic enables to carry out the measurements both for quiet Sun and during the very large solar flares.

The apparatus of the permanent solar patrol system for monitoring the solar radiation comprises the following units [3]:

1. A space-based patrol radiometer for the 0.14-157-nm spectral range with sequential separation of 20 bands of different spectral widths using a disk with filters made from thin metal foils, thin films, and optical crystals.
2. A space-based patrol spectrometer for the extreme UV radiation, which measures the solar radiation spectrum in a spectral range from 17 to 155 nm with a spectral resolution of 0.2 nm.
3. The new design of scanning slitless grazing polychromatic X/EUV-spectrometer is proposed [4]. It allows the registration of the spectral distribution of the solar irradiance in the spectral range of 1.8 nm - 198 nm to be carried out during 72 s with a spectral resolution about 1 nm. The concave grating with 600 grooves per mm and with radius $R=28080$ mm, size $S=30 \times 20$ mm², blaze angle $\delta=1^\circ$ ($\lambda\delta=3$ nm) is used. The variable line space enables the focal curve to be placed as close to the exit slits as possible. The spectrum scanning is performed by means of turning the exit slit together with the detector of radiation. In this case the entrance window and the grating are not moved. The grazing angle is 2 degrees.

3. ROLE OF THE SPACE SOLAR PATROL DATA IN INVESTIGATION OF GLOBAL CHANGES

The most important problem of the current science is to understand the basis causes of global environmental changes. Global warming observed in recent decades could present a potential danger for mankind.

According to [5] during the several past decades all the trends in the Sun that could have had an influence on the Earth's climate have been in the opposite direction to that required to explain the observed rise in global mean temperatures and therefore the observed rapid rise in global mean temperatures seen after 1985 cannot be ascribed to solar variability. Indeed, since 1985 the total solar irradiance (TSI) and extreme ultraviolet and soft x-ray radiation (EUV/X-ray) ionizing fluxes have been decreasing. Similar behaviour of TSI and EUV/X-ray fluxes [6] reflects the effect of secular cycles of solar activity. However geomagnetic activity (aa-index) has been going up till 2003 (+ 0.3 % per year after 1985). Similar growth was observed since the beginning of XX century, by a factor of 2 according to [7]. Only during the last few years geomagnetic activity also started decreasing (- 10.7 % per year). This means that negative trends after 2003 have come both for solar electromagnetic (including X/EUV) and geomagnetic activities. According to the suggested radiooptical trigger mechanism [8, 9] just ionospheric microwave radiation of aurora during the periods of geomagnetic storms affects the global climate changes. The fall of both solar EUV fluxes and geomagnetic activity during recent years the rate of the natural global warming will go down in the nearest future to the lower levels [8, 9]. Cosmic rays is the principal source of ionization of the stratosphere and troposphere and can slightly modulate the formation of lower level of the optically thick clouds, which produce mainly cooling effect in day-time. The long-term decline in GCR has been experimentally observed during several decades. But after 1996 there is an increase both in last minimum of GCR (near 2000) and in maximum of the current eleven solar cycle.

4. CONCLUSIONS

At present all three devices of Space Solar Patrol apparatus: radiometer, EUV-spectrometer and X/EUV-spectrometer are created and have been successfully tested in laboratory vacuum chambers SOI and (radiome-

ter) ESTEC. The data of this monitoring very important for study of global change in environment, because a novel radiooptical trigger mechanism is proposed for solar-weather relations [8, 9]. According to this mechanism, both solar EUV/X-ray radiation and corpuscular radiations during solar and geomagnetic events excite the Rydberg states of upper atmosphere neutral constituents by the impact of ionospheric electrons. At the laboratory experiments the excitation of these states by electron impact firstly was registered in [10]. The emission from these states is in the microwave range and penetrates freely from ionospheric heights to the lower atmosphere. There, via a complicated chain of processes involving creation and destruction of water clusters, this emission influences the water vapour content and cloudiness, both being a substantial parts of weather formation. As a result the role of radiooptical trigger mechanism in formation of clouds and aerosol layers is weakening that has to result in decrease of optical thin clouds which cause a net warming. Thus it is shown in the present paper that during last years all the main factors of solar variability influence on the weather and climate changed sign of trends in the direction that leads to the decrease of global mean surface air temperature [8, 9].

References:

- [1] Svestka Z.: Solar flares. D. Reidel Co., 399 p. 1976.
- [2] Woods, T.N., Rottman, G.J.: Solar Ultraviolet Variability Over Time Periods of Aeronomic Interest - "Atmospheres in the Solar System: Comparative Aeronomy", Geophysical Monograph 130, 151-167, 2002.
- [3] S.V. Avakyan, Andreev E.P., Afanas'ev I.M., Leonov N.B., Savushkin A.V., Serova A.E., Voronin N.A.: Creating of the permanent Space Patrol of ionizing solar radiation - "Innovative Telescopes and Instrumentation for Solar Astrophysics", Hawaii, Eds. S.L. Keil, S.V. Avakyan, Proc. SPIE, v. 4853, pp. 600-611, 2002.
- [4] Avakyan S.V.: Space Solar Patrol Absolute Measurements of Ionizing Solar Radiation - 35-th Scientific Assembly of COSPAR, Paris, France 18-25 July 2004, Advances in Space Research, V. 37, Issue 2, pp. 297-302, 2006.
- [5] Lockwood M., Frohlich C.: Recent oppositely directed trends in solar climate forcings and the global mean surface air temperature - Proceedings of Royal Society A. doi:10.1098/rspa.2007.1880, 14 p., 2007.
- [6] Lean J.: Living with a variable Sun - Physics Today, pp. 32-38, June, 2005.
- [7] Benestad R.E., and Schmidt G.A.: Solar trends and global warming - J. Geophys. Res., 114, D14101, doi:10.1029/2008JD011639. 2009.
- [8] Avakyan S.V., Voronin, N.A.: On the radiooptical and optical mechanisms of influence of cosmic factors on the global warming - Journal of Optical technology, 77 (2), pp. 141-144, 2010.
- [9] Avakyan S.V., Voronin N.A.: The role of space and ionospheric disturbances in the global climate change and pipeline corrosion - Issledovanie Zemli iz kosmosa, 3, pp. 14-29, 2011.
- [10] Cermak, V., Herman, Z.: The mass spectrometric detection of highly excited long-lived states of noble gas atoms - Collection Czech. Chem. Commun. 29, 4, pp. 953-959. 1964.

Solution of the problem of recognition celestial sky in astronavigation.

A. P. Grigoryev , V. Y. Mamaev

State University of Aerospace Instrumentation, Saint-Petersburg, Russia

The article deals with the possibility of using artificial neural networks (ANN) to solve the problem of recognition celestial sky in astronavigation. Expected results - increased noise immunity of the system due to the invariance of the ANN to distortions of input images of the stars. Substantiates the choice of network architecture and its method of training. Analyzed and discussed options for improving the speed and accuracy of recognition network.

INTRODUCTION

The sensors used in the orientation of stellar systems, satellite control (SC) from the first steps of space exploration. In addition to the stars as reference guidelines for solving problems related to orientation and navigation of aircraft can perform and other celestial objects like the Sun or Earth. There are special devices which allow to determine the orientation of the spacecraft based on survey data of celestial bodies - the stellar orientation sensors. Star coordinators are opto-electronic devices, allowing to determine the parameters of orientation on the results of processing of images of the celestial sphere. The principle of such devices is the reception of electromagnetic energy in the visible spectrum with its subsequent conversion and processing to obtain information about the position of the axis of the instrument. On the degree of automation star appliances can be a manual or automatic device (sextants).

There are devices that allow to determine the orientation of the spacecraft by the sight of single stars, as well as devices that work with the field stars. When using the device of the first type in the control space vehicle must be at least two star unit. The principle of operation of such devices is based on tracking and automatic selected astroorientation combined direction of the optical axis with the direction this astroorientation. Currently, preference is given to devices that are in the process of their work record images of stars, and by further processing of the image, determine the position of the spacecraft in the base coordinate system. The base coordinate system is generally considered second equatorial coordinate system or an orbital system of coordinates.

The main objective of the star device working with an image of the field stars, is to define the axes of the internal system of coordinates in a coordinate system connected with the stars. However appliances of this type possess certain disadvantages, which include, above all, their low immunity. Interfering factors can be divided into two groups - the factors of space (mainly charged particles and gas-dust medium) and parameters of the spacecraft on which the device (in the first place, the angular velocity). Increased radiation resistance and immunity to interference Star appliances may only after a large number of scientific

research, engineering and production work. The article deals with the possibility of using artificial neural networks (ANN) to solve the problem of recognition of star chart. Expected results - increased noise immunity of the system due to the invariance of the ANN to distortions of input images of the stars.

At present, most often in pattern recognition and image identification using classical neural network architectures (multilayer perceptron, feedforward networks, recurrent, radial basis, etc.), but, in practice, the use of classical ANN topologies to this problem is inefficient for the following reasons:

First, as a rule, images are of large dimension, respectively, grow the size of a neural network (number of neurons, the number of layers, synaptic connections and other). For example, an image of $28 * 28$ to 784 input ANN. If we take into account that in itself transform the image on the display of class rather complex and essentially nonlinear, it is necessary to use a multi-layer network. Since the number of neurons in the hidden layer must be at least an order of magnitude greater than the number of network inputs, the hidden layer should be about 8,000 neurons. Thus the number of trainees and customizable links will be about 5 million more than the number of parameters requires a larger training set, which increases the time and the computational complexity of the learning process.

Second, the lack of a full mesh architecture is that the topology of the input is ignored. Input parameters can be presented in any order, while images have a strict structure: the variables (pixels) that are spatially adjacent, highly dependent to each other.

Of these shortcomings are free to so-called Convolutional neural networks (SNA), as proposed by the American scientist Ian LeKunom. They provide partial resistance to changes of scale, mixing, rotation, change of perspective and other distortions of the image. The idea of convolutional neural networks lies in the alternating layers of convolution (C-layers), subdiskretiziruyuschih layers (S-layers) and the presence of fully connected (F-layers) layers at the exit. Convolution neural network topology is shown in (Fig. 1).

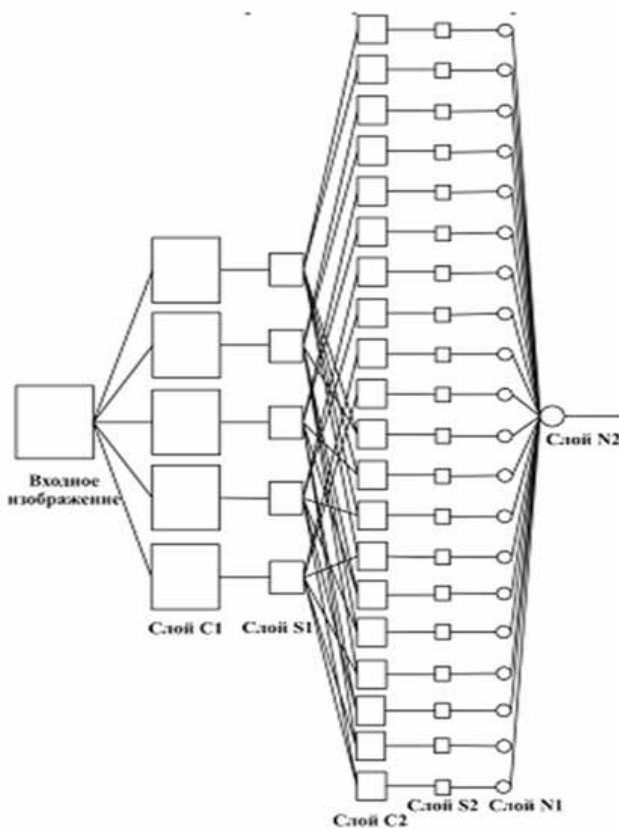


Fig. 1. The structure of the convolutional neural network

The architecture comprises three major paradigms:

1. Local perception (provided by a local two-dimensional connectivity of neurons);
2. Partial weight (provided by the detection of certain features anywhere in the image and reduces the total number of weights);
3. Undersampling (hierarchical organization).
4. Local perception implies that the input of one neuron is fed not the whole picture (or the output of the previous layer), but only some of its area. Such an approach to preserve the topology of the image from layer to layer.

The concept of shared weights suggests that for a large number of connections used is very small set of weights. For example the input image size of the SNA $32 * 32$ pixels, each of the next layer of neurons takes in input only a small portion of the image size, for example, $5 * 5$, and each of the fragments will be processed by the same set. It should be noted that sets of weights themselves can be quite a lot (in the training set), but each of them will be applied to the entire image. These sets are called kernels (kernels).

You can consider this approach from the other side. Most systems for pattern recognition are based on two-dimensional filters. A filter is a matrix of coefficients, usually given manually. This matrix is applied to the image using a mathematical operation called convolution. The essence of this operation is that each portion of the image is multiplied by the matrix (core) element-wise convolution and the result is summed and recorded in a similar position of output image. The main property of these filters is that the value of their output by more than a fragment more similar to the filter itself. Thus an image with some rolled-core will

give us a different image, each pixel would mean the similarity of an image to the filter. In other words, it will map features. Each fragment elementwise multiplied by a small matrix of weights (core), the result is summed up. This amount is the output image pixel, which is called the card features a weighted sum of the inputs is passed through the activation function (as in any other network). It should be noted that there are different parts successively through the core, and parallel to the image passes through all the identical nucleus. In addition, the number of cores (sets of weights) is determined by the developer and depends on a number of features to select. Another feature of the convolutional layer that it slightly reduces the image by edge effects.

The essence of undersampling and S-layer is to reduce the spatial dimension of the image. I.e input image is grossly (average) decreases in a specified number of times. More often than 2 times, although it may not even change, for example, two vertical and three horizontal. Sub-sampling is needed to ensure invariance to scale. Alternating layers allows to map features of the cards features, which in practice means the ability to recognize complex hierarchies of attributes.

Usually, after the passage of several layers of map features degenerates into a vector or a scalar, but these cards is hundreds of signs. As such, they are served by one or two layers of mesh networks. The output layer of the network may have different activation functions.

Used a neural network (NN) consists of six layers. The inputs to the neural network are the image (as an example, select an image size of $36 * 32$ pixels) that are classified as "presence of an object" or "The lack of an object." Since the problem is solved by the National Assembly - the classification, it is enough to resolve it one way out. The output value of the network is in the range $[-1, 1]$, respectively, that means the absence or presence of an object on the classified image.

As an activation function is used hyperbolic tangent. This is for the following reasons: symmetric activation functions such as hyperbolic tangent, provide faster convergence than the standard logistic function, this function has a simple and continuous first derivative that allows its use for training the algorithm with back propagation.

To train the neural network is selected as described algorithm error back propagation (back propagation). Education network begins with the presentation of the image and calculate the corresponding reaction. Comparison with the desired reaction makes it possible to change the weights of links so that the network in the next step could give a more accurate result. Training usually provides a setting the weights. Information about the network output is the starting point for the previous layers of neurons. These neurons can adjust the weight of their connections to reduce the error in the next step. When an unconfigured network is presented an input image, it will return a random way. The error function is the difference between the current output of the network and the ideal output, which must be obtained. For successful training, the network needed to bring the output of the network to the desired output, i.e, consistently reduced the magnitude of the error function. This is achieved by setting interneuronal connections. Each neuron in the network has its own weight, which is configured to reduce the magnitude of the error function.

The algorithm is error back-propagation method for quickly calculating the vector of partial derivatives (gradient) of a complex function of many variables, if the structure of this function is known. As such a

function is considered in the algorithm function and network errors, the fact that the structure of the error function is completely determined by the network architecture, neural network, which is assumed to be known. Backpropagation can be very slow especially for multi-layer networks, where the surface of the objective function is nonquadratic, and high-dimensional nonconvex with many local minima or flat areas. Initialization of the synapses of the neural network has a huge impact on the number of training iterations. Because how well the chosen initial values of the coefficients *sipaptycheskih* depends how long the network through training and the adjustment will look their best values, and if it finds them.

As the training set used by a collection of images from different sources. This collection effectively covers the variability and richness of the natural data, to teach this system to work in the real world. In this paper, uses a window size of 36 * 32 pixels, containing the image of the sky. In preparation for training, monitoring and test statistics do not satisfy any normalization of images (histogram equalization and brightness correction). To create a large number of examples and an increase of invariance, it is advisable to apply a series of transformations, including reflection, rotation of $\pm 360^\circ$.

References:

- [1] LeCun Yann, Denker J.S., Solla S., Howard R.E., Jackel L.D.: Optimal Brain Damage, in Touretzky David (Eds), *Advances in Neural Information Processing Systems 2 (NIPS*89)*, Morgan Kaufman, Denver, CO, 1990
- [2] LeCun Y., Bengio Y.: Convolutional Networks for Images, Speech, and Time-Series, in Arbib M. A. (Eds), *The Handbook of Brain Theory and Neural Networks*, MIT Press, 1995
- [3] LeCun Y., Bottou L., Orr G., Muller K.: Efficient BackProp, in Orr G., Muller K. (Eds), *Neural Networks: Tricks of the trade*, Springer, 1998
- [4] LeCun Y.: Generalization and network design strategies // *Proc. of the Intern. Conf. Connectionism in Perspective*. -University of Zurich, 10-13 October 1988. - P. 143-155.
- [5] Makarenko A.A., Kalaida V.T.: localization method for face image video surveillance systems based on neural network. *Proceedings of the Tomsk Polytechnic University*. 2006. T. 309. № 8

Intelligent training system for advanced spacecraft pilot

A. P. Lastochkin, V. Y. Mamaev, State University of Aerospace Instrumentation, Saint-Petersburg, Russia

Process of operator training consists of a theoretical study of some problems (course), practical training on the simulator and working with the real object. In this case there is a gap between the stages of theoretical training and practical training. For gap exclusion it is requested to include in the simulator intelligent tutoring system (SITS). Knowledge representation in such systems is done by a hierarchical semantic network (HSN), consisting of concepts (nodes) and relationships (arcs) between them.

INTRODUCTION

The Cosmonaut Training Center Yuri Gagarin from 1969 is a department of cosmonaut training in navigation and ballistic support of space flight. Astronauts get knowledge of navigation, astronomy, cartography, theory of flight, navigation and ballistic flight operations of spacecraft. The main objectives of the cosmonaut training in navigation support of space flight are:

- The acquisition of solid knowledge of the foundations of the astronauts of space navigation, as well as methods and means of the orientation of manned space vehicles;
 - To develop skills to address the problems of navigation and orientation through the implementation of on-board equipment and systems;
 - Development of skills and abilities to use on-board navigation systems, navigation meters, optical and visual means of navigation and orientation.
- By developing projects manned missions to the Moon and Mars, and in the future to other planets began leading space countries. Such flights are not possible without the use of autonomous navigation.

The use of satellite navigation systems, inertial navigation systems, digital astronomical finders and the ability to install on-board computers allow you to completely solve the problem of navigation on board a new qualitative level. In this case the astronaut will take part in solving the problems of navigation [1]. A special role in training astronauts space flight simulators. It is almost impossible to run training like a space flight training flights in aircraft because of their high cost and safety. The practice of training operators in various educational institutions shows that while traditional forms and methods of instruction have not lost their significance, they at the same time have some significant drawbacks and limitations. One of these restrictions is the gap between the theoretical and practical training. This leads to the fact that even with a good theoretical knowledge, learning, transition to the integrated simulator virtually no control over the relevant system. For specialized simulators can identify a number of shortcomings:

- the complexity of an individual approach to learning and continuous control of the deficit at the time of teachers;
- Inadequate training impacts individual psychological characteristics and level of training;

One possible way of constructing an automated training system (ATS) is the use of models, algorithms, procedures, interactions, etc., obtained in

the theory of multi-agent systems (MAS). Benefits of EPA and MAS in particular [2]:

- Flexibility. Ability to study in a convenient time, in a convenient location and speed. Unregulated period of time to develop discipline.
- Modularity. The possibility of a set of independent courses - modules to form a curriculum that meets individual or group needs.
- Coverage. The simultaneous treatment of many sources of educational information (digital libraries, data banks, knowledge bases, etc.) of a large number of students. Communication via a network connection to each other and with teachers.
- Economy. Effective use of training areas, facilities, vehicles, concentrated and unified view of multi-access training information, and it reduces the cost of training.
- Manufacturability. Use in the educational process of the latest achievements of information and communications technologies to promote rights in post-industrial world information space.
- Internationalism. Exports and imports of world achievements in the education market.
- The new role of the teacher. EPA expands and updates the role of the teacher who must coordinate the learning process, continually improve the courses taught by them, to improve the creativity and skills in accordance with the innovations and innovation.
- The use of artificial intelligence for problem solving in training.
- Working with the domain ontology.
- Decision support for students.

Using agent-oriented approach to building software allows ATS further explore and develop intelligent learning environment. Thus, the theory of MAS can be used as a basis for building complex intelligent information systems for creating simulators that meet modern requirements. The basic concept in the theory of the concept of MAS is an intelligent agent, which refers to a software entity capable of not only the ability to transform information and to conduct, allowing to organize its interaction with the environment. This approach to the representation of interacting objects can be regarded as objects that have some intelligence, whose presence provides the opportunity to simplify development and debugging fairly complex systems. Such objects are called intelligent agents. Intellectualization of the components of distributed systems can extend the functionality and standardize the methods of interaction between them.

Example of MAS architecture presented on (Fig. 1).

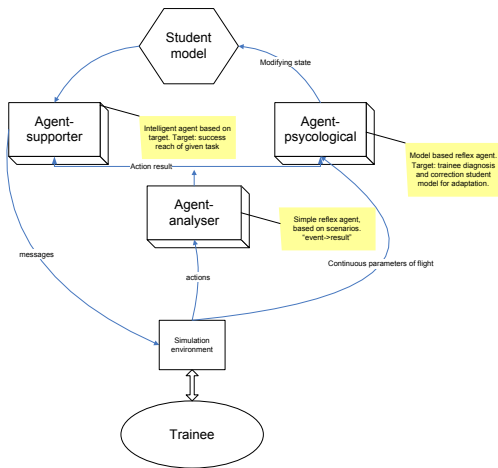


Fig. 1. MAS Architecture

The learner interacts with the simulator environment, performing actions for the management equipment and reading the readings. Student model is a whole set of characteristics of the student, measured during operation with the student and determines the degree of assimilation of knowledge on the subject studied and techniques (rules) treatment of this set [3]. Primarily, these rules must meet the challenges of the model trained on the results of his work with the system.

Student model should include information such as:

- learning objectives;
- student's knowledge of the course within the (current status of the learning process);
- about the features of supply of educational materials and selection of control tasks and issues;
- on the rules changes the student model based on the results of working with students.

As a student model uses an overlay model. Actions performed with the simulator environment are relayed to the agent parser with filters and selects events that are relevant to learning objectives. The work describes a special agent of the language with a set of conditions and actions. The generated events are fed to the agent, "psychologist", which determines the level of tension in the student and, if necessary, change the student model to adapt to the level of tension. Agent assistant based on a model student and the incoming events decides whether clues. In the stands as a model decision tree (Fig. 2).

Example:

The task of correcting Strapdown inertial system (SINS) of the optical sighting device driver 240k (EP-2).

Rules for the analyzer:

Condition	Message
It took 50 seconds and put the coordinates of the stars	Setting stars OK
It took 50 seconds and the coordinates of the stars are not entered	Setting stars DISCLAIMER
It was more than 60 stars and the coordinates are not introduced or modified	Setting stars re DISCLAIMER
It was more than 60 seconds and set coordinates of the stars	Setting stars re OK

It took 70 seconds. and enabled correction SINS	Set SINS OK
It took 70 seconds. and enabled correction SINS	Installing NO SINS
It took 80. and enabled correction SINS	Installation re SINS NO
It took 120 seconds. dimensions of the first stars are correct	Performing a measurement OK
It took 120 seconds. dimensions of the first stars are incorrect or missing	Performing a measurement of NO

Agent psychologist:

Analyzes the frequency of correct / incorrect actions, changes of aircraft. Action amends the student model: changing levels of complexity, tension.

Agent-assistant:

for different levels of a different number of tips of the tree for a normal student:

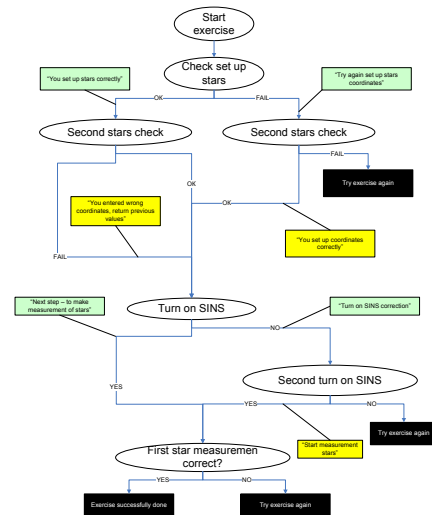


Fig. 2. Example decision tree for the student in the problem of correction

The solution to this problem is relevant not only for training operators of spacecraft, but also for other activities. To describe the domain model used in our ontology [4], which can be structured in sections of disciplines, concepts, and relationships between them. At present, the standard ontology description language can be considered as OWL [5]. The teacher can correct and supplement the training courses, without programming, and visual editing graph concepts. The OWL Web Ontology Language is designed for use by applications that need to process the content of information instead of just presenting information to humans.

References:

- [1] А.А.Митина: Некоторые вопросы подготовки космонавтов по навигационно-баллистическому обеспечению космического полета; научные чтения памяти К.Э.Циолковского, г. Калуга, Россия, 2006 г.
- [2] Д. Н. Кудинов: Перспективы разработки автоматизированных обучающих систем; Технические науки №6, 2006 г.
- [3] Глова В.И., Дуплик С.В.: Модели педагогического тестирования обучаемых; Вестник Казан. гос. Техн. ун-та им. А.Н. Туполева. 2003, №2. С. 74 – 79
- [4] Добров Б.В. , Иванов В.В. , Лукашевич Н.В. , Соловьев В.Д.: Онтологии и тезаурусы: модели, инструменты, приложения, 2009
- [5] OWL (Web Ontology Language) <http://www.w3.org/TR/owl-features/>

Analysis of the Concept and Prospects for Developing a Network of Micro- and Nano-Satellites for Research and Commercial Applications

Alexander V. Nebylov, Professor, Director of International Institute for Advanced Aerospace Technologies of Saint Petersburg State University of Aerospace Instrumentation, Chief of Department #11

Keywords: *nano-satellites, micro-satellites, classification, functional effectiveness, Earth monitoring, resolution, orbit and attitude control, cost of production and launch*

Classification of small satellites is performed. Main systems and units essential for satellites are listed and the opportunities of their microminiaturization and mass reduction are discussed. The concept of a small satellite bus structure unification and mass production is considered. The directions of great activity of many universities and enterprises for nano- and micro-satellites design and creation are analyzed. The opportunities for small satellites cheap launch are analyzed. Some ways of commercial application of nano- and micro-satellites are offered.

1. INTRODUCTION

For almost 55 years since the launch of the first artificial Earth satellite on October 4, 1957, the global cosmonautics has been overcoming the long way. Near-earth space exploration and the obvious benefit to earthlings in terms of monitoring, navigation and telecommunications have been achieved through the development and widespread use of several generations of various satellites and elements of the ground infrastructure. The number of "space" countries that already have their own satellites reached several dozen, and far much countries want to join the "space" pool.

The cost of specific practical tasks solution for particular country can be minimized by the way of international cooperation or purchase already developed space technologies. However, a large number of countries and even particular universities and firms desire to have their own satellite. It should be noted that the term "own satellite" is usually associated mostly with the presence of the opportunity to assign the desired satellite name, the capability of the satellite control, the application of the results of its operation. As for the main structural elements of the satellite, technology of its manufacture, method of injection into orbit, these issues may be easily solved by purchasing the relevant services in the world space market, and it is often practiced for "own satellites", first of all for micro- and nano- ones.

However, the question arises: how is the development of micro- and nano-satellites as a new class of spacecraft objectively justified? Is it the direction of space technology development of a real technological challenge for solving the common tasks of monitoring, communication, navigation, near space investigation or is it merely the result of

the appearance of technical capabilities for creation of small satellites with a small cost? Is the small satellite design the optimal solution for any reasonable comprehensive quality criteria or is it just the result of severely restricted the satellite cost? The paper attempts to answer these questions.

¹ The work was supported by the Russian Foundation for Basic Research under the project 09-08-00529.

2. CLASSIFICATION OF SMALL SATELLITES

Classification of satellites may be done on the bases of analyzing their mission, mass and dimensions, parameters of orbit and many other factors [1]. For the purposes considered in this paper the mass of launched satellite is especially important. Seven categories of satellites are known presently (Tab. 1) and only Micro-satellites (category 4) and Nano-satellites (category 5) are really developed during the last 1-2 decades and became rather widely used. As for Pico-satellites and especially Femto-satellites, they are the subject for future technological achievements and probably are interesting for local application in the neighbour zone of space stations, not for independent orbital use.

The three kinds of satellite orbit can be generally considered.

Low Earth orbit (LEO) has the altitude up to 2000 km. **Medium Earth orbit (MEO)** is characterized by the altitude from 2000 km to just below geosynchronous orbit at 35786 km. **High Earth orbit (HEO)** could be located above the altitude of geosynchronous orbit 35786 km. Practically all existing micro-satellites and nano-satellites were injected into

LEO because it is the cheapest orbit and it is not required the great power of onboard radio transmitter. Correspondingly, the duration of such LEO keeping may be 3-5 years only. In many cases the small satellites become unserviceable quicker due to bad influence of space environment.

When Classification of satellites by mission is considered, the following main types of vehicles may be listed.

#	Category	Mass Range (kg)
1	Large satellite	> 1,000
2	Medium-sized satellite	500-1,000
3	Minisatellite	100-500
4	Microsatellite	10-100
5	Nanosatellite	1-10
6	Picosatellite	0.1-1
7	Femtosatellite	< 0.1

Earth observation satellites are intended for such use as map making, environmental monitoring (including pollution of sea, polar ice area, floods, forest fires, etc.), meteorology, weather forecasting, etc. Micro- and nano-satellites really can perform such functions, especially if the required resolution of pictures is low and the flow of data is rather weak. For example, many projects of nano-satellites are devoted to forest fires recognizing, when low resolution in 100m is sufficient, but the periodicity of taking pictures has to be 1-3 hours. 50-100 nano-satellites are necessary for creation the global system of fires detection.

Communications satellites are carrying in space the functions of telecommunication. Most of them have geosynchronous HEO. Performing the tasks of telecommunication requires the essential onboard power supply for active repeaters, and it is a problem for small satellites with limited area of solar panels. Too broadband and multichannel communication systems require large satellites, but some particular functions of telecommunication may be solved with Micro- and nano-satellites application. Navigational satellites use radio time signals transmitted to enable mobile receivers on the ground to determine their exact location. They have distributed MEO, powerful radio transmitter and many other complex equipment. Small satellites are not used for such purposes.

Astronomical satellites are used for observation of distant planets, galaxies, and other outer space objects. An array of small satellites may be applicable for such tasks by forming the distributed phased array, but related motion of all satellites must be precisely controlled for it.

Reconnaissance satellites are Earth observation satellite or communications satellite deployed for military or intelligence applications. Of course, generally Micro- and nano-satellites could be applied for such purposes, especially taking into account the opportunity to launch such satellite to the required orbit in a short time. Small satellites may be also more complex target for any space weapon in comparison with large satellites.

Anti-Satellite weapons or "Killer Satellites" are satellites that are designed to destroy enemy warheads, satellites, other space assets.

Some times large number of weapon is more important than its high performance, in this cases small satellites may be used.

Scientific satellites are used for location the pure scientific equipment, sensors of different physical quantities. Micro- and nano-satellites may easily perform such tasks. For example, the sensors of magnetic field are installed at a number of Micro-satellites created by universities. Any device or unit which is necessary to test in space environment can be installed aboard small satellite also. It permits to test new hardware with reduced expense in testing. Furthermore, since the overall cost risk in the mission is much lower, more up-to-date but less space-proven technology can be incorporated into micro-satellites with less risk.

Educational satellites can serve for training students in creation of any equipment for satellites or for implementation the concept of distant education. Presently these purposes are mainly used for reasoning the creation of satellites micro- and nano-satellites in the universities. Several decades of universities in many countries have announced or already realized such projects.

3. SATELLITE MAIN MODULES AND STRUCTURAL SUBSYSTEMS

The following units are the attributes of any satellite, including micro- and nano-satellites/

The structural subsystems provide the mechanical base structure, shields the satellite from extreme temperature changes and micro-meteorite damage, and controls the satellite's spin functions.

The Power Subsystems consists of solar panels and backup batteries. Nuclear power sources (Radioisotope thermoelectric generators) have been used also in several satellite programs, but presently it is not popular.

The Thermal Control Subsystems protect electronic equipment from extreme temperatures due to intense sunlight or the lack of sun exposure.

The Attitude and Orbit Control Subsystems consist of small rocket thrusters that keep the satellite in the correct orbital position and keep antennas positioning in the right directions. Larger satellites usually use monopropellants or bipropellant combustion rockets for propulsion and attitude control. Micro- and nano-satellites use electric propulsion, compressed gas, vaporizable liquids such as butane or carbon dioxide or other innovative propulsion systems.

The Telemetry Subsystems (Command and Data Handling) monitors the on-board equipment operations, transmits equipment operation data to the ground control station, and receives the ground control station's commands to perform equipment operation adjustments. Micro-satellites can use conventional radio systems in UHF, VHF, the S-band and X-band, although often miniaturized using more up-to-date technology as compared to larger satellites.

Communication payload, mainly aboard transponders. A transponder is capable of receiving uplinked radio signals from earth satellite transmission stations (antennas), amplifying received radio signals,

sorting the input signals and directing the output signals through input/output signal multiplexers.

Useful payload is intended for performing the main mission of the satellite. For the Earth observation satellites it is optical devices and cameras with the necessary means of target designation, and probably image processing and compression.

4. OPPORTUNITIES FOR HARDWARE MICRO-MINIATURIZATION

Any satellite should be considered as a complex engineering system with elements of electronics (low-current, power, microwave and other types of devices), computer technology, optics, mechatronics, electro-mechanics (including MEMS), electric power generation elements, chemical physics (jet propulsion based on fuel combustion and other principles) and many other elements, usually specially developed for space application conditions. Part of these elements is really exposed to persistent a trend of miniaturization, but another part - not.

The dimensions and weight of the low-current elements of electronics and computer technologies are rapidly decrease. Personal computers, mobile phones, including – satellite ones, the other consumer electronics with almost six-month cycle of generations change demonstrate even a hardened skeptic that microminiaturization - one of the main trends of technological advance in these areas. Of course, space is not the place for cheap consumer electronics. Electronics need to be rigorously tested and modified to be "space hardened" or resistant to the outer space environment (vacuum, microgravity, thermal extremes, and radiation exposure). But electronic components which are resistant to the harsh radiation and temperature conditions are also being developed as a part of this trend.

The reducing of the dimensions of the elements of power electronics is not so appreciable and limited, in principle, by the need of heat removal. Further limitations exist for the microwave electronics, where the dimensions of waveguides and antennas are largely determined by the used frequency range. Fortunately, presently the new approaches for antennas construction appeared, but for narrow-beam antennas the progress in microminiaturization is not so great.

Satellite energetics, available onboard power supply is one of the key factors determining the ability of its active operation, especially the amount of data transferred to ground terminals and modes of control or at least stabilized satellite motion. It is known that the classical problem of noiseproof data signal reception may be successfully solved only at a sufficiently high signal to noise ratio in the used frequency range. Implemented in high-performance filters now allow for a clear form the desired frequency range, but cannot improve the potential characteristics of radio transmission. The transmitter power will always be crucial significance for the permissible rate of data transfer for a noiseproof radio link.

Concerning satellite power supply any revolutionary innovations are hardly to occur in the near future. Solar panels are still the most effective and natural source of onboard power, and creation a reserve of electric power is performed by rechargeable batteries (the attempts to

remove accumulators are undertaken only when the regime of a satellite "silence" at an orbit dark side is admissible). The quality of space solar panels has gradually been increased in terms of efficiency factor and durability, possibly by tens of percent, but not by several times. It is clear that even with close to 100% of solar battery factor of efficiency the generated power is determined by the flow of solar energy and the area of solar panel. It is wellknown that the solar constant is only 1367 W/m^2 (). For small satellites the area of solar cells is limited by structural factors that determine the fundamental shortage of on-board power supply. The mode of angular stabilization of small satellites is usually not associated with orientation of the panels at the Sun that also reduces the power output by the cosine law.

This year the options for energy supply from on-board nuclear power sources have become even less likely in connection with the peak of negative attitudes of public and governments of many countries to nuclear power.

The satellite angular stabilization in one or another form needs to implement the majority of functional tasks assigned to the satellite. Natural stabilization, for example, in Earth's magnetic field poor corresponds to the real needs of stability in the terms of laws and accuracy. Accuracy requirements depend on the angular stabilization mode and may be easily evaluated. For example, for "targeting" with an accuracy of 100 meters in photographing the earth's surface from the medium-high orbit satellite the allowable angular error can be estimated as approx. 1 ang.min .

In reality, such precision can be achieved by combination of satellite "physical" attitude stabilization and the "electronic" image stabilization in a camera or other on-board instrument. But in any case the high precision sensors of angular position would be required, such as positional star sensors and fiber-optic gyroscopic sensor of angular velocity. Both sensors cannot be microminiaturized. The high-quality optics also cannot be microminiaturized as the aspect ratio of the object lens and the eye-lens is important.

The launch of a single micro-satellite requires the special technologies and the specific cost of launch may be higher against «large» ones. Launch of many micro-satellites, some times together with a heavy spacecraft, by a single launcher is not suitable in the terms of required orbits shaping (but really it is widely used presently). Some publications on the success in this field are doubtful. Many projects of launchers creation for micro-satellites were announced, including the horizontal launch with ekranoplane assist [2]. Development of "micro-launchers" for micro-satellites is not easy and requires the separate finance.

5. GENERAL ADVANTAGES AND LACKS OF NANO- AND MICRO-SATELLITES

It is possible to consider a few additional nontechnical features of small satellites that are important for their usefulness estimation.

One of the main achievements of international team of designers working in the field of small satellites creation is the concept of maximum unification of hardware and software for different types of small satellites. Earlier each great firm developed own structure of any certain sa-

tellite and special units for onboard equipment. Using of the same units at many different satellites permits to increase the production volume, make the production industrial and cheap. Of course, the competition among many enterprises for such production will take place.

Another advantage consists in essential reduction of the term of development and production of small satellites in compare with large ones. A team of several persons can perform such work and any complex agreements between many enterprises are not necessary.

Two disadvantages are also essential. At first, the potential opportunities of small satellites to solve many tasks are smaller versus large satellites without strong limitations on mass and dimension. At second, the problem of space garbage becomes more essential with development of great number of small satellites.

6. CONCLUSIONS

The main advantage of micro- and nano-satellites is a low cost of their development, production (especially mass industrial production) and launch. A thousand of nano-satellites could be created instead of one large satellite. But the achieved quality of mission performance for large satellite may be several times greater than for micro- and nano-satellites. For example, the Russian satellite for Earth surface monitoring Resurs-DK with with 6.5 ton mass provides ground resolution in 2m and a great accuracy of pointing, but a nano-satellite could provide resolution in 50 m and bad referencing of the obtained pictures to the

coordinate frame. But periodicity of taking pictures for one Resurs-DK is 6 days, and it may be done 3 hours only at launch of 48 satellites. For weather forecasting or for fire recognizing the effect from 50 nano-satellites may be greater than from one large satellite, and a lot of money could be saved.

Nano- and micro-satellites could be very useful also at testing any hardware in space environment and of course for educational purposes.

Detailed analyzing of all essential aspects of micro and nano-satellites permits to conclude that they cannot drive the large satellites out of a space market as some essential functions could not be performed by them well. Micro-, nano- and even pico-satellites may be really useful in a few rather fields of space technologies, especially if these space vehicles have a flight in array.

References:

- [1] F.-B. Hsiao, ed. *Microsatellites as Research Tools*. Pergamon, 1999.
- [2] Tomita N., Nebylov, A.V. et al. (1999). Performance and Technological Feasibility of Rocket Powered HTHL-SSTO with Take-off Assist. *Acta Astronautica*, 45, No.10, pp.629-637.

Calculation of Temperature Fields of Vibrating Composite Part

Ing. Vilém Pompe, Ph.D

A composite part subjected to a cyclic strain produces heat which can be recorded by a thermographic camera. The thermograms obtained have various forms of exploitation, e.g. inspection of local temperatures, contact-free identification of natural vibration modes or selection of optimal location of strain gauges. The distribution of temperature across the surface of the vibrating part may also be obtained by calculation using the FEM and material constants acquired through experiments. Calculations based on the reference thermograms may be further used for conversion of temperature fields as a function of changed size of the cyclic loading displacement. This possibility is crucial e.g. for planning the fatigue tests where overheating and irregular failure need to be avoided.

Symbols used		
$\Delta Q, \Delta q$	Heat increase, specific heat increase	[J, J/kg]
C, c	Heat capacity, specific heat capacity	[J/K, J/kg.K]
ΔT	Temperature variation	[K, °C]
m	Weight	[kg]
ΔU	Strain energy increment	[J]
S	Area	[m ² , mm ²]
t	Thickness	[m, mm]
ρ	Density	[kg/m ³]
ξ	Loss coefficient	[1]
F	Active force	[N]
K	Stiffness	[N/m, N/mm]
Δu	Displacement, amplitude of displacement	[m, mm]

TEMPERATURE CALCULATION

For the purpose of material heating, the following relation between heat and temperature is assumed:

$$\Delta Q = C \cdot \Delta T \quad (1)$$

Or for one kilogram of substance:

$$\Delta q = c \cdot \Delta T, \text{ where } \Delta q = \frac{\Delta Q}{m}, c = \frac{C}{m} \quad (2)$$

In order to deal with laminate material composed of individual monolayers the relation (1) has to be modified so that heat capacity of the

laminate element is expressed as the sum of the capacities of the individual layers:

$$\Delta Q_e = \Delta T_e \cdot \sum_{i=1}^n c_i \cdot m_i \quad (3)$$

Actual calculation is assumed to be carried out using the method of finite elements, which practically means that some important data, such as weight, thickness and area of the mesh element, need to be read from the model database. Otherwise, an isolated calculation will be carried out as a matter of course. Relation (3) is transcribed using area "S" of element "e" of the mesh, thickness and density of individual monolayers:

$$\Delta Q_e = \Delta T_e \cdot \sum_{i=1}^n c_i \cdot S_e \cdot t_i \cdot \rho_i \quad (4)$$

As regards specific heat per one kilogram of substance, the following should apply (the element area is the same for all the monolayers):

$$\Delta q_e = \Delta T_e \cdot \frac{S_e \cdot \sum_{i=1}^n c_i \cdot t_i \cdot \rho_i}{m_e} \quad (5)$$

From which the specific heat capacity of the laminate element is derived as:

$$c_e = \frac{S_e \cdot \sum_{i=1}^n c_i \cdot t_i \cdot \rho_i}{m_e} \quad (6)$$

Using (1) and (6), the value of heating of one element can be expressed as:

$$\Delta Q_e = c_e \cdot m_e \cdot \Delta T_e \quad (7)$$

The vibrating body is deformed and accumulates mechanical energy one part of which is converted into heat through the process of loss. Within one period, the analysed element "e" reaches two amplitudes, therefore it can be assumed that the corresponding heat loss relates to double amount of the value of the maximum contained strain energy:

$$\Delta Q_e \approx 2 \cdot \Delta U_e \quad (8)$$

The dissipated heat is assumed to be the multiple of this value, expressed as the loss coefficient:

$$\Delta Q_e = \xi_e \cdot 2 \cdot \Delta U_e \quad (9)$$

The relation (9) is substituted to (7) and the change in temperature is expressed depending on material characteristics and strain energy of the element as:

$$\Delta T_e = \frac{2 \cdot \xi_e}{c_e \cdot m_e} \cdot \Delta U_e \quad (10)$$

The relation (10) yields a value corresponding to the steady state of the vibrating part. It does not depend on anisotropy directions, symmetry or balance of the composition of the laminate. It is theoretically possible to determine the specific heat capacity and the density of each layer; however, it is problematic to determine the mathematical expression of the loss coefficient ξ . The relation (10) may be simplified as:

$$\Delta T_e = A_e \cdot \Delta U_e \quad (11)$$

Constant A_e of a particular laminate composition can be determined using a thermographic camera; and provided the specific heat capacity, density and thickness of the layers are known even the loss coefficient ξ_e of the element may be separated. These characteristics will be considered to be the material constants independent of displacement, frequency and temperature.

AMPLITUDE DEPENDENCE

The conversion of temperature fields as a function of the height of displacement amplitude will be based on the following deliberation.

Let us assume that every new displacement vector in the model nodes is just a k-multiple of the previous vector, or the basic vector. This is particularly true of the modal analysis, where the natural mode proper to the given frequency is constantly the same and the displacement ratios are maintained for various excitations at this frequency. The condition is also fulfilled for certain cases of controlled cyclic loading, where directions and points of action of individual effects of loading remain the same, and their sizes are also a k-multiple of the basic case, e.g. uniaxial loading of a rod, spar bending by a discrete force or a system of forces, etc.

Then, it is sufficient to identify the theoretical dependence of the strain energy change on the changed displacement at the reference point. The strain energy increment imposed by the applied force on a linearly elastic element is expressed in the following equation:

$$\Delta U = \frac{1}{2} \cdot F \cdot \Delta u \quad (12)$$

$$F = K \cdot \Delta u \quad (13)$$

After substitution:

$$\Delta U = \frac{1}{2} \cdot K \cdot \Delta u^2 \quad (14)$$

$$\Delta U_{j+1} = \Delta U_j \cdot \left(\frac{\Delta u_{j+1}}{\Delta u_j} \right)^2 \quad (15)$$

By incorporating relations (11), (15), reference temperatures prior to loading and experimentally measured temperature increment at a nominal displacement (amplitude) at the reference point, we can roughly calculate the new temperature for new nominal displacement of the system as follows:

$$T_{j+1} = T_{ref} + \Delta T_{exp} \cdot \left(\frac{\Delta u_{j+1}}{\Delta u_{exp}} \right)^2 \quad (16)$$

Example calculation:

Let us assume the modal test performed on the composite propeller blade. During experiment, the steady temperature for the reference blade displacement (e.g. the blade tip at the trailing edge) of 1.8 mm

rose at the observed point by 2.6°C (difference between the final and initial temperature). The blade subsequently cooled to a temperature of 16.4°C. What will be the steady temperature at the observed point after inducing new displacement of 5.8 mm at the reference point at the same natural frequency?

$$T_2 = 16,4 + 2,6 \cdot \left(\frac{5,8}{1,8} \right)^2 = 43,4^\circ C$$

The performed experiment determined the steady temperature of 45.7°C for the aforementioned displacement. The concordance between the calculated and measured temperatures corresponds to the accuracy of simplified experiment and may be considered sufficient for the given purpose.

VERIFICATION BY TEST

The proposed calculation method was tested on an experimental VZLÚ V45 propeller blade for the first three natural vibration modes. A sequence of three displacement amplitudes of the reference point was selected for each vibration mode, the displacement was measured using a contact-free laser sensor. The propeller blade was clamped in a special vibrator-activated fixture, and the effects of ambient temperature fields were partially eliminated by means of an insulating box. Fig. 1 shows the measurement configuration, Fig. 2 and 3 represent an example of a thermogram and a corresponding FEM analysis.



Fig. 1: Composite propeller blade mounted in a special fixture for excitation of the first three natural vibration modes. The thermograms were taken using a thermal insulating box.

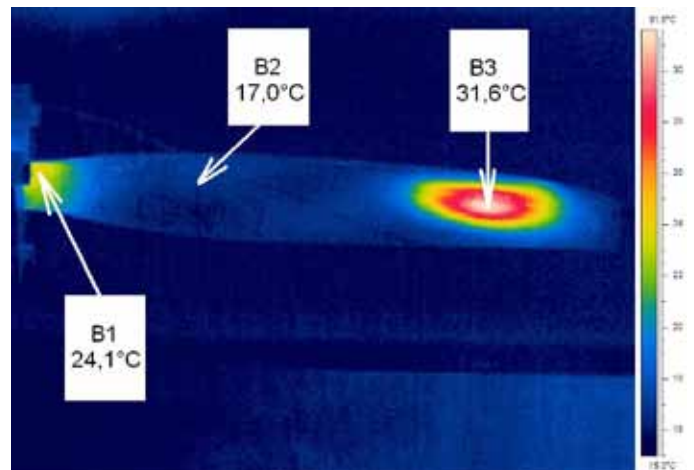


Fig. 2: Thermogram of the third natural vibration mode, suction side of the blade VZLÚ V45.

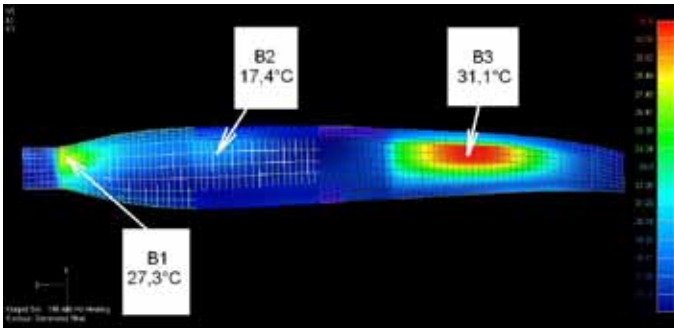


Fig. 3: FEM analysis of thermal fields of the third natural vibration mode, suction side of the blade VZLÚ V45.

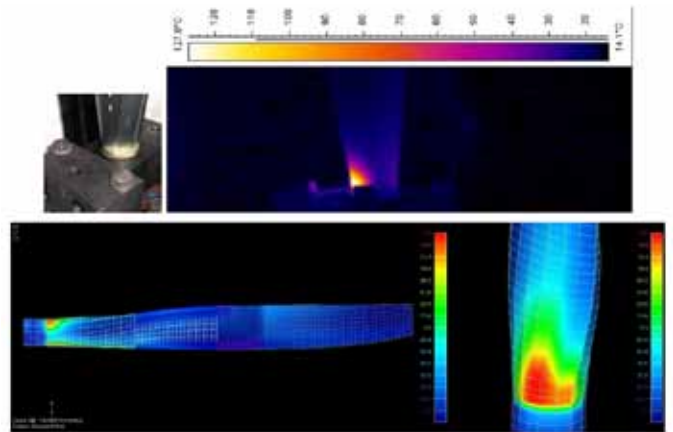


Fig. 3: FEM analysis of thermal fields of the third natural vibration mode, suction side of the blade VZLÚ V45.

Reference amplitude [mm]	2			4 (see Fig. 2 and 3)			6		
Point of temperature reading	B1	B2	B3	B1	B2	B3	B1	B2	B3
Thermography	17.5	16.7	19.1	24.1	17.0	31.6	36.3	19.1	45.2*
FEM	19.3	16.8	20.1	27.3	17.4	31.1	43.7	21.6	51.3

Table 1: Comparison of thermography results and the conversion of FEM results of the third natural vibration mode

*) The maximum measured temperature of 50.1° C, i.e. a value much closer to FEM, has been detected in the close proximity.

Table 1 shows an example of the comparison of a thermogram with FEM analysis carried out for the three most significant points. The VZLÚ V45 blade was excited to reach the third natural vibration mode and a thermogram of the suction side at reference amplitudes of 2, 4 and 6 mm was subsequently taken. The aim was to verify the applicability of the relation (16) for the conversion of temperature fields and to compare the measurement results with the theoretical calculation according to (10).

Currently, no loss coefficients or specific heat capacities of individual layers, which at the same time represent the material function and volume proportions of the individual composite phases, are available. Their measurement, or identification of an effective method of determination, will be subject to further development of the method. At present, temperature fields are being calculated based on the FEM modal analysis and a reference thermogram using the following formula:

$$T_2 = T_{ref} + A \cdot \Delta U_{MKP} \cdot \left(\frac{\Delta I_2}{\Delta I_{exp}} \right)^2 \quad (17)$$

At first, the ratio of reference amplitudes is stated $\Delta I_2 / \Delta I_{exp} = 1$, and then the constant for each element (or composite composition) is tuned off on the basis of the reference thermogram. To convert to other displacements, the relevant ratio of reference amplitudes is substituted as necessary, i.e. ΔI_{exp} is substituted with a value proper to the thermogram obtained, and ΔI_2 is substituted with a reference value to which the temperature field needs to be converted.

The images below show further examples of how thermography and the aforementioned calculation methods are used.

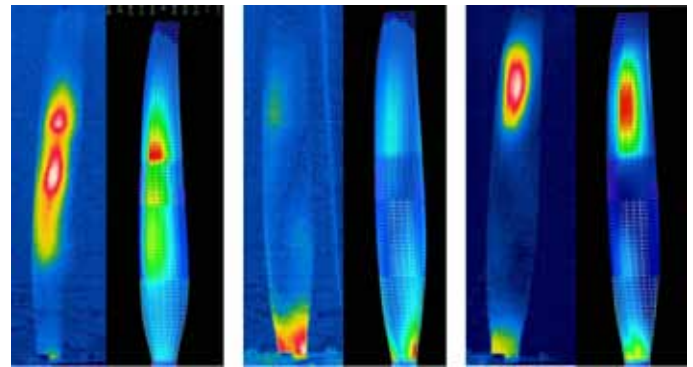


Fig. 5: Contact-free identification of the natural vibration modes, using the thermography and FEM analysis of the temperature distribution across the surface of the VZLÚ V45 propeller blades.

CONCLUSION

The method of calculation of temperature fields presented in this document is currently at the stage of experimental verification. The final aim of the researcher is to generalize this method so that it can be applied to any periodic mechanical load imposed on a composite material, i.e. not only in the case of natural vibration modes.

Furthermore, it is necessary to devise practically applicable methods of determination of requisite material constants. As regards specific heat capacities, it may be assumed that their values are calculable. Loss coefficients will presumably draw on empirical data obtained from measurements of typical material systems allowing for the effect of volume proportion of the individual composite phases.

Properties of ejecta generated at high-velocity perforation of thin bumpers made from different constructional materials

N.N. Myagkov^{a)}, T.A. Shumikhin^{a)}, L.N. Bezrukov^{b)}

a) Institute of Applied Mechanics of RAS

b) State Research Institute of Aviation Systems (GosNIAS)

The series of impact experiments were performed to study the properties of ejecta generated at high-velocity perforation of thin bumpers. The projectiles were 6.35 mm aluminum spheres, the bumpers were aluminum plates and meshes weaved of steel wire. The impact velocities ranged from 2.2 to 3.2 km/s. In the experiments, the ejecta particles were captured with low-density foam collectors. The processing of the experimental results allowed one to estimate the quantitative and qualitative parameters of the ejecta particles: their spatial and size distribution data, and total masses of ejecta from different targets.

INTRODUCTION

A hypervelocity impact of a particle on a target is accompanied by a sufficient ejection of material in the semi-space from which the particle approached towards the target. This emitted material is called ejecta. Due to the ejecta phenomenon, the ejecta particles may represent a danger to exterior equipments of the spacecraft (the antennae, solar batteries, etc) [1]. Nowadays, the ejecta particles are considered as one of the main sources of the near-Earth space pollution [1, 2] that justifies an interest to their study.

In the present work, the series of impact experiments were performed to study the properties of ejecta generated at high-velocity perforation of thin bumpers. The aluminum projectiles had the 6.35 mm diameter and the bumpers were aluminum plates and meshes weaved of steel wire. The thin aluminum plate is the classic bumper providing protection of inner wall against a meteoroid or a space debris particle for manned spaceship. The mesh bumpers are also used in constructing protective system (see, for example, "Mesh Double-Bumper" [3] and protection of the Russian ISS module "Zarya" [4]).

SETUP OF THE EXPERIMENTS

The general scheme of the experiments is presented in Fig. 1. A two-stage light-gas gun accelerates the sabot with a projectile fixed in it up to velocities about 3.5 km/s. In the expansion chamber the couple of steel annular cutoffs separate the projectile from the sabot and the projectile moves further into the target chamber where the velocity-meter registers it velocity. The target is fixed in the end part of the target chamber. The interaction of the projectile with the target generates ejecta particles which penetrate into the collector placed in front of the target.

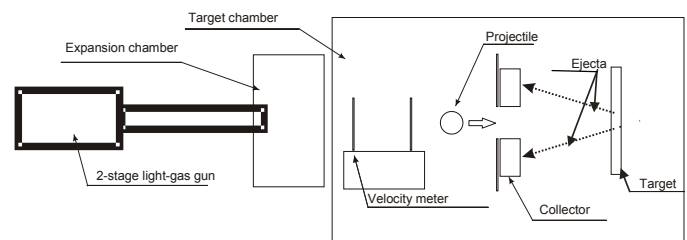


Fig. 1. The scheme of experiments with collectors

In all experiments a 6.35mm aluminium sphere of 2017 or AD1 aluminium alloy was used as a projectile and the impacts were normal to a target. The range of impact velocities was 2.2-3.2 km/s. For the targets we used: 1.45 and 3.0mm thick aluminium (AMg6) plates; three staked together 1.0 mmx0.32 mm steel meshes (0.32 mm is the diameter of the mesh wire and 1.0 mm is the gape between two neighbouring wires in the mesh) and a single 2.0mmx1.0mm steel mesh. All experiment data are provided in Table 1.

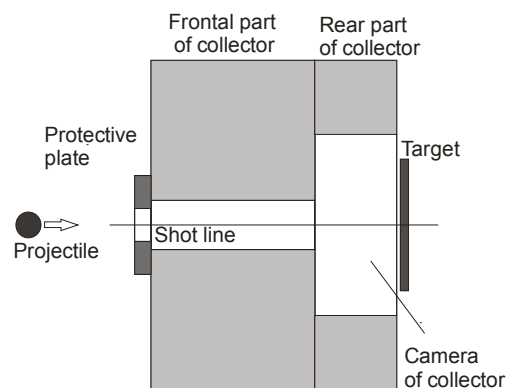


Fig. 2. Scheme of the foam collector (cross-section along the shot-line). The thickness of the frontal part is 100mm and 50mm for the rear part. The external diameter of the collector is 250mm; the internal diameter of the frontal part is 40mm; the diameter of the camera of the collector is 130 mm.

Collectors were made of 15kg/m³ polystyrene foam. They had a cylindrical form and consisted of two parts (Fig. 2). A protective plate to prevent the damage of the collector by shot-debris covered the frontal part. Along the symmetry axis of the collector a channel was made to provide projectile entering. In addition, the hole was made in the frontal protective plate. The impact of the projectile on the target attached to the rear part of the collector led to the emission of ejecta particles into the camera of the collector where they, having penetrated into the low-density collector material, were captured living visible traces of penetration on the camera surface.

The foam collector was put into a metal cylindrical shell. The full assembly was installed in the target chamber. The special measures were undertaken to provide accurate aiming providing the coaxiality of the assembly axis with the shot line. To extract the captured ejecta particles we used some available solvents. The extracted particles were weighted using the electronic laboratory balance (with accuracy up to 0.5 mg). The recovered substance was also studied using a metallurgical microscope.

RESULTS OF THE EXPERIMENTS

Selected experiments with recovered mass of ejecta are presented in Table 1. The external appearance of collector camera surfaces for collector #1 (shot #39422-1 with 1.45 mm aluminum plate) is as follow. The most intensive flow of ejecta particles is distributed along the circle of diameter 120mm according the traces on the back side of the frontal part of the collector (Fig. 3), which reflects a cone shape of the flow with the generating line of the cone making an angle about 45-48 degree from the shot line. The circumference distribution of particles in the cone-flow is quite inhomogeneous (Fig. 3). It reveals six zones of concentration of ejecta particles.

For the purpose of detailed analysis the frontal and rear parts of the collector were cut on six sectors. That allowed one to perform convenient visual inspection of the side wall of the collector camera (Fig.4) and recover the particles from each individual sector as well. Some amount of particles was knocked out of the target surface at grater angles according the imprints of the thread-like vertical traces (Fig.4) on the side wall of the collector camera. This means that during the process of perforation the angle of the ejecta cone increases starting with the lower angle where its intensity is maximum. The weight of recovered particles for twelve pieces of the collector (six for frontal and six for rear part) listed in Table 2. The number of quite large aluminum particles (more than 0.5mm in size), which was counted up visually, correlates though with the evaluated weight of substance for each sector (Table 2), which prove reliability of considered estimation.



Fig. 3. Rear side of the frontal part which was faced to a target (collector #1) Fig. 4. Part of the side wall of the camera of collector #1. The horizontal size is 60 mm. Fig. 5. Camera of collector #4

Collector #	Shot #	Velocity, (km/s)	Target, (mm)	Target areal density, (kg/m ²)	Total mass of recovered substance (g)
1	#39422-1	2,23	alum.(AMG6) plate, 1.45	3,97	0,0656
2	#39475-1	2,65	alum.(AMG6) plate, 1.45	3,88	0,0781
3	#39475-2	2,66	alum.(AMG6) plate, 1.45	3,88	0,0549
4	#39461-1	2,64	3 steel meshes 1.0x0.32	2,82	0,0187
5	#39461-2	2,52	3 steel meshes 1.0x0.32	2,82	0,0154
6	#39484-1	3,19	3 steel meshes 1.0x0.32	2,82	0,0166
7	#39556-1	2,70	alum.(AMG6) plate, 3.00	8,10	-
8	#39556-2	2,83	alum.(AMG6) plate, 3.00	8,10	-
11	#39581-1	2.61	1 steel mesh 2.0x1.0,	3.83	0,019

Table 1. Experimental shots and recovered mass of ejecta

Sector	Frontal part, (g.)	Rear part, (g.)	Total, (g.)	Number of particles with size bigger than 0.5 mm
1	0.0076	0.0047	0.0123	20
2	0.0017	0.0008	0.0025	8
3	0.0077	0.0077	0.0155	18
4	0.0074	0.0079	0.0153	14
5	0.0059	0.0064	0.0123	14
6	0.0058	0.0020	0.0077	12
Total:	0.0361	0.0295	0.0656	86

Table 2. Weight of recovered particles (collector #1)

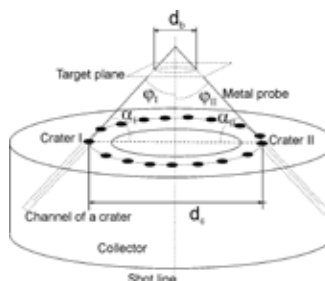


Fig. 6. Scheme of particle trajectories measurement.

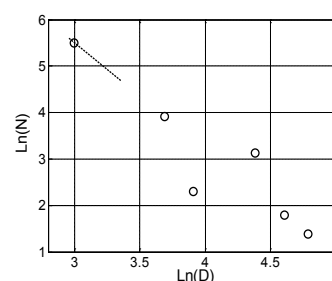


Fig. 7. The cumulative distribution: N (D) is the total number of channels whose depth is equal to or larger than D (collector #8).

One can see (Table 1) that the total mass of recovered particles (e.i. the ejecta mass) in experiments with meshes is sufficiently lower than that in experiments with plates. The reaction of the recovered dust (collectors #4-6, 11) on magnetic field reveals the presence of iron. This iron dust seems to be consisted of the finest ejecta particles knocked-

-out from the steel meshes. The exterior appearance of the surface of collector #4 (Fig.5) in experiment with the 3 steel meshes differs from the surface of collector #1 (Fig 3), which was obtained in experiment with the aluminum plate target. The surface of the collector camera is visually clean. There are no traces of inlet holes made by ejecta.

The ejecta flow from the impact on a 3mm-thick aluminum plate occurred to be quite intensive and inhomogeneous. That led to the formation of prolonged channels in collectors (up to 100 mm in length and up to several millimeters in width). They could be formed either large particles (the size of about ~ 1 mm) or jets consisting of smaller particles. Assuming that the particle trajectories are not affected by the event of particles contact with collector material, the direction of channels can be used for estimation of the angles at which the particles leave the target.

For this purpose thin metal probes were used (Fig. 6) and the following parameters were estimated: d_c - the distance between two opposite craters situated on an imaginary circle formed as intersection of an ejecta-cone and the plane of the surface of the collector rear surface, d_b - a diameter of the circle formed as intersection of an ejecta-cone and the plane of the target, φ_I - the angle between the trajectory of crater I and the the shot line (φ_{II} - an angle, consequently, for crater II). The retrieved parameters for collector #7 are presented in Table 3. The parameters reveal quite inhomogeneous distribution of the angle φ . One can see that in case of the 3 mm plate the average angle $(\varphi_I + \varphi_{II})/2$ of ejecta cone is 32.5-43 degree. Analogous measurements of the angles were made for collector #1 (experiment with 1.45 mm-thick aluminum plate).

Channel I	Channel II	db (mm)	dc (mm)	φ_I	φ_{II}	$\varphi_I + \varphi_{II}$
8	9	21	87	30	35	65
9	14	15.5	86.5	38.5	31.5	70
17	18	16	86	35	35.5	70.5
2	7	10.5	83	34	38	72
14	15	14	89.5	39	35	74
7	21	7	88	42.5	32.5	75
19	20	8	87	42	37	79
5	6	13	100	38	42	80
12	16	12	101	39	43.5	82.5
5	10	6	97	42	43	85
6	11	4	100	43	43	86

Table 3. Parameters of the ejecta trajectories (collector #7).

The depths of the channels were estimated as follow. Collector #8 (shot #39556-2) was sliced perpendicularly to the shot line into five similar 20 mm-thick slices. The images of the layer surfaces were digitally processed. The digitally improved visualization of the slices perforations allowed one to perform the correct counting of the quantity of the channels as a function of the channel depths. Since the channel depth depends on jet intensity, the distribution of channel depths reflects the distribution of kinetic energy of the jets. The graphical representation of the obtained data (Fig. 7) gives the linear dependence in the logarithmic scale that suggests that the distribution may fit a power law. One can see that this distribution has a peculiarity at the depths of 60-80 mm which breaks the fitting by power law.

CONCLUSIONS

In experiments with the aluminum plate, the matter in the ejecta is distributed quite inhomogeneously forming the deep channels having different depths in foam collectors (up to 100 mm in length and up to several millimeters in width for experiments with 3mm-thick aluminum plate). The channels could be formed either large particles (the size of about ~ 1 mm) or jets consisting of smaller particles. In fact, the imprints of the thread-like vertical traces (Fig.4) on the sidewall of the collector camera speak well for that the matter in the ejecta concentrates in the jets. Cumulative distribution of channel depths corresponds approximately to the power law. Trajectories of the jets form an ejecta cone. In experiments with the steel meshes, the jets were not observed in the ejecta.

Presence of the channels inside of the foam collector in experiments with aluminum plates allowed one to restore a trajectory of jets with high accuracy and to measure their slope angles. These slope angles were measured for aluminum plates of 1.45 mm and 3.0 mm thickness. It turned out these angles have appreciable dispersion. Moreover, magnitudes of the angles depend on the plate thickness and decrease as the plate thickness increases. The quantity of matter in the ejecta obtained in experiments with the aluminum plate considerably exceeds that in experiments with the steel mesh targets.

The result of the work, being considered from the point of view aiming the eliminating of the pollution of the outer space with ejecta particles generated at hypervelocity impacts, clearly suggests against the usage of metallic plates as first (outer) bumper in spacecraft shield protection systems. Apparently, the better choice would be the bumpers consisting of 2-3 meshes (not only steel, as well) having the competitive ability (comparing to continuous metallic plate) to destroy effectively a projectile. Ballistic tests carried out in [5] showed that the stacked meshes can be high-quality alternative to the solid shield of the same areal density. As to the opportunity to use the mesh stack as outer bumper of spacecraft shield protection, it is worth to note that the threshold velocity of fragmentation for them is less than 2.6 km/s, that is less than the threshold velocity for the case of aluminum plate bumpers [6].

References:

- [1] Rival M., Mandeville J.C.: Modeling of ejecta produced upon hypervelocity impacts, Space Debris 1, (1999), 45–57.
- [2] Bariteau M., Mandeville J.-C.: Modelling of ejecta as a space debris source, Space debris 2, (2002), 97–107.
- [3] Christiansen E.L., Kerr J.H.: Mesh double-bumper shield: a low-weight alternative for spacecraft meteoroid and orbital debris protection. Int J Impact Engng. 14, (1993), 169-180.
- [4] Bezrukov L.N., Gadasin I.M., Kiselev A.I. et al.: About the Physical Bases of Building the Protection of the ISS Module "Zarya" against Impact Damage by Near-Earth Space Debris Fragments. Cosmonautics and Rocket Engineering 18, (2000), 140-151.
- [5] Bezrukov L., Myagkov N., Shumikhin T.: Ballistic Properties of Mesh Shield Protection at Hypervelocity Impact. Fifth European Conference on Space Debris, (ESA, Darmstadt, Germany, March 30-April 2, 2009). Book of Abstracts, 85.
- [6] Shumikhin T.A., Myagkov N.N., Bezrukov L.N.: Comparative estimation of the fragmentation onset velocity of a projectile on discrete and continuous shield. Mehanika Kompozicionnyh Materialov i Konstrukcij 17, (2011), No1, 61-70 (in Russian).

Combustion Characteristics of Droplets of Paraffin Propellants

S.G. Orlovskaya¹, V.V. Kalinchak¹, V.Ya.Chernyak², F.F. Karimova¹,
M.S. Shkoropado¹, E. Yu. Aktan²

¹ Odessa National I.I. Mechnikov's University

² Kiev National T.G. Shevchenko University

In this study we investigated combustion of single paraffin droplets (n-Octadecane C₁₈H₃₈; n-Docosane C₂₂H₄₆) in air at atmospheric pressure. The burning rates were measured. It was found that the burning rate of Octadecane droplet is 1.6 times bigger than one of Docosane. The binary droplet array burning was studied with special emphasis on ignition the second droplet by the burning first one. The critical value of the droplets spacing was defined above which the second droplet didn't ignite.

INTRODUCTION

Last decade new effective and safe propellants are intensively developed. It was found that paraffin-based fuels for hybrid rockets are environmentally friendly and very promising due to high regression rate along with safety and relatively low cost. The fire tests at Stanford University showed sufficiently high specific impulse of hybrid rocket motor [1]. The high regression rate of a paraffin charge is a result of fuel surface melting and entrainment by oxidizer high-speed flow [2]. Then the paraffin droplets burn rapidly in oxidizer flow, the heat and mass transfer is intensified in combustion chamber. So the paraffin-based propellant combustion is a complex multistage phenomenon including fuel melting, spraying, evaporation and droplets ignition. Detailed information about different n-alkanes combustion charac-

teristics is required to elaborate high effective paraffin-based propellant. So our study is aimed at measuring characteristics of n-Docosane and n-Octadecane combustion. The special experimental bench-scale setup was constructed to study ignition and burning of paraffin droplets. This scheme is presented in Fig.1. A paraffin droplet suspended on a tungsten wire (d=114 mcm) is ignited by spark Ruhmkorff coil (4). The ignition and burning process is continuously registered – the flame height by web-camera (5) and the droplet diameter by camera (8) through microscope (x24).

The successive images of the burning droplet of n-Octadecane and surrounding flame are presented in Fig.2.

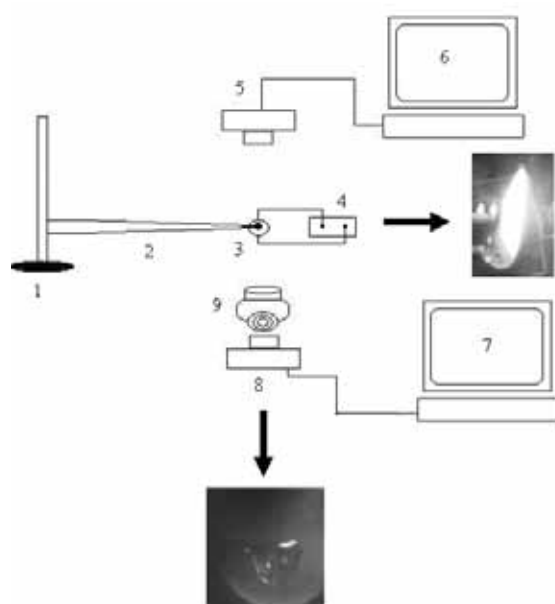


Fig.1 Scheme of experimental setup:

1 – support; 2 – tungsten wire; 3 – suspended droplet; 4 – Ruhmkorff coil;
5, 8 – digital cameras; 6, 7 – computers; 9 – microscope.

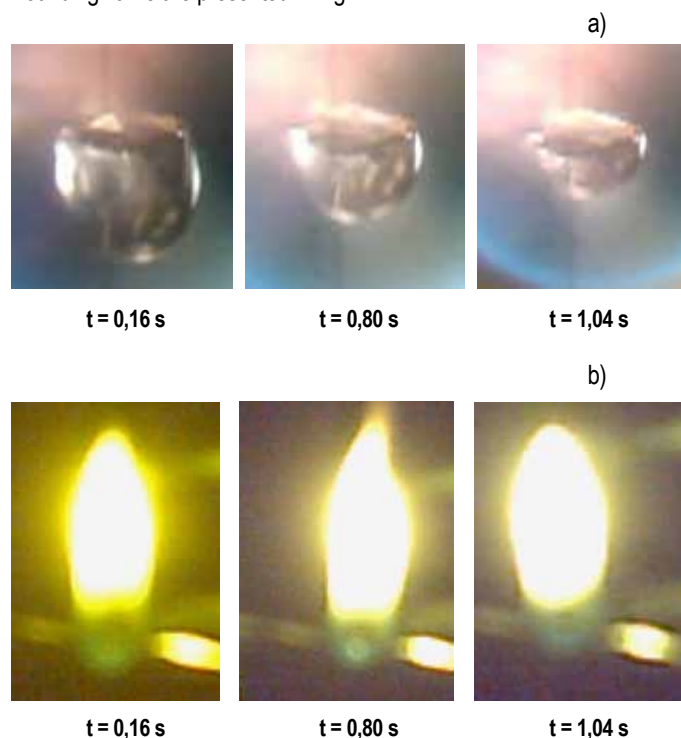


Fig.2. The successive images of burning n-Octadecane droplet and surrounding flame.

The images are processed with Image Processing Toolbox (Matlab7.0) to obtain the droplet diameter and flame height histories – $d(t)$ and $H(t)$ for n-Docosane and n-Octadecane droplets. The normalized diameter squares are calculated, the obtained data curves are presented in Fig.3. The flame height histories are presented in Fig.4.

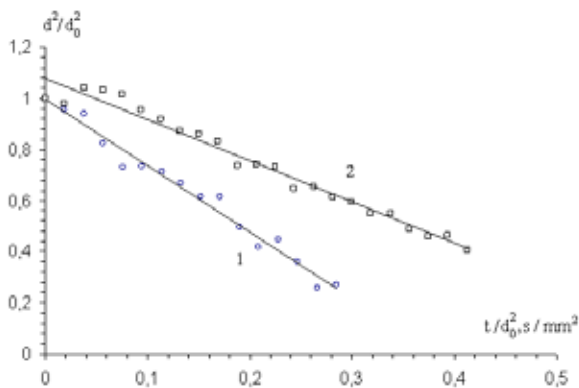


Fig. 3. Normalized droplet diameter square $d^2/d_0^2 = f(t/d_0^2)$, $d_0 = 2.05$ mm: 1 – n-Octadecane ($C_{18}H_{38}$); 2 – n-Docosane ($C_{22}H_{46}$)

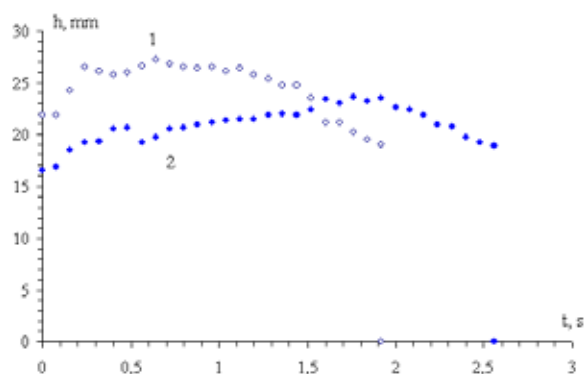


Fig. 4. The flame height histories $h = f(t)$, $d_0 = 2.05$ mm : 1 – n-Octadecane; 2 – n-Docosane.

The curves in Fig.3 are approximately linear, so we define burning rates as the curves slopes. The results are presented in Table 1. We can see that Octadecane droplet burning rate is 1.6 times greater than those of Docosane, while burning time is, correspondingly, 1.3 times smaller than those of Docosane. The main part of burning time the flame height of Octadecane droplet exceeds the Docosane one (Fig.4).

n-alkane	Molecular weight	Maximum flame height, mm	Burning rate, mm^2sec^{-1}
n-Octadecane ($C_{18}H_{38}$)	254,2	28	2,59
n-Docosane ($C_{22}H_{46}$)	310,6	24	1,61

Tab. 1.: The burning characteristics of n-Octadecane and n-Docosane droplets ($d_0 = 2.05$ mm)

From applications point of view the droplet array burning is of great interest. A binary droplet array may be regarded as a first approximation to droplets interaction in combustion chamber. We ignited the first droplet by electric spark and studied ignition of the second droplet. The ignition delay of Octadecane droplet was measured for initial droplets diameters $d = 1,82 \div 2,4$ mm. We varied the droplet-droplet spacing and their mutual position: vertical or horizontal one (Fig.5).

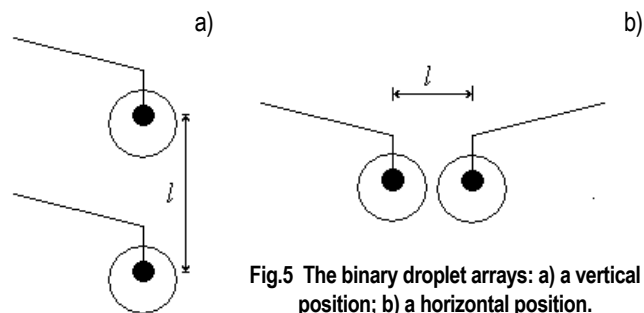


Fig.5 The binary droplet arrays: a) a vertical position; b) a horizontal position.

The experimental study showed that for horizontal droplets disposition (case b) the ignition of the second droplet took place if the distance between droplets centers didn't exceed three radii and ignition delay of the second droplet was about 0,4 s. In case of vertical droplets disposition (Fig. 5 a) the ignition delay is nonlinear increasing function of the distance between them (Fig.6).

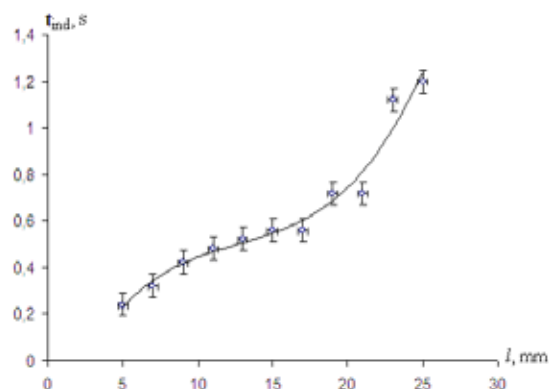


Fig. 6 The second droplet ignition delay as function of the inter-droplet spacing.

The experimentally obtained dependence $t_{ind} = f(l)$ allowed us to define the critical inter-droplet spacing l_{cr} , which limited the ignition of the second droplet by the burning one. The critical distance equals 28 – 30 mm for initial droplets diameters about 2 mm. Thus the main combustion characteristics of paraffin droplets were studied. It was found that burning rate of single Docosane droplet is 1.6 less than that of Octadecane, and the corresponding burning time exceeds by 33% that of Octadecane droplet. It was shown that in vertical binary array the upper droplet ignition takes place if the distance between droplets centers doesn't exceed 30 mm. Earlier we studied the combustion of small paraffin charges (1.7 g) in air flow. It was found that regression rate of n-Docosane exceeds by 10 % those of n-Octadecane. It could be explained by different viscosity and surface tension of these alkanes and, as a result, different average diameters of the droplets obtained [3]. So further investigation is required with account of melted paraffin spraying and size distribution of the droplets formed.

References:

[1] Karabeyoglu, M.A., Cantwell, B.J., and Altman, D. Development and testing of paraffin-based hybrid rocket fuels. // AIAA Paper A01-34608, Stanford, California, 2001.
 [2] Eric Doran, Kevin Lohner, Jonny Dyer, Zachary Dunn, Eric Wooley, and Valentin Decker. Nitrous Oxide Hybrid Rocket Motor Fuel Regression Rate Characterization//43rd Joint Propulsion Conference and Exhibit, Cincinnati, July 8-11, 2007.
 [3] E. Yu. Aktan, Yu. F. Zabashta, V.Ya. Chernyak, S. G. Orlovskaya. The Physical bases of paraffin engine design for Hybrid Rockets//Space Science and technology. V. 17. № 3. P. 28–33, 2011.

The fatigue test effectiveness improvement using NDT methods combination

Ing. V. Makarov, Ing. V. Horak, VZLÚ a.s., Prague, Czech Republic

Keywords: fatigue test, crack, NDT

The Experimental Strength Laboratory provides full-scale fatigue tests of aircraft structures and their components for the Czech aviation industry. Based on example of utilisation of VT,AE, UT and ET methods combination for failures detection during VUT 100 aircraft wing attachment fatigue test, there is the complexity of detection illustrated and also the ability of Experimental strength NDT laboratory to solve such tasks. The utilisation of combination of NDT VT,AE, UT and ET methods significantly raises the probability of failure indication in crack inception phase, makes shorter the inspection time and in consequence whereof decreases costs connected with structure fatigue test accomplishment. The application of NDT methods combination is universal and effective manner for flaw detection. It is usable in aeronautical industry and quality control.

1. INTRODUCTION

It is very essential to find out cracks in initial (early) stage of their rise during the fatigue examination process. Indispensable elements for the cracks detection in the tested structure are periodical NDT inspections determined by prescribed number of fatigue cycles. Application of conventional single NDT method is so hard and time-consuming task. Nevertheless, using AE methods markedly facilitate the monitoring process of examined structure state during the strength experiment even in time between periodical inspections. Acoustic Emission makes possible to localize occurrence crack position in the tested structure and therefore represents a short-cut road to research and detect inner and surface defects by VT,UT and ET methods.

2. EQUIPMENT LIST

There are list of instruments, which was used in NDT inspection during VUT 100 wing hinge fatigue test:

- Dakel Xedo Box-16 AE system, with sensors of type MIDI04 and TZ 09 are instruments for acoustic emission detection.
- Data were recorded by the control unit Acer Travel Mate 2003Lmi, through communication extension-line Ethernet Planet ENW-3502-2 on hard disk of this unit. Process of measurement was controlled by Daemon programme and to results presentation was used evaluating program DaeShow.
- Masterscan 340 (SONATEST), with angle beam transducer/probe MSG2550- 5 MHz (45°) is instrument for Ultrasonic detection of inner defects.
- Defectometer 2.837 (Institute Dr. Foerster), with angle probe NFe 2.835.01-2600 is instrument for Eddy Currents detection of surface cracks. Angle probe was used because of bad accessibility to side wing hinge lug.

3. RESULT

VUT 100 wing hinge fatigue test was completed on load machine MTS 250kN. Sample was submitted by oscillated cycle of loading about nominal values $F_H = 158,25$ kN and load period $f=1,7$ Hz. Fig. 1 shows measured points where acoustic response was scanned and points where strain-gauges were placed. Sample designed to be a thick-walled structure with lightening openings made of aluminium alloys D16. Connection of both parts was provided by bushing guide spigot connection made of treated steel material. NDT inspections were performed after pre-determined number of loading cycle. The check points of lug 2B4 specimen are visible in Fig.2



Fig. 1

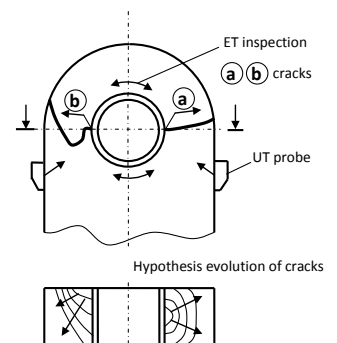


Fig. 2

During monitoring, AE sensors recorded many spurious signals. These ones were gradually identified and preliminary map of spurious signals was created. Source of these signals was from outer surroundings and energy of loading MTS machine, force relation between sample and its gripping in MTS machine and further way of setting loading of sample in MTS machine, through hard or soft force relation also. The sample

itself created another interfering signal. Dominant signal was created by linkage between part A and part B. That was emerging into result signal processing. Failure signal was emitted from five joints consisted of pin-pin-bushing and washer.

Based in these information was possible identify new emitting signal, coming from the front of crack and identify beginning state of failure. We was succeed in safety identification of advanced phase of failure which corresponded for sample loading of 170 000 cycles. Earlier and more detailed identification of initial failure state is subject of research tasks in VZLU a.s. supported by government of Czech Republic. Based on newly acquired experiences concurrently is under way the development of measuring system and also acoustic emission method self one. The propagation of failure was confirmed at lug 2B4 by the inspection by UT method also, which correspond for sample loading 175 000 cycles. During loading test, after 175 000 cycles there was detected inner crack **a** (Fig.2) in lug specimen by using Ultrasonic Testing (UT). At next load cycle rising, after 182 000 cycles there was detected 6 millimetres long surface crack **a** by using Eddy Currents Testing (ET) and Visual Testing (VT). At number of 175 000 cycles there was detected 8 millimetres long surface crack **b** on the side of lug specimen by ET and VT. The next **b** crack propagation in the inner structure was affirmed by using UT. Occurrence of disorders, their starting position, shape **a** and **b** fault propagation demonstrate Fig.2

4. FRACTOGRAPHY ANALYSIS RESULTS

Model of wing attachment specimen No. 2, central lug 4b

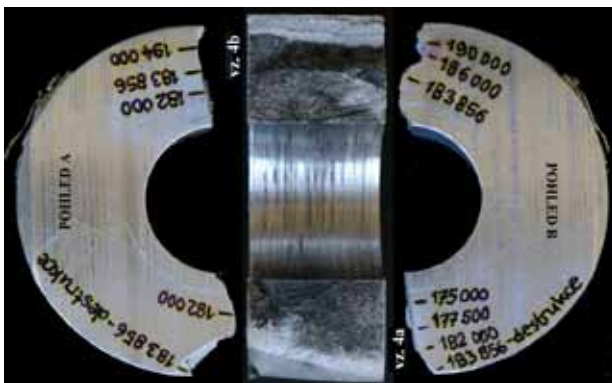


Fig. 3 General view on upper part of damaged lugs of wing attachment model (specimen No. 2)

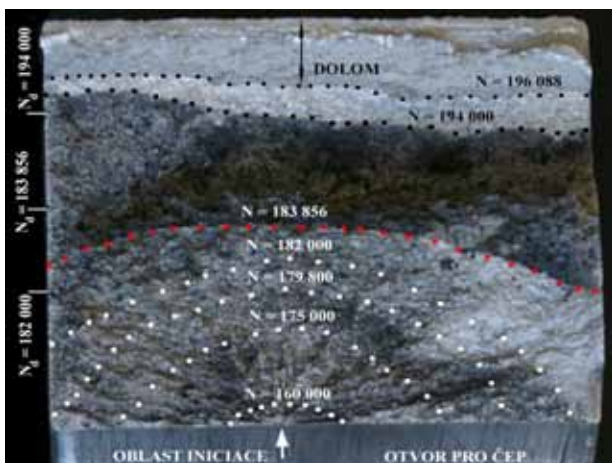


Fig. 4 Results summary of fractographic analysis of fracture surface created by 4b crack propagation.

The character of fracture surfaces is documented in macro pictures. It possible to see here even views on both sides of relevant lug.

Further in pictures is seen used marking of fractographic samples (the same is used for cracks, which have created corresponding fracture surfaces in individual specimens).

- White dotted lines delimit position and shape of instant crack tips corresponding NDT inspections at 160 000, 175 000, 179 800 and 182 000 load cycles (estimation based on fractographic reconstruction).
- Red dotted line delimit position and shape of 4b crack tip in moment of central lug rear part failure (see 4a), i.e. at 183 856 load cycles.
- Black dotted lines delimit position and shape of instant 4b crack tips both by NDT inspection at 194 000 load cycles and closely before final rupture (i.e. boundary “fatigue-rupture”). Striac mechanism has not contributed to final phase of 4b crack propagation (see also upper part of general picture in Fig. 5b).
- There are positions of marks for checking highlighted. They correspond to NDT inspections at 182 000, 183 856 and 194 000 load cycles (the position of these marks on side of lug is recorded even in the Fig. 3 – view A).
- Resulting from this evaluation the significant increasing of striac distances (and i.e. macroscopic 4b crack propagation velocity) was after application 160 000 load cycles. It was probably cause of local decreasing of 4a crack propagation velocity by crack lengths about 5 mm.

Fracture surface was created by 4b crack propagation, which was initiated on surface of the hole for attachment pin in place marked by arrow. There are any surface flaws and structural inhomogeneities which would significantly to short the time to initiation were find out in initiation area (Fig. 5a). Crack propagation progressed firstly by streak creation mechanism (Fig. 5), with increasing crack length the plastic pitted fracture mechanism participated on propagation (Fig. 5b).

Typical progress line corresponds to overloading. to which it came by total failure of lug rear part (Specimen No 4a) at 183 856 load cycles. In result of change of stress in central lug after lug rear part final fracture it came to change of crack propagation plane.

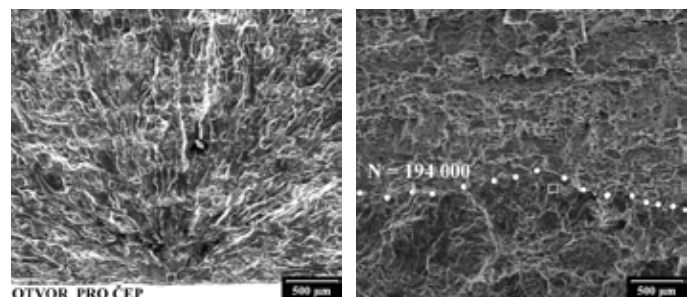


Fig. 5 Typical micro-morphology characteristics of fracture area created by 4b crack propagation.

- a) Area of 4b crack initiation on pin hole surface
- b) Fracture micro-morphology on boundary fatigue-final rupture

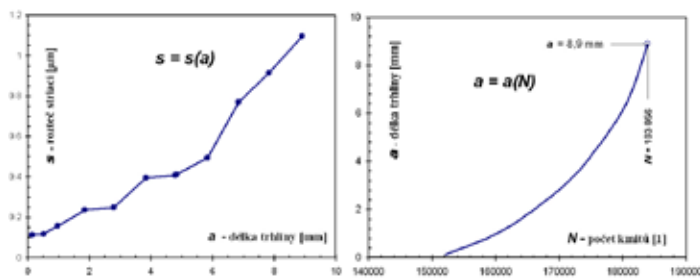


Fig. 6 Results of quantitative fractographic analysis of 4b specimen crack – in diagram of growth curve $a = a(N)$ the data pair is marked out “length crack – number of cycles used in evaluation.

CONCLUSION

Of the above combination of four NDT methods (VT,AE,UT,ET) case is evident essentially bigger reliability of detection disorders origin in the inceptive stage. Combination of this NDT methods are able to detect cracks at the same time, when strain measuring by means of strain gage, placed in proximity, give no signals about disorders initiating yet.

Single chance of detection internal fault in construction under given fatigue exam conditions is UT. Combination of three methods VT,UT and ET makes it possible to monitor cracks development during fatigue test, as on surface, as also in internal structure test part. Loading-sample experiment results obtained by the combination of four methods(VT, AE, UT and ET) were confirmed by fractographic analyses carried out by the Department of Materials, ČVUT – Prague.

References:

- [1] Drexler J., Pilař M.: Základní studie problému vyhledávání trhlin na konstrukci draku letounu v laboratoři a provozu – zpráva VZLÚ R-2281/86.
- [2] Pilař M.: Detekce trhlin na konstrukcích prováděná pomocí systému Defectometer 2.837. Written procedure – protokol VZLÚ 23/2230/99.
- [3] Makarov V.: Defektoskopická prohlídka zkušebního vzorku modelu závěsu křídla. Protokol – 276/3220/05.
- [4] Operator's manual, Masterscan 340; Issue 3, SONATEST
- [5] Mazal P.: 25th European Conference on Acoustic Emission Testing Pratur, Czech Republic, 11-13 September 2002, Brno University of Technology
- [6] Koula V., Loszi, I. AE Detection during Crack propagation on material test specimen. Zpráva DAKEL, Praha-Bratislava 1996.
- [7] Skala J.: Application acoustic emission measuring system Xedo Box16, at laboratory fatigue examination. Report R-3759/05, VZLÚ, Praha 2005
- [8] KUNZ,J. – SIEGL,J. – NEDBAL,I. – AUGUSTIN,P. – PIŠTĚK,A.: Application of Quantitative Microfractography in Damage-Tolerance and Fatigue Evaluation of Wing Spar. In: Proceedings of 24th International Congress of the Aeronautical Sciences (ICAS 2004, Yokohama). Ed. I.Grant. Optimage Ltd., Edinburgh 2004, 10 p., CD-Rom
- [9] NEDBAL,I. – KUNZ,J. – SIEGL,J.: Fatigue Crack Growth in Austenitic Steel AISI 304L in PWR Primary Water at Room and Elevated Temperature. In: Environmental Degradation of Engineering Materials [CD-ROM]. Bordeaux: University Bordeaux 1, 2003.
- [10] Makarov V., Skala J., Horak V.: New Approach to Fatigue Disorders Detection: Acoustic Emission (AE), Ultrasonic (UT) and Eddy Current Technology (ET) Methods Combination. 36th International Conference “Defektoskopie 2006”, Tabor, ISBN 80/214/3290-X

LF Technology – Smart method for composite parts production

Mgr. Eva Straňáková, Ing. Richard Pavlica, Ph.D. Prague, Czech Republic

Letoxit Foil Technology (called LF Technology) is an out-of autoclave process suitable for manufacturing of various CFRP structures and tanks developed and patented by 5M s.r.o.. One of the advantages of the process is that size of the products is not limited by the size of an autoclave. LF Technology provides freedom in choice of reinforcement (dry reinforcement, core materials) and epoxy or cyanoester matrix systems because these two components are totally separated from each other (on the contrary to prepregs where the fabric and resin form one layer). This was enabled by developing of epoxy or cyanoester resins in foil form with precise resin width layer called Letoxit Foils that allow easy manipulation and simplify the production process. After folding up the desired layers of reinforcement, Letoxit Foils and core materials, placing proper inserts or other local parts, release film is applied and bleeder fabric is added. The whole composition is then put into a vacuum bag and evacuated typically using pumps (an autoclave can be used as well). After the complete evacuation temperature is raised by the oven and originally solid layers of Letoxit Foil resin become liquid and wet through dry reinforcement layers without starting the process of curing. Only after the complete wetting it is possible to raise the temperature again up to the level of curing. Epoxy resins are suitable for usage up to 130°C, cyanoester systems even up to 250°C.

ADVANTAGES

- perfect surface quality
- production of composite parts without any air microbubbles
- cost saving because of possible combination of one resin matrix system with more kinds of
- reinforcement (fabrics, unidirectional, ...)
- only resin (Letoxit Foil) must be stored in freezer - operational cost saving (compared to
- prepregs -no fabric storage in freezer)

1. INTRODUCTION

Lightweight structures, which are inexpensive and have excellent mechanical properties, are recently one of the most desired concepts not only for aerospace industry, but generally for transportation and automotive industry. LF Technology, developed and patented by 5M s.r.o., is a very efficient technique to produce sophisticated and relatively cheap composite structures. Composite materials are the best materials for lightweight structures because they can be tailored to the specific application. The biggest advantage is a variability of polymer matrix and reinforcement, where reinforcement determines mainly mechanical properties/weight ratio. Initially, optimised mechanical properties should be found for every product. Then different reinforcement types, their orientation and number of layers in "every point" of composite part must be used to reach required properties and low weight. Also a possibility of using sandwich structures or other inserts as a local reinforcement can be a big advantage. Apart from these basic requirements for composite part production there are many others connected with the usage of these materials in the space. For

example low content of volatile compounds in the material, low coefficient of moisture expansion or high-energy radiation resistance are crucial parameters for placing of the part to any satellite or space object depending on the choice of matrix only and together with the parameters that are derived from matrix and reinforcement, for example the coefficient of linear thermal expansions, must be carefully set up. LF Technology is a smart way how these basic and space requirements for composite parts production can be achieved.

RESULTS AND DISCUSSION

LF Technology is based on laying dry reinforcement and core material to the mould with layers of foil polymer material called Letoxit Foil. Whole composition is vacuum bagged and cured at elevated temperature. The scheme can be seen in Fig. 1. Finished part is released from mould as ready to use product with excellent surface. Variability of LF Technology gives freedom to composite parts design with very competitive price. Autoclave can be employed but it is not necessary, because vacuum assistance is usually enough for reinforcement impregnation.

Basic component for LF Technology is Letoxit Foil that is usually a thermoset flexible film. Basic type is Letoxit Foil LFX 023, which is composition of special epoxy resin hardeners latent at room temperature. Film colour is originally light yellow but can be set according to the customer desire. Thickness of Letoxit Foil varies between 0,1 to 0,7 mm and it is described by area weight, which is usually between 100g/m² and 700g/m². Typical curing conditions are 120°C for 1 hour but LFX 023 can be cured at any temperature between 90°C and 140°C.

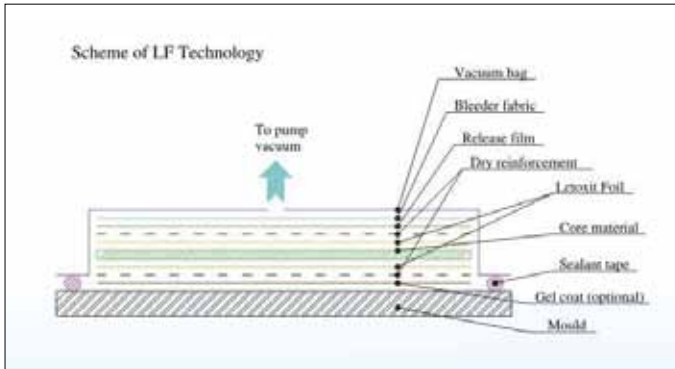


Fig.1 Scheme of LF Technology

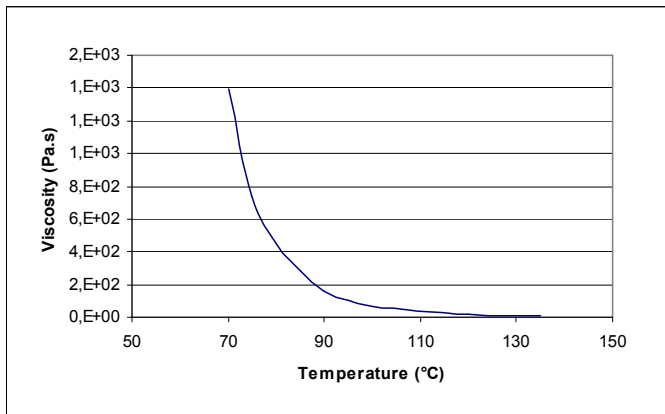


Fig.2: Dependence of viscosity on time at various temperatures

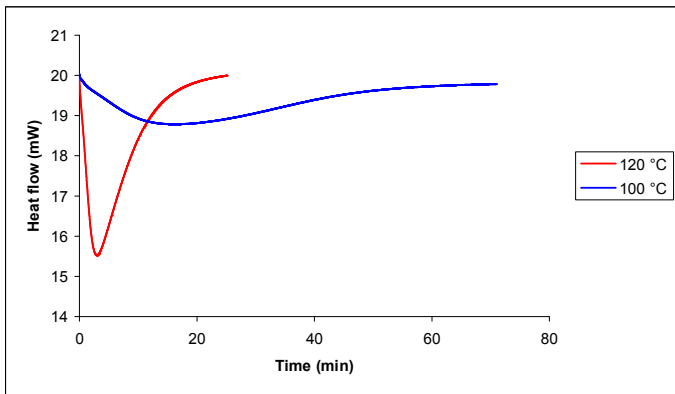


Fig. 3 Dependence of curing kinetics on curing temperature of LFX 023

Density (g/cm ³)	1,19
Curing shrinkage (%)	0,4
Hardness Barcol	18-19
Tg (°C)	95
Ultimate flexural strength (MPa)	120-125
Flexural modulus (GPa)	3-3,1
Impact strength (kJ/m ²)	45-50

Table I Mechanical properties of LFX 023 cured at 120°C for 60 min

TYPE	RESIN	CURING TEMP.	CURING TIME	Max .Tg	DESCRIPTION
LFX 023	epoxy	120°C	60 min.	100°C	basic type
LFX 035	epoxy	120°C	60 min.	125°C	low viscosity, for carbon fabrics
LFX 038	halogenated epoxy	120°C	60 min.	135°C	self extinguishing (FAR 23)
LFX 040	modified cyanoester	180°C	180 min.	250°C	high Tg, post-curing needed
LFX 044	modified epoxy	120°C	60 min.	105°C	high impact strength
LFX 054	epoxy	120°C	60 min.	155°C	higher Tg, low viscosity
LFX 055	epoxy	120°C	60 min.	155°C	higher Tg, low stickiness
LFX 056	epoxy	120°C	60 min.	125°C	self extinguishing (FAR 25)
LFX 059	epoxy	120°C	60 min.	125°C	self extinguishing
LFX 060	epoxy	80°C	240 min.	125°C	low curing temp., low viscosity, for carbon fabrics
LFX 162	epoxy	80°C	240 min.	100°C	low curing temp., higher stickiness

Tab.2. Commercial types of different Letoxit Foils

Big advantage of LF Technology is variability of the reinforcement due to very simple impregnation. Also combination of different reinforcement types is possible. The most common reinforcements are fabrics, where glass, carbon, aramid and basalt are usually used. Also hybrids of these materials are possible. The most important parameters of fabrics for LF Technology are area weight, thickness and sizing. Weight ratio of fabric and Letoxit Foil depends on geometry, which is determined by area weight and thickness of fabric. Whole free space of fabric must be filled with resin and therefore appropriate thickness of Letoxit Foil must be chosen. Calculation of minimal resin content is given by equation:

$$m_{LF} / \rho_{LF} + m_R / \rho_R = t_R$$

where m_{LF} is area weight of Letoxit Foil, ρ_{LF} is density of Letoxit Foil, m_R is area weight of reinforcement (fabric, etc.), ρ_R is density of reinforcement and t_R is thickness of reinforcement. Usually, one layer of fabric is laid to the mould covered by release agent, one layer of Letoxit Foil is applied and finally one or more layers of fabric are laid. Another reinforcement types are mats, stitched fabrics, multiaxial fabrics and direct or bulky rovings etc. Setting of resin/reinforcement ratio for other types of reinforcement is using the same rule as in case of fabric.

Dependence of flexural properties on resin content of carbon composite made by LF Technology under vacuum is shown below in fig. 4 and 5. Composite samples are made from 12 layers of balanced carbon fabric 200 g/m², type twill and LFX 023.

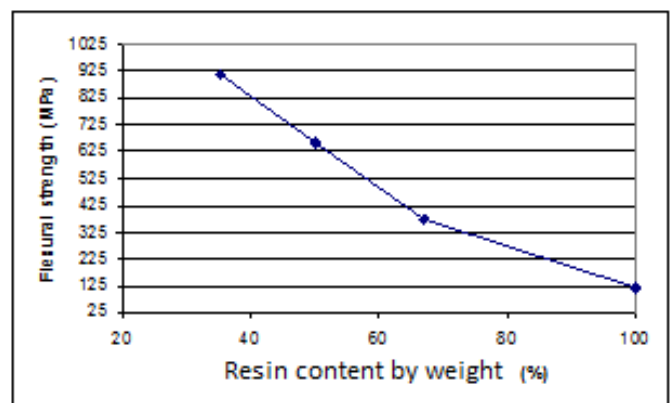


Fig. 4 Dependence of flexural strength on reinforcement content

Except of LFX 023, there are several other types of Letoxit Foils available. Some of them are listed in the table 2 below.

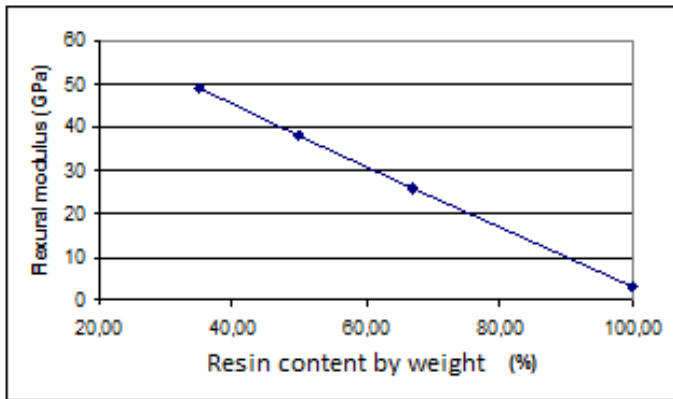


Fig. 5 Dependence of flexural modulus on reinforcement content

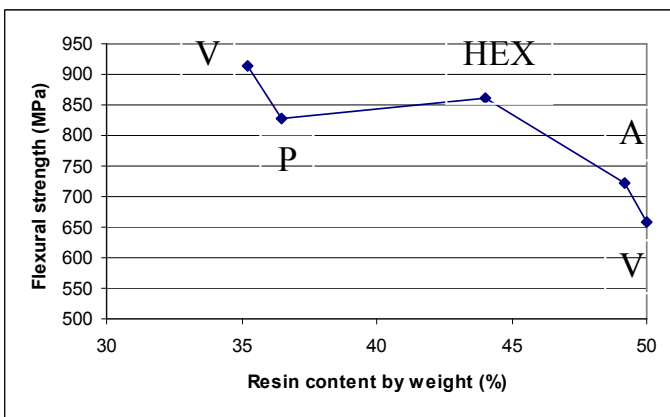


Fig. 6 Dependence of flexural strength on reinforcement content and curing equipment. Comparison with prepreg cured in autoclave.

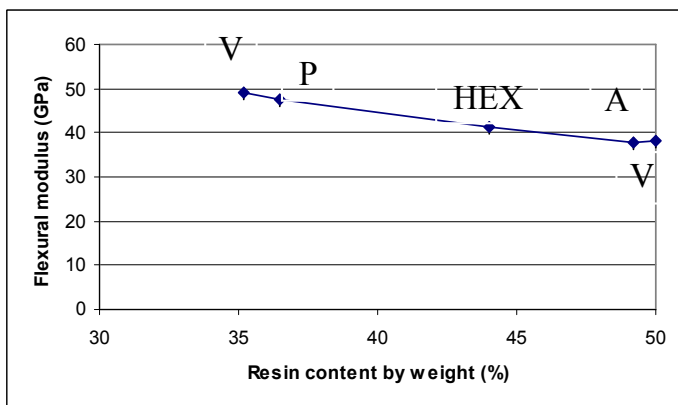


Fig. 7 Dependence of flexural modulus on reinforcement content and curing equipment. Comparison with prepreg cured in autoclave.

CONCLUSIONS

According to the exact usage of the composite part structural parameters of the part can be optimised by choosing the appropriate composition. As was mentioned before, LF Technology provides wide design's freedom in the reinforcement choice and content of the resin. Other parameters which are necessary to be fulfilled for space applications are mainly the matter of resin and are being certified according to the space standards.

EXAMPLES OF LF TECHNOLOGY APPLICATIONS

The very first application was an engine hood of ultralight aeroplane CHS 701SP, originally composite part made by hand-lay up from unsaturated polyester resin. 40% weight decrease was achieved using LF Technology. This weight decrease appears and the same stiffness remains due to use of local reinforcement with Nomex honeycombs in the top of the hood. Foam was applied in the upper part. Other important benefit was higher thermal stability. Good surface of the part was achieved although gelcoat was not applied.



Fig. 8 Engine hood of ultralight CHS 701SP – prototype



Fig. 9 Carbon knee orthosis made by ING Corporation

Next application was carbon knee orthosis made by ING Corporation, where Hexcel carbon prepreg was substituted. Advantages were better bonding of steel juncture and decrease of material costs with almost the same labour costs. Mechanical properties of the orthosis composite body made by LF Technology were comparable with mechanical properties of the prepreg orthosis.



Fig. 10 VUT 100 made by EVEKTOR. (Czech Republic). LF Technology is used for glass foam sandwich baggage wall, 2005

Another application was a baggage wall in 4 seats airplane VUT 100, where good stiffness of baggage wall and low weight were achieved by usage of a sandwich manufactured from ROHACEL foam, glass fabrics and LFX 023. The most recent examples of LF Technology usage in the aerospace area are interior panels for airplanes L-410 and M101-Expedition or transport box for people infected by highly infectious diseases (fig. 11 - 16).



Fig.11 M101 Expedition



Fig.12 Interior panels of M101 Expedition made by LF Technology with LFX 038 according to FAR 23



Fig. 13 Box for transport of people infected by highly infectious diseases



Fig. 14 Box is transported by helicopter panels where installed



Fig. 15 Airplane L410 where ceiling interior



Fig. 16 LF Technology was used for the production of the ceiling interior panels in airplane L-410 (according FAR 23)

Friction Stir Welding of Aerospace Structures

Ing. Petr Bělský / VZLÚ, a.s., Prague, Czech Republic

As an innovative joining technology for lightweight metal alloys, Friction Stir Welding (FSW) attracts more and more interests from aeronautical and space industry. Due to its numerous process benefits, such as high product efficiency, perfect mechanical property, lower structure distortion and automatic machinery process, FSW is often depicted as a revolutionary welding method in the new century.

The article gives general information about the revolutionary welding technology and summarises its present aeronautical and space applications in the world. Finally, short information about last R&D activities realized in the area by VZLU is presented.

1. INTRODUCTION

Friction stir welding (FSW) is an enabling solid-state joining process for fabrication of low-cost lightweight structures. This revolutionary Hi-Tech technology was invented and patented in 1991 by The Welding Institute (TWI) in Cambridge. In the last decade, FSW was successfully implemented in many structural applications in aeronautical and space industry. Traditional joining technology used in aeronautical industry – riveting fails to satisfy recent enhanced demands for production progressive low-cost airframe structures. Riveting is simple and very well mastered joining method but it is very time-consuming technology. Potential advantages of FSW joints include economic benefits, reduction in part count and weight, elimination of hole drilling with the associated stress risers, and removal of outer moldline fasteners thereby improving corrosion resistance. For space applications the method offers enhancement of joint reliability and possibility to weld new materials, which are unweldable with fusion-welding technique and which enable to achieve significant weight savings.

BASIC PRINCIPLE OF FSW

The basic form of the process uses a cylindrical, non-consumable tool, consisting of a flat circular shoulder, with a smaller, profiled probe protruding from its centre (see Fig. 1). Plunging a rotating probe into the adjoining plates joins material of work-piece and subsequent heating caused by friction between the rotating tool and material elevates the temperature of the local weld region high enough to plasticize material of work-piece. Through mechanical forces the heated material is extruded from the front of the probe to the back as the probe transverses the length of the joint. The combination of the frictional heat and mechanical working produces a solid-phase joint. Because no macroscopic melting takes place the weld is left in a fine grain wrought structure and other problems associated with liquid to solid transformation, porosity, solidification cracking, residual stresses are all eliminated. The friction process is environmentally friendly, as it does not require consumables (filler wire, flux or gas) and produces no fumes. FSW makes possible joining speeds 6 times faster than automated riveting or 60 times faster than manual riveting, with improved quality. The joining method can be used for joining many types of materials and material combinations, if

tool materials and designs can be found which operate at the forging temperature of the workpieces.

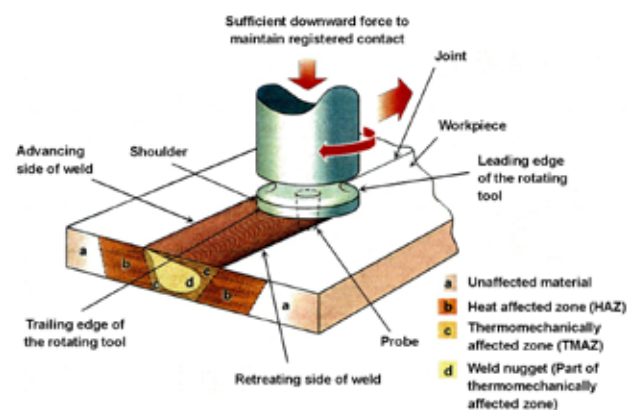


Fig. 1 Principle of Friction Stir Welding

APPLICATIONS IN AERONAUTICAL INDUSTRY

The first commercially produced FSW welded aircraft parts were probably welded toe nails for ramp of Boeing C-17 Globemaster III cargo aircraft and cargo barrier beams for Boeing 747 Large Cargo Freighter but the most important milestone for dissemination of FSW to the aeronautical industry was small business jet aircraft Eclipse 500 developed by Eclipse Aviation Corp. (see Fig. 2). The Eclipse 500 is a twin engine jet, with six passenger capacity, 368 kt (680 km/h) cruising speed, a 41 000 ft (12 500 m) service ceiling and a range of 1125 nm (2084 km).

Stir welding was used on the Eclipse 500 to build up integrally stiffened skin panels by lap welding ribs, stringers and frames to pocketed skins. The pockets were machined or chemically milled into the skins between the stiffeners for weight savings. The lap welds were used over 65% percent of the aluminium-alloy structure in the cabin, aft fuselage, wings and engine mounts. That way FSW replaced more than 60% of the rivet joints (about 30 000 rivets per airplane) normally used in the assembly process. Overall, there were used a total of 263 welds on each aircraft with a total length of 136 meters. The first flight of the

prototype accomplished in August 2002 and full type certification was achieved on 30th September 2006. Eclipse Aviation delivered 259 of the friction stir welded business jets.



Fig. 2 Eclipse 500 and 5-DOF FSW machine MTS ISTIR Aero

Next aeronautical manufacture showing great activity in the area of utilization of FSW for aircraft structures is Empresa Brasileira de Aeronáutica S.A. (Embraer). Embraer started cooperation with GKSS Forschungszentrum in spring 2002. In frame of the common project were developed and produced friction-stir welded fuselage parts that yielded a weight saving of around 30 per cent. For the welding activities was used robotic FSW system TR 805. Outputs of the project will be used in Legacy 450/500 program.

Lockheed Martin (LM) achieved very interesting results in frame of MAI program. The Metals Affordability Initiative (MAI) was created in 1999 by the Air Force Research Laboratory's. Its goal was to spur technology development that is aimed at lower cost material and manufacturing methods, efficient component designs, and tools and methods for reducing the time required for development and production manufacturing of metallic components. R&D activities of LM were focused mainly on riveted structure replacement with FSW. Stir welded cargo floor demonstrator and center wing bulkhead of C-130 transport aircraft were realized. Successful implementation of FSW resulted in significant reductions in part count, touch labor, and overall manufacturing cost. LM declared 20% cost reduction.

Also both the biggest aircraft manufacturers Boeing and Airbus decided to use FSW technology in the structures of their large civil and military aircrafts. Floor panels for Airbus A400M are now friction welded by Pfalz Flugzeugwerke and Airbus uses FSW method for the longitudinal fuselage skin joints of A340-500/600 and A-380. Airbus also plans to use FSW extensively on the A350. The technique has enabled the A350 design team to reduce the number of longitudinal fuselage panels from eight to four, resulting in significant weight-savings while also improving the reparability and maintainability of this component. The manufacturer indicated that FSW will save in the order of 0.9 kg for each meter of longitudinal fuselage panel joint.

Boeing uses FSW method for welding of cargo floor treadways and webs for C-17 and plans to use it also for selected aluminium and titanium parts of B787 Dreamliner. Boeing in frame of cooperation with Pacific Northwest National Laboratories and University of South Carolina developed technique allowing fabrication of very large monolithic structures such as jet engine leading edge with superplastic forming (SPF) of friction welded aluminium and titanium tailored blanks. The test results have shown that FSW is a viable option for fabrication of the tailored blanks for use in the manufacture of SPF commercial hardware.

SPACE APPLICATIONS

The United States

At the beginning of the 90's, NASA decided to use new Aluminium-Lithium alloy Al-Li 2195 in new redesigned structures of its space launch systems. The new alloy is only 5% lighter than previously used Al alloy 2219 but its 30% greater strength at cryogenic temperatures results in a significant weight savings. Initially VPPA (Variable Polarity Plasma Arc) method was used for welding of the new alloy but it was very problematic. The repair welds were difficult to make and the joint strength had much lower mechanical properties. This drove up production cost and that is why alternative welding technology was sought. The first tests of new FSW method appeared very successful because the FSW welds were stronger than the fusion arc welded joints and the process was very effective.

Boeing has applied FSW to the Interstage Modules of a Delta II rocket, and the first of these was launched successfully in August 1999 (see Fig.3). Next important step was demonstration of the strength and quality of longitudinal FSW joints on three cylindrical tank components in Delta II rocket during the Mars Odyssey launch in April 2001. After that FSW was implemented for full friction welding of all fuel tanks of Delta II and Delta IV rockets. Boeing reported that FSW technology for the Delta IV common booster core tanks increases the weld strength by 30 to 50% and lowers cycle time by nearly 80%. The FSW specific design of Delta II and Delta IV achieved 60% cost saving, and reduced the manufacturing time from 23 to 6 days.



Fig. 3 – Space launch system Delta II

In frame of SLWT (Super Light Weight Tank) program, which was started in 1993, Lockheed Martin (LM) redesigned structure of Space Shuttle's External Tank (ET) and implemented FSW technology. The first FSW welds were used for ET-132, the 128th flight tank that LM has assembled for NASA. Lockheed Martin became also the prime contractor to NASA for the Orion MPCV. The structure of the vehicle consists of panels jointed together with 33 FSW welds. The longest is final close out weld joining the Forward Cone Assembly and Crew Tunnel to barrel shaped Aft Assembly. The final FSW weld is about 11 m in length.

In 2002, Elon Musk founded Space Exploration Technologies Corp. (SpaceX) located in Hawthorne, California. This private company developed Falcon 1 (F1), Falcon 9 (F9) launch vehicles and Dragon spacecraft. Fuel tanks for F1 and F9 with outside diameter 3.6 m and pressure vessel for Dragon spacecraft are completely friction welded.

Japan

Japan Aerospace Exploration Agency (JAXA) in cooperation with Mitsubishi Heavy Industries, Ltd.(MHI) started development of new launch vehicle H-IIB in 2003. In order to enhance the reliability of the new rocket, Friction Stir Welding and Spin formed dome manufacturing technology were implemented in production of propellant fuel tanks. The H-IIB is a two-stage launch vehicle that uses liquid oxygen and liquid hydrogen as propellant. The first stage tank is 5.2 m in diameter and the approximate total lengths of the component tanks are, respectively, 7 m LOX tank and 20 m LH2 tank, meaning that the entire tank structure holds about 176 t of fuel in total. The second stage tank has diameter 4 m and it holds about 16.7 tons of fuel in total. All the tanks were assembled using FSW technology. MHI uses FSW probably also for assembly of Pressurized Logistics Carrier (PLC) and other modules of the HTV.

China

China National Space Administration (CNSA) announced utilization of FSW for welded fuel tanks of Long March 5 and structure of the first Chinese space station Tingong 1. Long March 5 (CZ-5, Changzheng 5) is next generation heavy lift launch system with maximum payload capacity 25 t to LEO and 14 t to GT. The first launch is planned in 2014. Tiangong 1 is 8-ton orbital laboratory module, which is intended mainly as an experimental testbed to develop the rendezvous and docking capabilities of Chinese space vehicles. It was launched on 29th September 2011.

Europe

The first attempt to implement FSW in space applications on the European continent was done by Fokker Space B.V. It realized study relating to applying FSW to the ARIANE 5 main motor thrust frame. The thrust frame is essentially an unpressurized machined aluminium 7075 alloy parts interconnected by the extensive use of manually installed Hi-Lok fasteners. FSW could dramatically decrease labour input and overall manufacturing cost of the part. In frame of the study research activities focused on FSW lap joints were performed and new cone sub-assembly multifunctional jig was developed.

Next European FSW pioneer in the area is Thales Alenia Space (TAS). It pioneered FSW for some spacecraft components, and has applied the process, under contract to the Italian Space Agency, to a full-scale prototype of a cryogenic tank using an Al-Li alloy. TAS indicated FSW as very promising technique for future European space applications.

MT Aerospace AG demonstrated three-dimensional dome segment of the Ariane 5 liquid hydrogen tank whose port flange was assembled using the FSW method at this year's International Paris Air Show in Le Bourget. In cooperation with NASA and Lockheed Martin Space, a tank dome with a diameter of 5.4 meters was manufactured for large cryogenic tanks. For the production, flat panels were joined to one plate by FSW and then pressed into the final form using the spin-forming method. A cooperation agreement for the development of the new Upper Stage tank for Ariane 5 Midlife Evolution was signed with Astrium in May 2011. MT Aerospace is responsible for development and production of the enlarged, lightweight propellant tank, making the new cryogenic upper stage more efficient. From 2017 on, the Ariane 5 ME will have up to 20% more payload capacity.

FSW AND FSSW ACTIVITIES IN VZLU

The first contact of VZLU with the revolution FSW method took place already in July 2002 during The First EuroStir Workshop held at TWI but own R&D activities were started in 2005. VZLU established near cooperation with The Welding Institute and became one of the participants of framework project LOSTIR. The project was favourable evaluated and has been approved for funding by the European Commission in July 2003 and officially started in November 2004. The main objectives of the project were the development of a low cost torque/force-monitoring device for conversion milling machines to FSW technology and development accurate and reliable predictive model for the FSW process.

Systematic FSW research activities were started in 2005 in frame of the project ARC-B2 (Aerospace Research Centre) supported by the Czech Ministry of Education, Youth and Sports. The technology collaboration and licence agreement between TWI and VZLU was signed in June 2006 and the first official FSW tests performed in September 2006. These first experiments were focused mainly on the tests of basic principle and demonstration of general possibilities of FSW. The tests were carried out on manual knee-type milling machine FGU40 with 11 kW spindle drive motor power equipped with monitoring system, digital measuring system and small various-purpose fixture with maximum length of welds up to c. 200 mm.

This old machine was used also for the next experiments but the main FSW machine of VZLU became new NC bed-type milling machine FSG 80 A2 purchased from TOS Kuřim in 2006. This machine has large table clamping surface 2000x800 mm and high main spindle motor output – 20 kW. Adaptation of the machine for FSW technology required some small design modifications. Most considerable changes were connected with increasing maximal feed trust in axes "Z" from 15 to 20 kN. The machine was also equipped with new special clamping fixture combining vacuum system Horst-Witte and standard mechanical elements enabling realization of long welds (up to 1200 mm).

A lot of various studies focused on butt, lap and T-welds were performed through the years 2006-2011. **In frame the R&D FSW activities were welded these materials:**

1. Al-alloys (2024-T3, 7075-T7351, 6082-T6, 6060-T6, 5083-H34,5754-H11), thicknesses 1-8 mm
2. Mg-alloys (ZE10, ZE41, AZ31, AZ61), thicknesses 0.8-3 mm
3. Copper, thickness 1.2 mm
4. Steels (USIBOR 1500, AISI 304), thickness 1.5 mm

Most welding tools used for above mentioned experiments were designed and manufactured directly in VZLU. First FSW trials in 2006 were performed with simple tools having concave shoulder and cylindrical rounded pin but for the next experiments were tested markedly more complicated tool geometries. Last big challenge and very important milestone in the area was realization of tools for friction welding of high melting temperature materials such as steel (see Fig.4). For the FSW experiments were designed and tested special tools with working parts made of pure tungsten, W24.5%Re2%HfC alloy, Silicon Nitride and PCBN.



Fig. 4 – FSW of stainless steel profile in VZLU

Studies focused on FSSW – Friction Stir Spot Welding were next very interesting R&D activities of VZLU related to FSW. FSSW owes its origins to linear FSW and has the same or similar advantages. The technology has a big potential to replace some conventional joining methods such as resistance spot welding. It is also utilizable for thin-wall lightweight structures. That is why VZLU started research activities in the area and became one of the participants of the EU project SPOTSTIR in 2007. The main objective of the project was development and production of prototype hand held Friction Spot Welding gun for the cost effective repair of high aluminium content vehicles by SME body shops.

Preliminary tests of FSSW technique in VZLU focused mainly on spot welding of A5754 aluminium automotive sheet were realized in 2009. The influence of welding parameters and tool geometry on bond formation and tensile strength of the resulting joints was studied. In frame of the R&D works new unique SD-Tool geometry with secondary cone shoulder located inside probe was developed.

CONCLUSIONS

FSW has made spectacular advances in the last decade, enabling realization of non-linear and three-dimensional welding of the main components of aircrafts and space vehicles. It is possible to use the technology for production primary airframe structures and to eliminate thousands of rivets, resulting in reduced assembly costs, better quality joining, and stronger and lighter joints. Because FSW is significantly faster than riveting, production cycle times can be drastically reduced. The method is also suitable for utilization in space applications. The

principle of FSW enables to joint some alloys, which are unweldable with fusion-welding technique and which enable to achieve significant weight savings. At the present time it clear that it will completely replace VPPA technology in welding of fuel tanks for all new space launch vehicles. Arc welding processes will continue to decrease in relevance for the aerospace industry.

ACKNOWLEDGEMENTS

The R&D FSW activities realized in VZLU in years 2005-2011 were supported by the Czech Ministry of Education, Youth and Sports. The author would like to thank all cooperating partners from Czech Republic and abroad.

References:

- [1] Kallee S. W., Nicholas E. D. and Thomas W. M.: 'Friction stir welding – invention, innovations and applications'; Tube International, Vol. 21, No. 117, July-August 2001.
- [2] Bělský P.: Friction Stir Welding of Aircraft Structures; Letecký zpravodaj No.3, page 15-17, VZLU, Prague, 2003.
- [3] Ding, Jeff; Bob Carter, Kirby Lawless, Dr. Arthur Nunes, Carolyn Russell, Michael Suites, Dr. Judy Schneider (2008-02-14): "A Decade of Friction Stir Welding R&D At NASA's Marshall Space Flight Center And a Glance into the Future". NASA http://ntrs.nasa.gov/archive/nasa/casi.ntrs.nasa.gov/20080009619_2008009118.pdf. Retrieved 2009-04-14.
- [4] Nimura K., Kondo S., Nakamura T., Goto T., Egawa K., Arita M.: Development Status of H-IIB Launch Vehicle, Technical Review Vol.45, No.4, Mitsubishi Heavy Industries, Ltd., December 2008.
- [5] Brooker M.J., Deudekom A.J.M., Kallee S.W., Sketchley P.D.: Applying friction stir welding to the Ariane 5 main motor thrust frame; Proceedings of the European Conference on Spacecraft Structures, Materials and Mechanical Testing, Noordwijk, The Netherlands, 29 November – 1 December 2000 (ESA SP-468, March 2001).